Micro Machining Using the Electrochemical Discharge Assisted Cutting

by

Baoyang Jiang

A dissertation submitted in partial fulfillment
of the requirements for the degree of
Doctor of Philosophy
(Mechanical Engineering)
in the University of Michigan
2017

‘

Doctoral Committee:

Professor Jun Ni, Chair
Professor Elijah Kannatey-Asibu Jr.
Professor Richard M. Laine
Professor Jyotirmoy Mazumder

Baoyang Jiang

byjiang@umich.edu

ORCID iD: 0000-0002-5431-0202

ACKNOWLEDGEMENTS

I am honored and humbled to have the opportunity to thank those who have made this dissertation possible.

I would like to express my most sincere gratitude to my advisor, Professor Jun Ni, for his persistent help and guidance throughout my graduate study. The dissertation could never be completed without him. I was constantly inspired by his enthusiasm towards research in manufacturing science.

I would like to thank Dr. Shuhuai Lan for his valuable suggestions for my research. I am also grateful to Mr. Xianli Qiao for his advice and assistance on the difficulties I encountered during experiments.

I appreciate my committee members Professor Elijah Kannatey-Asibu, Professor Richard Laine, and Professor Jyoti Mazumder for their time and efforts in reviewing this dissertation. Their insightful advice has significantly improved the work presented in this dissertation.

I wish to thank all my friends from the S. M. Wu Manufacturing Research Center. It was a true pleasure working with my fellow labmates for stimulating discussions. I would also like to thank all my friends at the University of Michigan. Their friendship makes my life in Ann Arbor meaningful and blissful.

Finally, and most importantly, I would like to thank my parents. Their endless love and support gave me confidence to face challenges over the years.

TABLE OF CONTENTS

LIST OF FIGURES

LIST OF TABLES

ABSTRACT

The desirable physical and mechanical properties and the low machinability of glass have attracted many studies toward micro-machining of non-conductive materials. Recently electrochemical discharge machining is considered to have good potential in processing non-conductive materials. Material removal in the process utilizes the electrochemical discharge effect, in which high thermal energy is released through electric discharging. However, electrochemical discharge machining has not been adopted in the industry so far. The major challenges include slow material removal, low surface quality, and lacking in geometric accuracy.

In this study, a hybrid machining process combining electrochemical discharge and mechanical cutting is presented, under the name “electrochemical discharge assisted cutting (EDAC)”. Mechanical cutting can be very effective as the material is softened by the high heat generation in electrochemical discharging. The material removal rate is boosted significantly with the hybrid process.

The experimental investigation of the EDAC includes both drilling and milling processes. A machining system is designed and fabricated to enable the EDAC. Experiments are conducted to validate the feasibility of the concept, as well as to explore the boundary of the machining performance in terms of material removal rate, geometric accuracy, and surface finish. By using micro drill bit or flat end mill as the tool electrode, electrochemical discharge can be incorporated into mechanical cutting and significantly increases the material removal rate.

Surface finish of the EDAC milling is around Ra 4 μm. Overcutting can reach hundreds of microns, but compensation is possible by appropriate tool path control since overcutting can be quantified.

Models are created to simulate the electrochemical discharging and the material removal processes. A physics-based model is derived for gas film dynamics and electrolysis to correlate film characteristics with various process parameters. Meanwhile, the mechanisms of the discharging phenomena are revealed through modeling and experimentation, including the process of bubble growth and the criterion of the transition from bubbles to gas film.

The energy and spatial distributions of sparks are determined both empirically and mathematically. The energy level of each spark generated is measured and is fit in a stochastic model with a two-component mixture log-normal distribution. The energy distribution proves that conic tool improves the consistency of spark generation and suppressed the generation of minor discharges.

The proposed process model is capable of predicting temperature profile and the corresponding material properties, as well as the cutting forces in the machining process. The electrochemical discharging, as the heat source in the process, is modeled analytically and is followed up with finite element simulations to determine the heat distribution on the tool electrode. The temperature profile can therefore divide the material into three zones: thermally removed, softened, or solid. A cutting force model is created to estimate the overall cutting force that addresses the thermal removal and the thermal dependent mechanical behavior. It is found that amorphous materials can be softened significantly at much lower temperature than the melting point. Mechanical cutting can therefore be effective in removing the softened material and preserving surface quality.

Chapter 1

Electrochemical Discharge Assisted Cutting

1.1 Introduction

Glass is a hard and brittle material with many excellent physical and mechanical properties, including high hardness, optical transparency, low electrical conductivity, and good corrosion resistance. Glass is widely used in automotive, electronics, optics, and biomedical industry due to its unique materials properties. For example, glass is often chosen to be the material for lab-on-a-chip (LOC) devices (Figure 1.1). LOC is a device with embedded microfluidic systems of utility for biomedical and laboratory functions. The applications of microfluidic technologies have dramatically increased over the past decades. LOC should be considered as a toolbox for developing innovative products in the life science (Haeberle and Zengerle, 2007).

Glass components of LOCs are typically produced using chemical etching and photolithographic technologies (Schneegaß et al., 2001), which are time consuming and energy inefficient. Such situations can be significantly improved if glass devices can be fabricated directly through mechanical cutting. However, glass is not amenable to mechanical machining

due to its low fracture toughness. Conventional cutting results in fractured surfaces and subsurface damage.

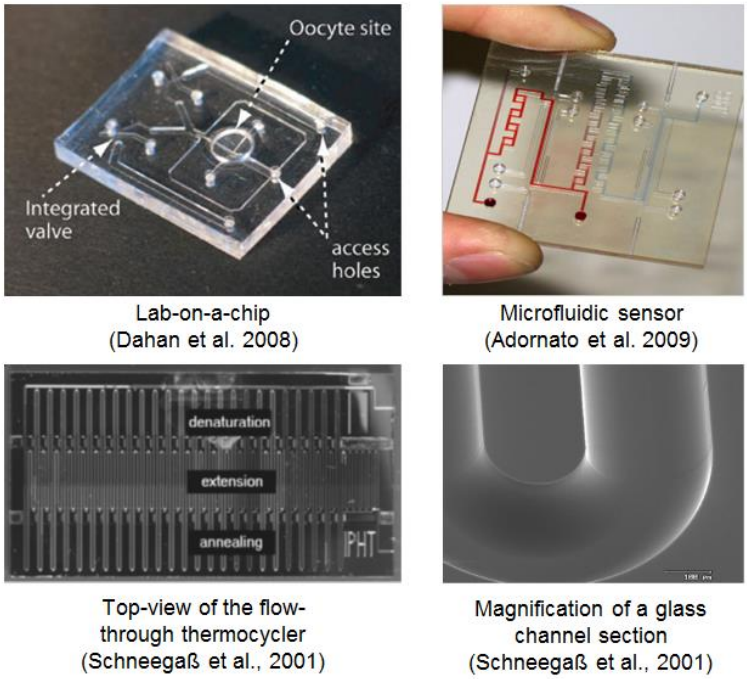

Figure 1.1. Examples of lab-on-a-chip products.

Glass's desirable physical and mechanical properties and poor machinability have attracted many studies towards glass machining. Etching, lithography, and grinding are considered to be viable approaches, but all these technologies have low machining efficiency, as well as limitations in creating 3-dimentional geometry. Advances in ductile machining of glass have proven that mechanical cutting has the potential to become an efficient cutting process for glass. Machining in the ductile regime can produce continuous chips, resulting in good surface quality and minimal cracks. Researchers have facilitated ductile machining of glass for turning and surface texturing (Foy et al. 2009). However, the physics behind the transition from brittle to ductile regime remains unclear, and therefore viable ductile cutting processes are not yet available.

Electrochemical discharge machining (ECDM), also known as spark-assisted chemical engraving (SACE) or electrochemical spark machining (ECSM), is a non-conventional machining technology that has shown potential in machining non-conducting brittle material (Wüthrich et al., 2005, Wei et al., 2011). Similar to electric discharge machining (EDM), material removal in the ECDM processes is through the thermal and mechanical energy of the discharging process. Unlike EDM, in which discharge activity takes place directly between the tool electrode and the conductive workpiece, ECDM takes advantage of electrochemical discharge phenomenon and therefore does not require the workpiece to be electrically conductive. Figure 1.2 illustrates the electrochemical discharge phenomenon. Two electrodes are immersed into electrolyte, typically sodium hydroxide, to perform electrolysis. Similar to a typical electrolysis process, gas bubbles are generated on both electrodes given constant electric potential is applied on the electrodes. Since the tool electrode is very small (0.5 mm diameter in this case), bubbles merge into gas film if the reaction rate is high enough. The gas film provides insulation between electrode and electrolyte, creating intense discharge as the gas film breaks down under high voltage.

In the ECDM process, the workpiece is placed close to the discharging end of tool electrode. Sparks with high temperature would therefore enable material removal.

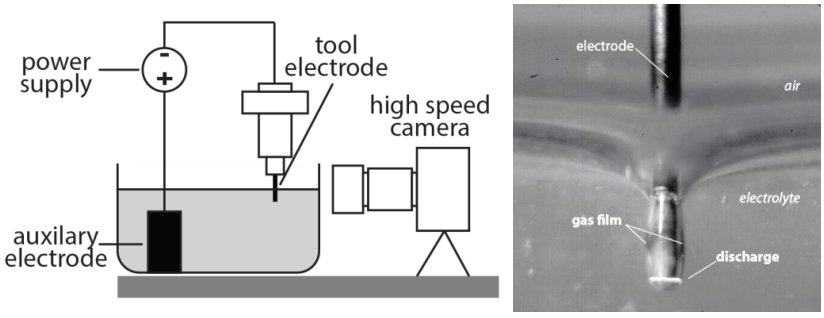

Figure 1.2. Electrochemical discharge phenomenon: setup and picture

The research in this dissertation is intended to develop a micro-milling technology on non-conductive materials under the name "electrochemical discharge assisted cutting (EDAC)". It is a hybrid machining process combining electrochemical discharge machining (ECDM) and mechanical micro-cutting. The research is dedicated to developing comprehensive and fundamental studies of the proposed micro-end-milling process, including the investigation of discharging activity and cutting force, tool design and process modeling and optimization, and complex geometry fabrication.

1.2 Literature review

In the past decade, research on ECDM has increased dramatically. Most of the studies focused on drilling because drilling is the most fundamental and straightforward process for a brand new machining technology. These studies include designing a special tool electrode (Yang et al. 2011, Han et al. 2011, He et al.2012, Mochimaru et al. 2012, Wei et al., 2010), high aspect ratio drilling (Jui et al. 2013), and tool kinematics (Gautam and Jain 1998, Jain et al. 2002). The limitations of ECDM include low machinable depth, slow drilling speed, and large overcut. In addition, a few attempts at end-milling using ECDM were made (Zheng et al. 2007, Abou Ziki et al. 2012), but it turned out to be very slow and uncontrollable. The typical feed rate was in the range of 10 μm/s, with a layer thickness of 50 μm and a mill diameter of 200 μm.

Improving the machining efficiency and quality has long been the concentration for studies of ECDM of non-conducting materials. Fascio et al. (2004) conducted a study to characterize the electrochemical discharge phenomenon using both qualitative and quantitative measures. The results indicated that the discharge process involves five regions (Figure 1.3): (1)

the thermodynamic and overpotential region at the initial stage; (2) the ohmic region as low voltage applies; (3) the limiting current region as rapid gas generation prohibits the conductivity; (4) the instability region as gas starts to form an insulating layer; and (5) the arc region as the gas film becomes stable and sparks are observed.

Research on choosing process parameters was conducted to improve material removal rate, geometric accuracy and surface integrity. These researches contributed to modeling the ECDM process from many aspects, including the modeling of the heat source, spark generation, and machining depth. Jain et al. studied the impacts of tool kinematics on material removal rate and maximum machining depth comparing with the conventional tooling and feeding mechanism (Gautam and Jain, 1998; Jain and Chak, 2000). An abrasive cathode also aided material removal in the ECDM process (Jain and Choudhury, 2002). Wüthrich et al. conducted research on process modeling including gas film and current signals (Wüthrich et al., 2006; Wüthrich and Hof, 2006).

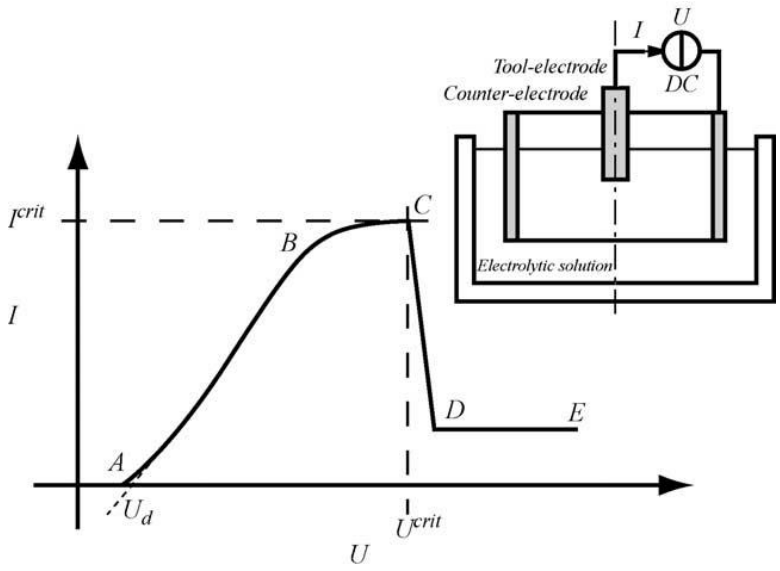

Figure 1.3. Voltage-current characteristics in electrolysis.

(Wüthrich and Fascio, 2005)

To achieve a better machining process, innovative methods were introduced into conventional ECDM, including developing new procedures and machining tools. Wüthrich and Hof (2006) applied tool vibration and experimentally demonstrated the improvement in the material removal rate. Yang et al. (2011) fabricated a spherical tool electrode and showed the merits of the new tool with respect to machining efficiency and accuracy. Mochimaru et al. (2012) introduced a two-step machining method to reduce the over-cutting in drilling process.

1.3 Research objectives

There is a need to develop hybrid micro-manufacturing processes capable of generating three-dimensional micro-scale features in hard-to-machine non-conductive materials such as glass. Limitations in current manufacturing processes for these materials include: (1) low process capability of generating complex three-dimensional micro-scale features; (2) limited machinable depth, surface quality and efficiency; (3) lack of comprehensive machining models; and (4) insufficient understanding of machining characteristics.

The goal of this research is to reveal the fundamental mechanisms involved in the electrochemical discharge assisted micro milling process. A systematic study is conducted to address the above limitations. The study targets at understanding the fundamental mechanisms of electrochemical discharge assisted micro-milling for non-conductive hard-to-machine brittle materials. The specific research objectives are:

- Develop a machining system that facilitates electrochemical discharge cutting, including drilling and milling processes. Experimental studies were carried out to validate the

feasibility of the hybrid machining process. Process parameters were investigated to establish the correlation between machining performance and input parameters.

- Develop a physics-based model for the gas film evolution and discharging process. The output of this model should establish connections from various process parameters to the magnitude and distribution of electric energy released through sparks. The model also provides comprehensive understandings of the fundamentals of both electrical and electrochemical behavior, and further improves the controllability of discharging activity during the machining process.
- Investigate the mechanism of material removal. Glass is a material with high temperature dependence in thermal and mechanical properties. The goal is to develop understandings of the material behavior under thermal and mechanical impacts from the tool. The outcomes should yield to quantitative models of the cutting force and the material removal mechanism.

1.4 Outline

This dissertation presents observations, results, and modelling of the electrochemical discharge assisted machining process. Chapter 2 presents the development of the EDAC drilling process, including the design and fabrication of the experimental apparatus, drilling tests and comparison to conventional machining technologies, and vibration assisted drilling for higher material removal rate. Attempts are also made to explain the challenges in conventional technologies and the advantages that pertain to the developed EDAC process. Mechanism for material removal is also qualitatively revealed through experimentation and observation.

Chapter 3 introduces the EDAC milling process. Experimentation and data analysis are used to validate the feasibility and viability of the EDAC in glass milling. Efforts are made to fabricate three dimensional shapes with decent surface integrity and geometric accuracy. The discussion is focused on the achievable precision of the process, including overcutting and geometric accuracy, to explore the capability and limitations of the process.

Chapter 4 provides a physics-based model of the electrochemical discharge phenomenon, targeting at a deeper understanding of the fundamentals of the EDAC. Two key elements are investigated: the gas film and the discharging energy. Models of the gas film are established based on the fluid dynamic behavior of bubbles, and the evolution from bubbles to the gas film. Discharging energy of sparks is experimentally determined with the assistance of a sharp tool electrode fabricated by ECM. The energy and spatial distributions of sparks are mathematically modeled.

A material removal model is introduced in Chapter 5, highlighting the temperature profile and the cutting force. A material heat transfer model is proposed to investigate the temperature profile of the material and to further determine the temperature dependent mechanical properties. A cutting force model is proposed to predict the cutting force as a function of time in the process. The model includes intrinsic equations to simulate the viscous fluid behavior of material, as well as generic chip formation estimations to address the issues of overcutting by thermal energy.

Conclusions and recommendations for future study are presented in Chapter 6.

Chapter 2

Micro Drilling by Electrochemical Discharge Assisted Cutting

2.1 Introduction

One of the major challenges of ECDM is the low material removal rate. In a conventional electrochemical discharge drilling process, the material removal rate drops significantly as the machining depth increases. Variations of ECDM, including changing the tool and the process, can potentially improve the material removal rate. Han et al. (2009) applied ultrasonic vibration to the tool electrode and studied the mechanism of gas film generation under vibration. Huang et al. (2011) employed a drill bit as cathode in machining, and studied machining of metal. Cheng et al. (2010) embedded ECDM into a magnetic field that regulated micro-flow of electrolyte during drilling process. Tool variations could also affect the performance of ECDM. Cheng et al. (2010) used a tool electrode with flat sidewall and experimentally validated that the revised geometry could aid spark generation. Yang et al. (2013) designed and fabricated an electrode with a spherical end, which enhanced the material removal rate and accuracy.

In this chapter, micro-drilling processes facilitating electrochemical discharge assisted cutting (EDAC) are discussed. Conventional ECDM removes material only by electrochemical discharge, resulting in low material removal rates, limited machinable depth, and undesirable

surface finish. By incorporating mechanical drilling, the drilling performance can be significantly improved. As a hybrid machining process combining ECDM and cutting, the material removal rate is significantly enhanced. Drilling throughput and the material removal mechanism is analyzed with emphasis on comparison with conventional ECDM. Tool vibration is enabled that further improves the material removal rate especially in drilling deep holes. Experiments are conducted to determine process parameters to increase material removal rates.

2.2 Experimental setup

An experimental apparatus that implements electrochemical discharge machining is designed and fabricated (Figure 2.1). The apparatus is adapted to an EDM machine (EDM solutions, 416 NC10 PLC2000), with the addition of a micro-precision spindle, a fixture, external power supply, and electro-chemical chamber. The micro-drill bit, which also serves as the working electrode, is mounted on the spindle. A motor is employed to enable tool rotation with a maximum runout of 10 μm. The workpiece is clamped on a rigid acrylic fixture. The fixture is designed particularly with high stiffness and surface flatness to minimize the turbulence to electrolyte flow during drilling process. A three-axis dynamometer (Kistler 9256C) measures the contact force during the machining process, and enables constant-force feeding in drilling.

The fixture is immersed in a chamber filled with electrolyte. The tool and the auxiliary electrode would trigger electro-chemical discharge once an appropriate DC voltage is applied. Spindle consists of a piezo-actuator connected with a ball spline bearing, providing vibration up to 20 kHz with a maximum load of 3 kN. The motor provides rotation up to approximately 3000

rpm to the spindle through belt transmission. A LVDT displacement sensor measures the displacement of the fixture. The bandwidth of the LVDT sensor is limited to 80Hz due to the fact that the sensor is mechanically pushed against the measurement surface using a built-in spring. The maximum range of the sensor is 2 mm, and the accuracy is 1 µm. Data acquisition is through National Instruments data acquisition system to record electrode voltage, electrode current, contact force, and tool displacement, with a sampling frequency of 1000 Hz.

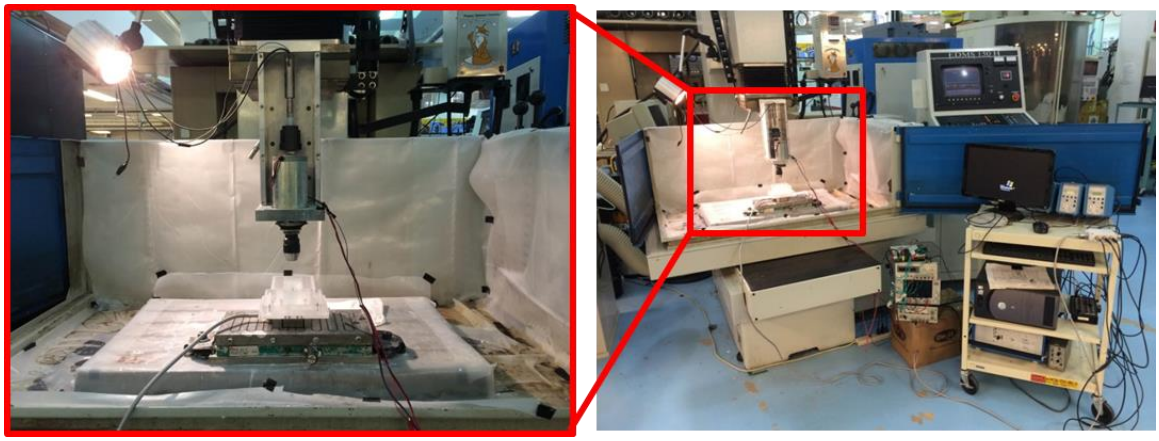

Figure 2.1. Experimental setup of the EDAC.

The electrochemical chamber (Figure 2.2) is designed with an immersion control mechanism to prevent inaccuracy due to the loss of electrolyte. The workpiece sits at 1 mm blow the edge of the chamber when tightly mounted. When the chamber is fully filled with electrolyte, the immersion depth will reach about 2 mm due to surface tension. The evaporative loss of electrolyte is negligible during experimental studies therefore no compensation is necessary. However, if the system is being operated through long hours, a small pump that refills the electrolyte can keep the workpiece maintained at constant immersion level.

There are two types of feeding mechanisms available in ECDM: constant velocity and constant force. If a drilling process enables constant velocity feeding, as implied by name, the

drill bit moves downward at a preset velocity. In such case the feed velocity has to be lower than the material removal capability through the entire drilling process. Since the material removal rate in ECDM decreases drastically as the hole gets deeper, the feed velocity has to compromise the minimal material removal rate at the late stage of drilling and therefore the potential of drilling cannot be fully utilized.

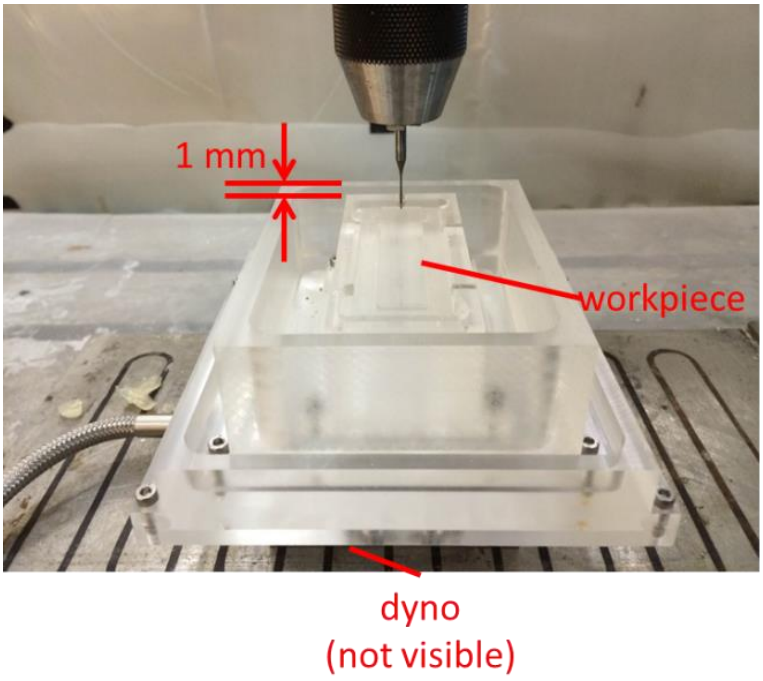

Figure 2.2. Fixture and the electrochemical reaction chamber.

On the other hand, constant force feeding is a more popular feeding option in ECDM drilling. A constant force is maintained between the tool and the workpiece. A widely used approach to enable constant force feeding is gravity (Figure 2.3). The entire fixture sits on a rail with linear bearing that enables vertical movement. The fixture is connected to a counter-weight using a pulley system. The gravity feed apparatus is designed and fabricated to serve the drilling processes.

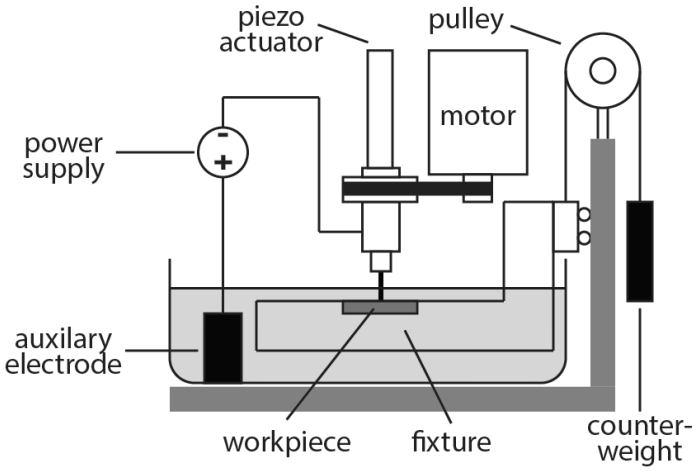

Figure 2.3. EDCM drilling setup with gravity feeding.

The gravity feed system, however, may have potential undesirable behavior, including

- The counter weight does not always provide a constant contact force. The total mass of the counter weight equals to the mass required to balance the fixture, plus the desired contact force. However, when the fixture moves upwards in the drilling process, the acceleration in motion can change the tension of the connecting string, resulting in a varying contact force.
- The fixture has a cantilever beam structure that may cause a non-negligible deflection at the drilling point. The deflection comes from either the low rigidity of the fixture material (typically acrylic for electrical resistance) or the clearance of the linear bearing and carriage.

After some design iterations, the gravity feed device eventually overcomes the weaknesses listed about. A steel string is used to connect the counterweight to maximize the stiffness of the string. And the fixture is designed to be mechanically rigid so that the deflection is measured to be less than 5 μm under 2 N contact force.

An alternative approach to realize constant force feeding is to track the feedback from the dynamometer and control the position of the tool. However, the minimum programmable resolution for vertical movement is 2 μm. Due to the high rigidity of the tool and the fixture, a movement of 2 μm can cause the variation of the reaction force to reach 4 N, which is very high compared to commonly desired contact forces of 1 - 2 N. Therefore the closed loop control method is not feasible with the current apparatus.

Constant velocity feeding can be used for general purpose EDAC drilling, while constant force feeding is the only option to maximize the material removal rate. Therefore all drilling experiments presented in this chapter use the constant force feeding.

2.3 Experimental procedures

Drilling experiments are conducted to investigate the characteristics of the EDAC. Conventional ECDM drilling with stationary cylindrical tool creates a benchmark for the hybrid process of the EDAC with incorporation of mechanical micro-drilling. The comparison between conventional and the EDAC reveals the reason behind the huge enhancement of material removal rate throughout the process.

Electrode voltage in ECDM drilling is critical to material removal rate and machining quality. Higher voltage can increase the material removal rate, but can also create large overcuts and damage the surface integrity. It is determined that 30 to 40 V is a range for electrode voltage that ensures a relatively high material removal rate and prevents cracks and large overcutting (Wüthrich & Fascio, 2005).

A cylindrical tungsten-carbide rod with 0.5 mm diameter is used as electrode tool in conventional ECDM drilling experiments. Tungsten-carbide is used here due to its high thermal resistance and chemical inertness (Yang et al., 2010). Soda-lime glass specimen (SiO_2- Na_2O - CaO system, 74 wt. % SiO_2, 13 wt. % Na_2O, 10.5 wt. % CaO) with 1 mm thickness is chosen as workpiece in the drilling. The specimen is immersed 2 mm under the electrolyte (30 wt. % NaOH, if not specially indicated).

In the EDAC drilling experiments, a tungsten carbide micro-drill bit is employed as a discharging electrode with the same nominal diameter as the cylindrical tool (Figure 2.4). The drill bit is driven forward using a DC motor. Mechanical material removal takes place through tool rotation during ECDM process. Rotary velocity of spindle ranged from 100 to 400 rpm.

Electrode voltage is set to 30, 34, 38 V. Conventional ECDM is ineffective under 30 V electrode voltage. However, with the involvement of mechanical drilling, the material removal rate has the potential to reach an acceptable range.

Drilling specimens are observed using optical microscope (model: Nikon Optiphot Planar Microscope with Nikon Digital Insight DS-L2) and scanning electron microscope (SEM, model: FEI (Philips) XL30 with BSE mode and EDAX analysis). Platinum layers with 20 nm in thickness are sputtered on the specimens in advance to using electron microscope. The specimens are tilted by a 30 degree angle to achieve intuitive visual effects.

In these experiments, four holes are drilled to pre-heat the tool and electrolyte after loading a new glass specimen. It is noticed that the material removal rate for the first few holes drilled is slightly lower than steady state. Preheating would help creating a stable ambient for

machining and enhance the repeatability of the experiments. Drilling is repeated for 3 times under each machining configurations.

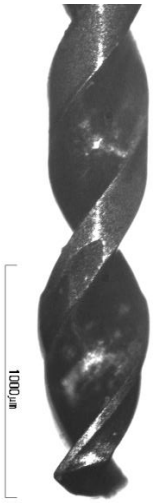

Figure 2.4. The micro drill bit with 500 µm diameter.

2.4 Experimental results

Blind hole drilling experiments are conducted. As a conventional way of ECDM process, drilling with a stationary cylindrical tool is used as a benchmark for the EDAC drilling (Figure 2.5). The comparison between conventional ECDM drilling and the EDAC drilling revealed the material removal rate and material removal mechanism throughout the process.

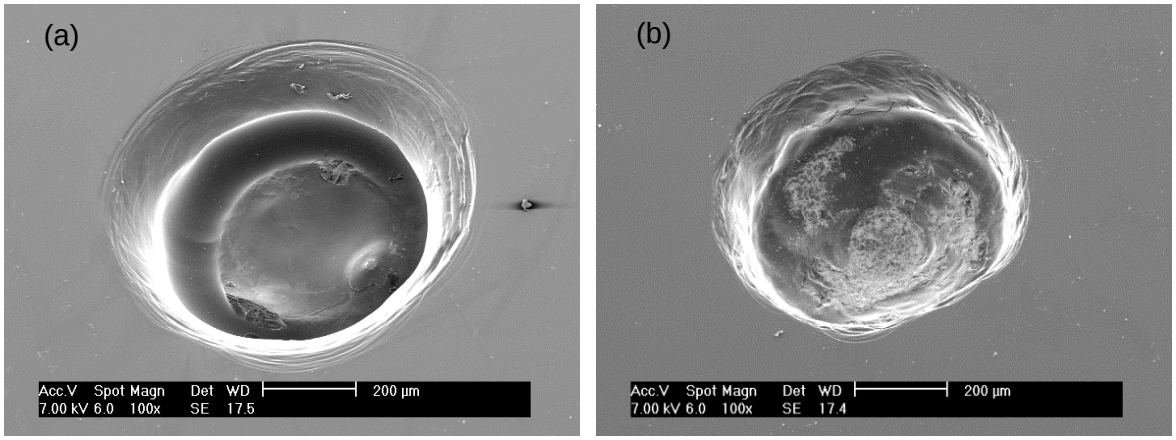

Figure 2.5. Micro holes drilled by (a) conventional ECDM drilling and (b) EDAC drilling.

When the cylindrical electrode contacts the workpiece, material near the edge of the electrode is removed first, forming an undesired circular groove. In the EDAC drilling, however, the bottom of the hole is mechanically scratched severely, indicating mechanical material removal at the bottom.

Figure 2.6 shows typical curves of machining depth versus machining time of conventional ECDM using cylindrical tool. As seen in the figure, the material removal rate is inconsistent throughout the machining process. The burst increment of machining depth occurs periodically and the feeding rate slows down until next burst takes place. This suggests a discontinuous material removal mechanism throughout the drilling process. This is not true when micro-drilling is incorporated, however. Figure 2.6 demonstrates that the rate of material removal changes continuously during the machining process, indicating different material removal mechanism from conventional ECDM drilling.

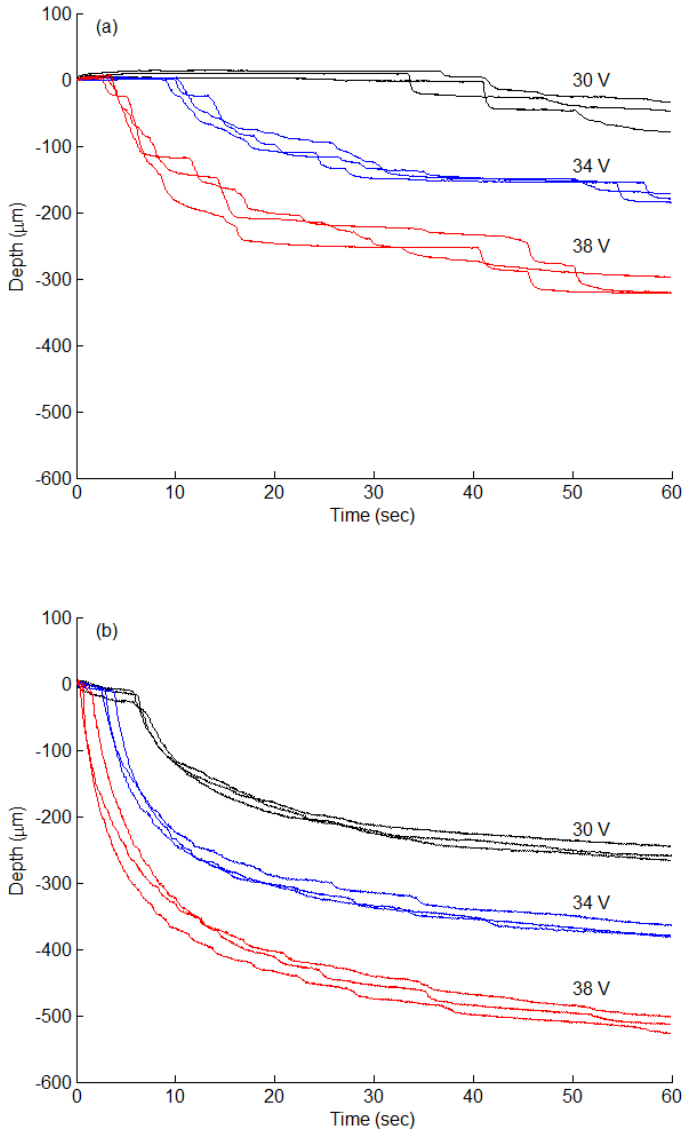

Figure 2.6. Machining depth curve of (a) conventional ECDM drilling and (b) EDAC drilling.

Figure 2.6 also demonstrates that electrode voltage significantly affects drilling efficiencies in initial stages. It takes over 30 seconds until detectable feeding occurs with low electrode voltage (30 V). The delay is reduced to less than 4 seconds with high electrode voltage (38 V).

Based on the observations from drilling experiments, a hypothesis model for material removal in ECDM drilling is proposed, as illustrated in Figure 2.7.

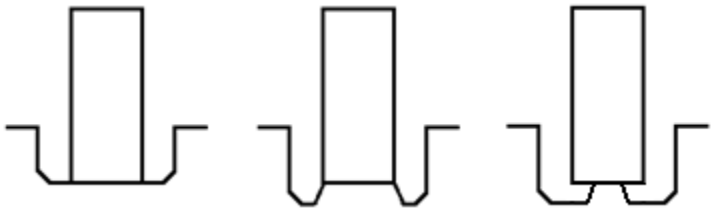

Figure 2.7. Schematic of material removal in conventional ECDM drilling

Material around the edges is removed first, and the material remained at the center became a pivot that supports the tool electrode. When the cylindrical tool is in contact with the workpiece, material removal rate is higher around the edge, because the electrical field intensity is stronger at sharp edges. Discharges at the edge remove material around the cylindrical tool, while minor discharges at the center removes the material at a slower rate. Hence the remaining material at the center becomes a pivot that supports the tool. However, with more material being removed, the pivot becomes smaller in diameter, and eventually loses strength to sustain the feeding force. Then a collapse occurs, corresponding to a burst inn the machining depth - time plot.

The same phenomenon can also be observed in material removal simulation. The simulation is discussed in detail in Chapter 5. Figure 2.8 shows the simulated process of material removal at the beginning of the drilling. The temperature contours represents the boundary of the removed material.

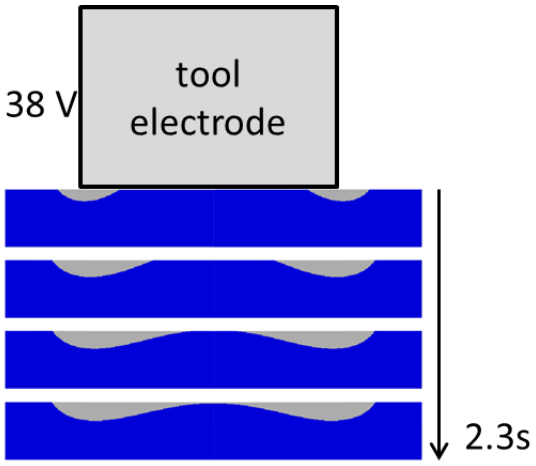

Figure 2.8. Cross-section of the removed material.

To further test this hypothesis of material removal mode, SEM images of micro holes drilled by a cylindrical tool at different machining times were taken (Figure 2.9). When the cylindrical electrode contacts the workpiece, material near the edge of the electrode is removed first, forming a circular groove. The pivot at the center reduces in size as the groove grows. The machining depth indicated on the curve (Figure 2.6) is actually the height difference between the pivot and the surface of the work piece.

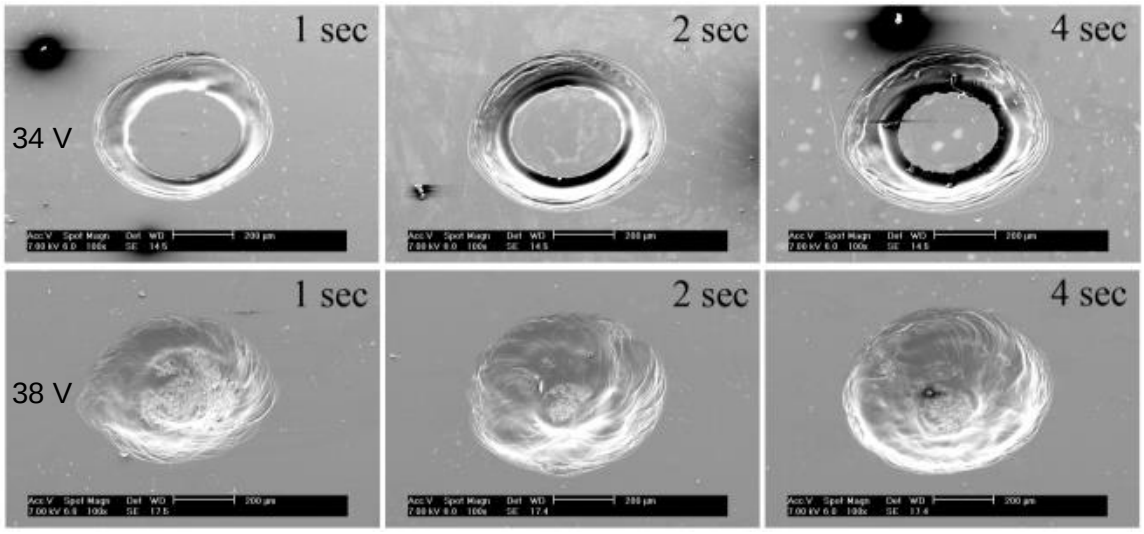

Figure 2.9. Craters drilled under short machining time, under 34 V and 38 V electrode voltage

Figure 2.10 compare the cross-sectional view of holes drilled by conventional ECDM and by the EDAC drilling. Lines in the figures represent the size of 500 μm tools. This further proves the existence of the pivot for holes machined from conventional ECDM, whereas holes created with micro-drilling have flat bottom surfaces. The delay in feeding during conventional ECDM is due to support from the pole at the bottom, which is an inevitable outcome through electrochemical discharging. In micro-drilling incorporated ECDM, the machining curves are smooth since material at the center of bottom is mechanical removed and poles are not created.

The holes present in Figure 2.10 are approximately 700 μm in diameter, while the diameter of our drilling tool is only 500 μm. Apparently material out of a circular range of 500 μm is not mechanically removed. Therefore, an appropriate explanation for material removal in micro-drilling incorporated ECDM is that: (1) Material in the range of a 500 μm circle from the center is dominated by mechanical material removal. (2) Material outside that range is electrochemically removed.

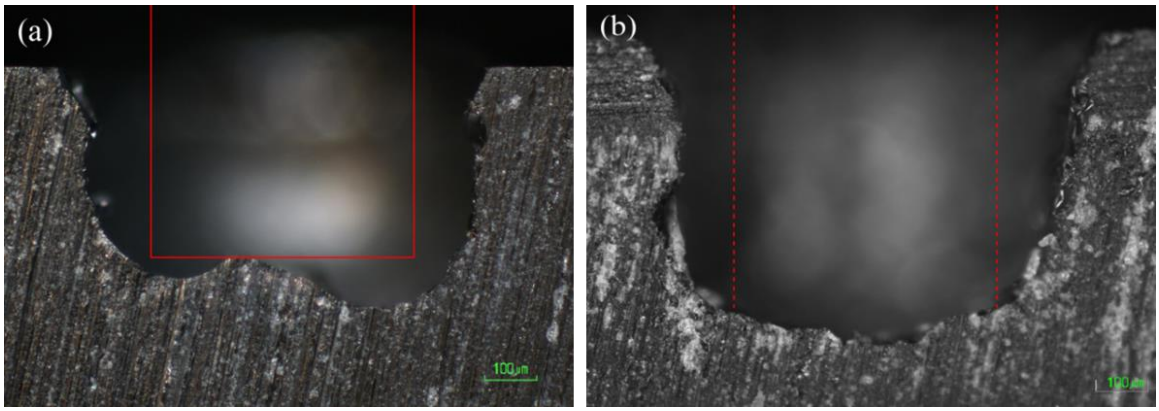

Figure 2.10. Cross-sectional view of holes drilled by

(a) conventional ECDM drilling and (b) EDAC drilling.

Material removal rate in both ECDM and EDAC drilling is very sensitive to electrode voltage. The tradeoff using high electrode voltage is the overcutting and the risk of thermal cracks. Figure 2.11 is a perfect example to illustrate the effects of electrode voltage. Both holes are drilled over one minute. Under 30 V electrode voltage, the hole looks almost defect-free, while the depth is also significantly lower than the hole drilled with 38 V electrode voltage. The optimal electrode voltage depends on the specific requirements of whether higher material removal rate or surface finish is more desirable.

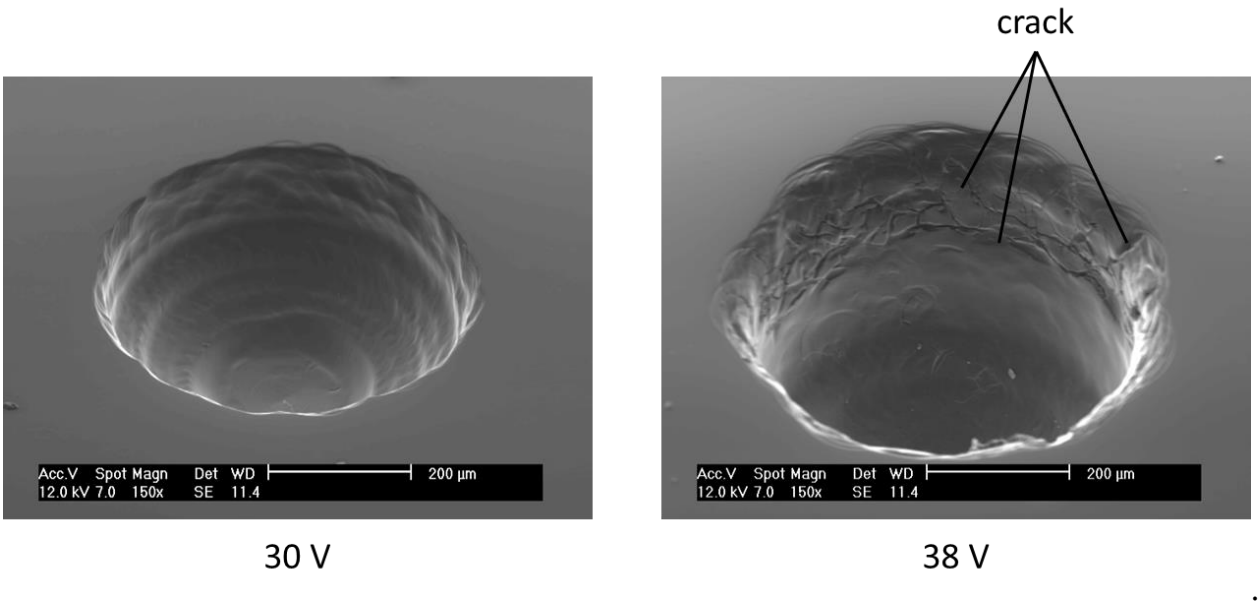

Figure 2.11. Surface finish of low vs. high electrode voltage.

The rotary speed of spindle could also affect the quality and efficiency of machining. Tool rotation with higher speed increases material removal mechanically. Meanwhile, high speed rotation tends to break the gas film and therefore reduces electrochemical discharge. Figure 2.12 shows the machining depth over one minute under various process parameters. The machining depth is significantly lower under 400 rpm spindle rotation, comparing with 100 rpm rotary speed. A detailed discussion about the process parameters is presented later in this chapter.

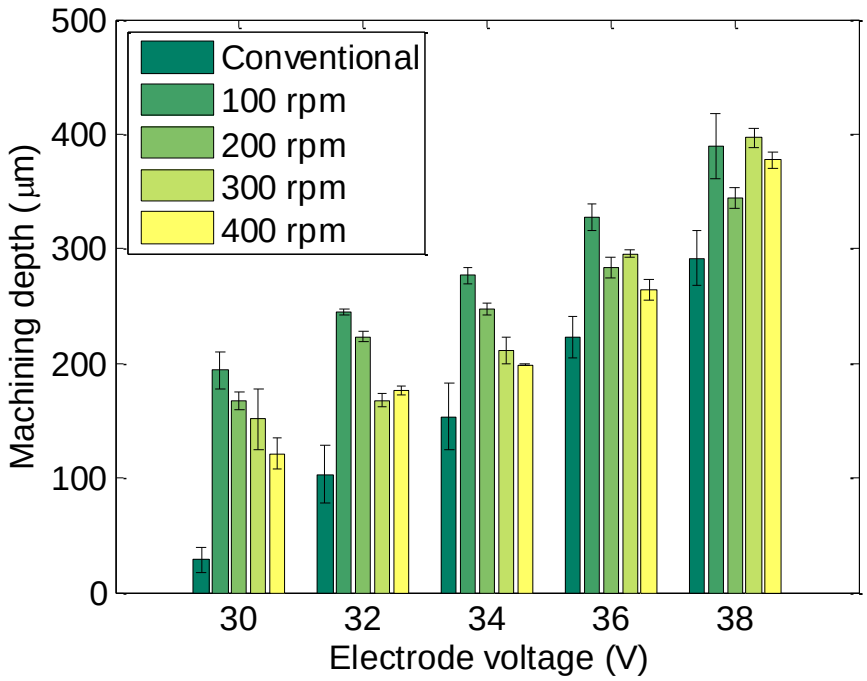

Figure 2.12. Machining depth over one minute.

The average machining depth over 1 minute for conventional ECDM under 30 V, 34 V, 38 V electrode voltage is 29 m,153 μm, 292 μm, respectively. When incorporating micro-drilling, the average machining depth increases to 194 μm, 277 μm, 389 μm, respectivley (the rotary speed of spindle for micro-drilling is 100 rpm, and all other configurations are same to experiments with conventional ECDM). It proves that the EDAC enhances the through put of drilling considerably.

2.5 Vibration assisted drilling

Material removal rate is significantly increased using micro-drilling tool in ECDM. However, the material removal rate, reflected as feed rate on the drilling curve, decays with the increment of machining depth. A potential solution to this issue is to introduce tool vibration to

the machining process (Wüthrich et al., 2006). The piezo-actuator on the spindle can vibrate the tool electrode at a wide range of frequency and amplitude. Vibration waveforms can affect the machining process. Square wave is employed in the experiments. Several parameters of vibration are taken into consideration: frequency, amplitude, and duty ratio.

An example of machining curves of vibration assisted drilling under different electrode voltage (vibration waveform is a 160 Hz square wave with 50% duty ratio, 20 μm amplitude) is presented in Figure 2.13. It can be seen that the machining curve is smooth comparing with those of conventional ECDM, which indicates that mechanical material removal is preserved in the vibration assisted drilling process. The major difference on material removal rate by introducing vibration is that the machining depth increases almost linearly after about 10 seconds. In conventional and drilling assisted ECDM, material removal is suppressed as machining depth increases, resulting in a limitation in maximum machinable depth.

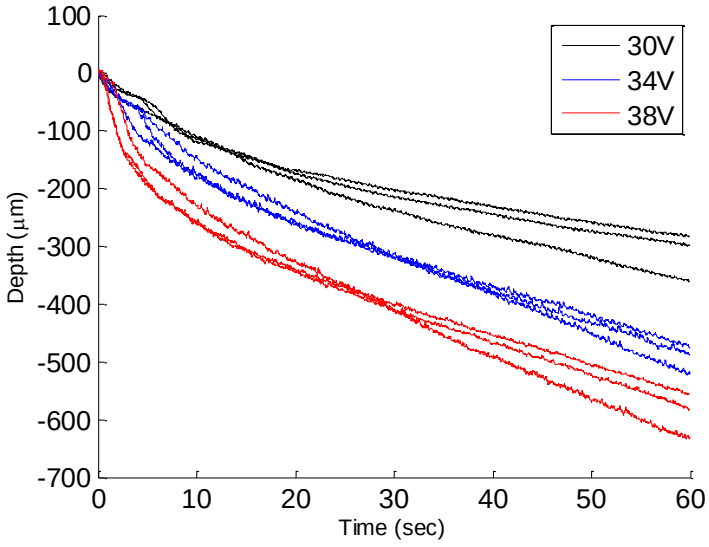

Figure 2.13. Drilling depth curves with vibration.

The reason for the increased machinable depth in deeper hole drilling is that vibration helps replenishing the electrolyte in the hole. Without vibration, it is hard for electrolyte to flow into a deep hole. The helical groove of the drill bit is designed to push out the removed chip, but meanwhile it removes the electrolyte in the hole as well. Vibration solves this issue and therefore the drilling process maintains a steady material removal rate with the hole getting deeper.

Vibration compromises material removal by electrochemical discharge because vibration increases the tendency of bubble departure from tool electrode, and therefore impairings gas film formation and discharge. In the initial period of drilling process, in which the electrochemical material removal dominates, vibration negatively affects the material removal rate (Figure 2.14). The reduced discharge lowers material removal by sparks. As machining depth increases, the machining depth of vibration assisted drilling catches up and surpasses that of drilling without vibration.

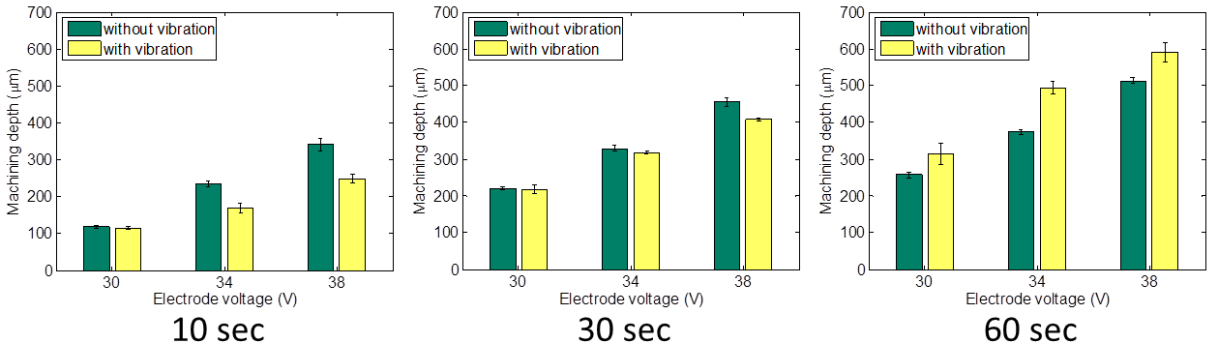

Figure 2.14. Drilling depth under 10, 30, and 60 seconds etching time.

Another tradeoff of using vibration is that it compromises surface finish. Figure 2.15 demonstrates an EDAC drilling hole with vibration. It can be seen that the bottom of the hole is very rough, indicating brittle material removal at the bottom surface. This is a result of the

hammering effects of the mechanical vibration. The brittle removal is very undesirable due to the fact that it gives chance to uncontrollable cracks and sub-surface damages.

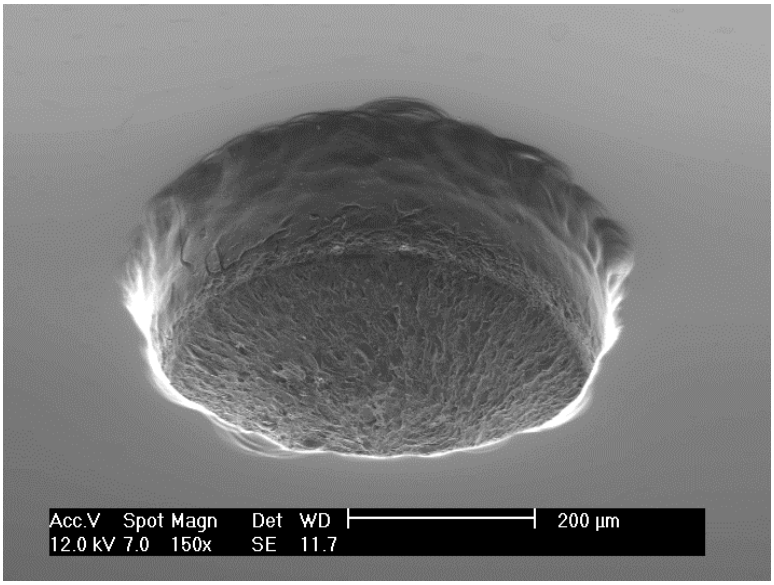

Figure 2.15. A hole drilled with vibration.

2.6 Process parameters

There are several process parameters involved in the EDAC drilling with vibration. Electrode voltage, as a direct input of electrochemical reaction and discharging activity, can significantly change the material removal characteristics. In addition, spindle speed can affect the machining quality and machining throughput as discussed in the previous section. Meanwhile, parameters related to vibration also have impacts on the machining process. With higher vibratory amplitude and frequency, mechanical cutting power is enhanced, while weaker vibration can provide better discharging. Duty ratio of vibration waveform determines the percentage of time that tool and workpiece are in contact during the drilling process.

A 3-level Taguchi design of experiment (DOE) is conducted with five factors: spindle speed (2-level), electrode voltage, frequency of vibration, amplitude of vibration, duty ratio of vibration. The reason for using Taguchi DOE instead of full factorial design is due to the fact that a full factorial experiment contains 162 combinations of variables. The values of choice are listed in Table 2.1. The experiments are designed with L18 orthogonal array (Table 2.2), with three replications under each combination of parameters.

Table 2.1. Process parameters in Taguchi DOE.

	Level 1	**Level 2**	**Level 3**
Spindle speed, ω (rpm)	100	200	N/A
Electrode voltage, V (V)	30	34	38
Frequency, f (Hz)	20	160	320
Amplitude, A (μm)	10	20	30
Duty ratio, μ	0.2	0.5	0.8

The main effects of factors on mean machining depth are analyzed (Figure 2.16). The results indicate that electrode voltage is rank 1 in significance among all factors, followed by amplitude and frequency of vibration. It is intuitive that higher voltage yields more machining depth because discharge energy is closely related to electrode voltage. The amplitude and frequency of vibration, however, demonstrate a non-monotonic trend. Moderate choices of vibratory parameters (160 Hz frequency, 20 μm amplitude) enhance material removal rate considerably. Quantitatively, the average machining depth under 30 V, 34 V, 38 V is 384 μm, 469 μm, 512 μm, which is considerably superior to 58 μm, 178 μm, 315 μm by conventional ECDM, with improvement percentage of 562%, 163%, 60%, respectively.

Table 2.2. L18 array for Taguchi DOE.

No.	ω	V	f	A	μ
1	1	1	1	1	1
2	1	1	2	2	2
3	1	1	3	3	3
4	1	2	1	1	2
5	1	2	2	2	3
6	1	2	3	3	1
7	1	3	1	2	1
8	1	3	2	3	2
9	1	3	3	1	3
10	2	1	1	3	3
11	2	1	2	1	1
12	2	1	3	2	2
13	2	2	1	2	3
14	2	2	2	3	1
15	2	2	3	1	2
16	2	3	1	3	2
17	2	3	2	1	3
18	2	3	3	2	1

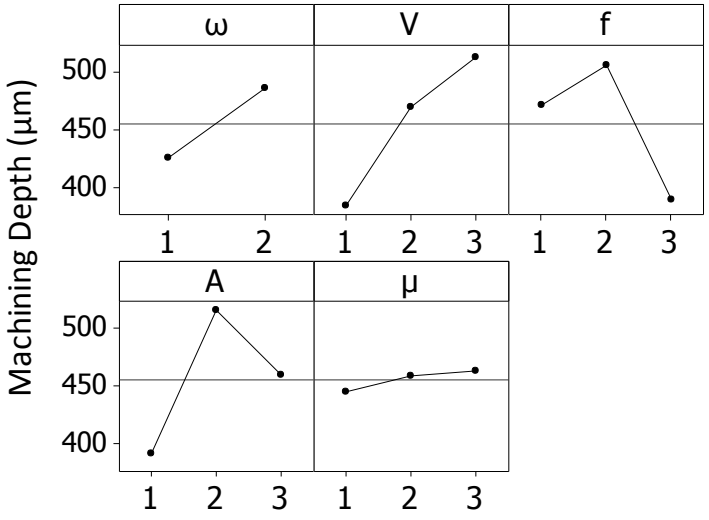

Figure 2.16. Mean machining depth by Taguchi DOE.

2.7 Conclusions

This chapter summarizes motivation, methodology, experiments, and analysis of micro-drilling incorporated electro-chemical discharge manufacturing. The experimental apparatus is designed and fabricated to machine 1 mm thick glass specimen. Conventional ECDM experiments are used as benchmarks for the EDAC. Quantitative measurements throughout the process have been collected to characterize the material removal rate and mechanism.

Material removal mechanism for both conventional ECDM and EDAC is analyzed. Discontinuity in feeding during conventional ECDM is found and is resolved in micro-drilling incorporated ECDM. Therefore, the machining speed for the EDAC is significantly enhanced in comparison with conventional approaches by fundamentals of the material removal mechanism.

Vibration assisted drilling is introduced. Tool vibration establishes steady material removal scenario as machining depth increases, whereas conventional ECDM is limited by

maximum machinable depth. On the other hand, mechanical vibration compromises gas film formation and discharging. The optimal parameters of vibration are determined by the results of the design of experiment. It can be also concluded the improvement of drilling with vibration in terms of machining depth over one minute is 60% or higher, depending on electrode voltage.

Chapter 3

Micro Milling by Electrochemical Discharge Assisted Cutting

3.1 Introduction

There are many technologies that are viable for glass micro machining, such as lithography, ultra-fast laser cutting, and chemical etching. None of these processes are cost effective due to expensive equipment and maintenance. Electrochemical discharge machining has been developed as a potential process for cost effective three-dimensional micro structuring of glass. Zheng et al. (2007) demonstrated an ECDM milling process facilitating rotary tool electrodes and obtained 3D microstructures on glass. However, the material removal rate of the process still needs to be improved. The samples (Figure 3.1) were machined using a 200 µm diameter tool, with 1000 µm/min travel rate and 50 µm depth of cut. In other words, it takes up to 30 minutes to complete each of these structures.

Another challenge in ECDM milling is to preserve the surface quality. Due to the fact that the electric discharge distributes non-uniformly at the bottom surface, the surface finish of milling can be very bad. Improving surface conditions has long been an objective for ECDM research. Figure 3.2 shows examples of conventional ECDM milled surface (Abou Ziki et al., 2012).

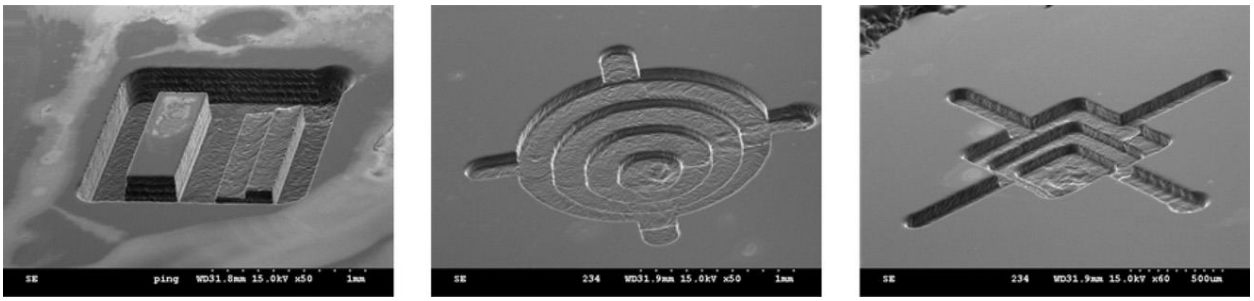

Figure 3.1. Milling process of electrochemical discharge machining.

(Zheng et al., 2007)

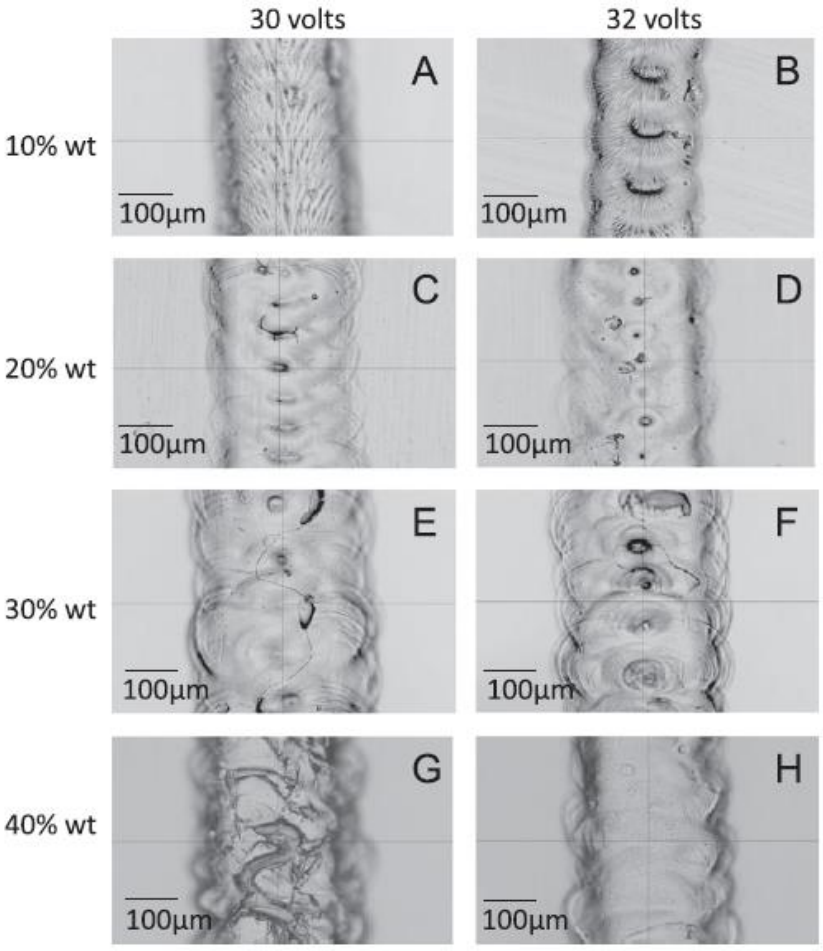

Figure 3.2. Surface conditions of ECDM milling.

(Abou Ziki et al., 2012)

Ductile regime cutting of glass is another viable rapid-prototyping approach to cut glass (Nakasuji et al. 1990, Takeuchi et al. 1996). Foy et al. (2009) demonstrated some groove cutting samples using ductile model micro-milling (Figure 3.3). The ball-end mill adopted has a nose radius of 100 µm, the depth of cut is 16 µm, and the optimal feed rate is determined to be less than 320 µm/min. Although the surface quality can be preserved using ductile mode cutting, the material removal rate must be significantly enhanced to fulfill the requirements of rapid prototyping.

On the other hand the quality of the machined product from ductile cutting is good in terms of surface roughness and integrity. It can be visually indicated that the grooves have low proportion of fracture failure, minimum sub-surface damage, and good surface roughness (Ra < 0.2 µm). This makes ductile regime cutting to be suitable for fine machining rather than removing high volume of material.

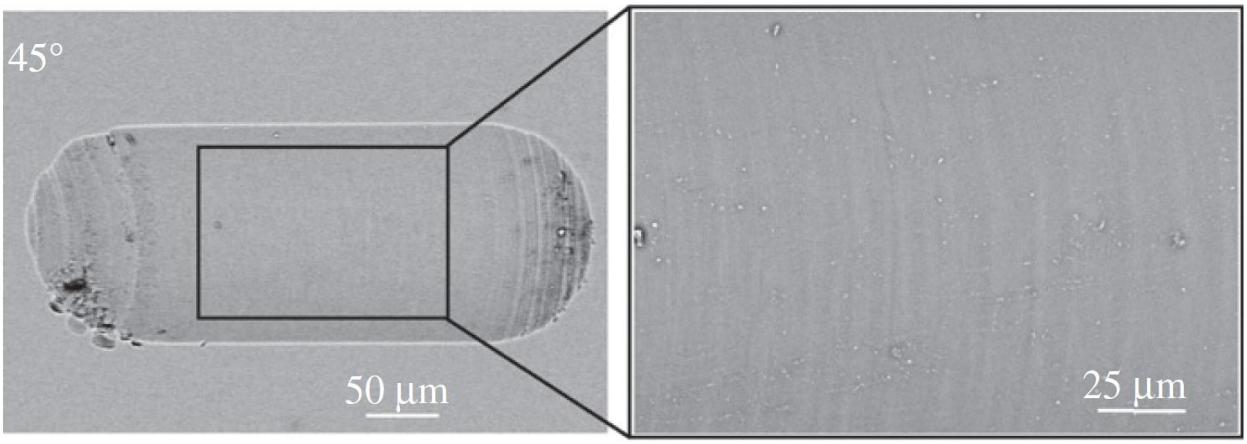

Figure 3.3. Groove cutting of ductile mode milling (Foy et al., 2009).

In this chapter, the milling process facilitating electrochemical discharge assisted cutting is introduced. The combination of mechanical cutting and electrochemical discharge enables

rapid removal of material. Using similar tool size as those in the examples above, the material removal rate (MRR) has been enhanced significantly.

3.2 Experimental setup

The EDAC milling experiments are conducted on the setup introduced in Chapter 2. The machining system is designed to be compatible for both drilling and milling processes. The features specifically designed for milling include the three axes CNC control over the fixture as well as the dynamometer to measure the reaction forces on the tool electrode. Although the dynamometer is mounted at the bottom of the fixture, the fixture is very rigid and therefore the cutting force can be transmitted to the dynamometer with minimal loss.

It is essential to choose an appropriate drill bit for the EDAC process. Since the drill bit performs cutting and releases discharging simultaneously during machining, the desired properties of a machining tool are:

- The material of the tool should resist the high temperature of electrochemical discharging.
- Discharging activity should be restricted to cutting edges only to prevent heat loss and to achieve high energy efficiency in cutting.
- The tool should enable continuous cutting otherwise the surface integrity cannot be preserved due to the brittleness of the material.

The most common material for conventional micro-milling tools is high strength carbide steel. However steel is not the optimal choice in electrochemical discharge assisted cutting because of the different working principles of the two processes. In the EDAC, the hardness

required of the drill bit is not as high as traditional cutting. The mechanically removed material is softened by electrochemical discharge and the cutting force is significantly lower than that in traditional cutting as a result. On the other hand, the discharge brings excessive heat to the tool and has a chance to damage the tool as well.

Tungsten carbide is the material well known to offer excellent wear resistance and high melt point. Many studies indicate that tungsten carbide tools can survive intense discharging. Therefore tungsten carbide is the most appropriate tool material for EDAC.

The helical flat end mill is the most common tool in traditional micro-milling. With tungsten carbide, the tool can be employed in the EDAC as well since the cutting mechanism is not very different from traditional cutting. Tool diameters in these experiments range from 200 μm to 500 μm. The reason that tool size cannot be further reduced is because smaller end mills are difficult to fabricate and are rarely commercially available. Figure 3.3 shows the picture of a 500 μm flat end mill. Once the electrochemical reaction is turned on, it can be seen clearly that spark intensity is high only along the tool edges of the tool (Figure 3.4). The concentrated sparks heat up only the material in the machining zone, providing good energy efficiency, and more importantly preventing massive evaporation of the electrolyte due to overheating. The energy distribution of sparks is discussed in detail in Chapter 5.

Using a tool with 500 μm diameter, the feed rate for the EDAC milling can reach 16 mm/min at 100 μm depth of cut. This corresponds to the material removal rate 80 times higher than conventional ECDM milling and 780 times higher than ductile cutting. Table 3.1 summarizes the material removal rate of the machining processes discussed above. It can be concluded that the EDAC is productive in micro-machining in terms of removing large volume

of material, given the fact that the material removal rate is much higher than other machining approaches. Therefore the EDAC milling has the potential to be an effective technology for rough machining.

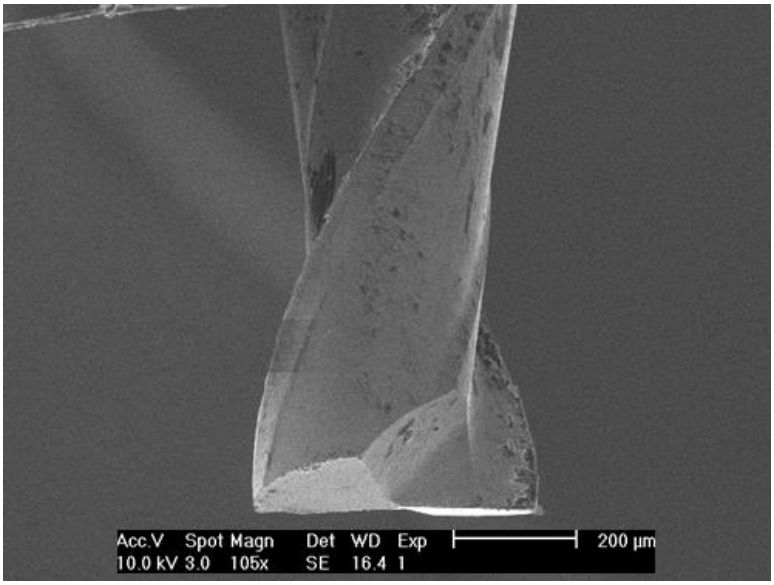

Figure 3.4(a). Flat end mill with 500 µm diameter.

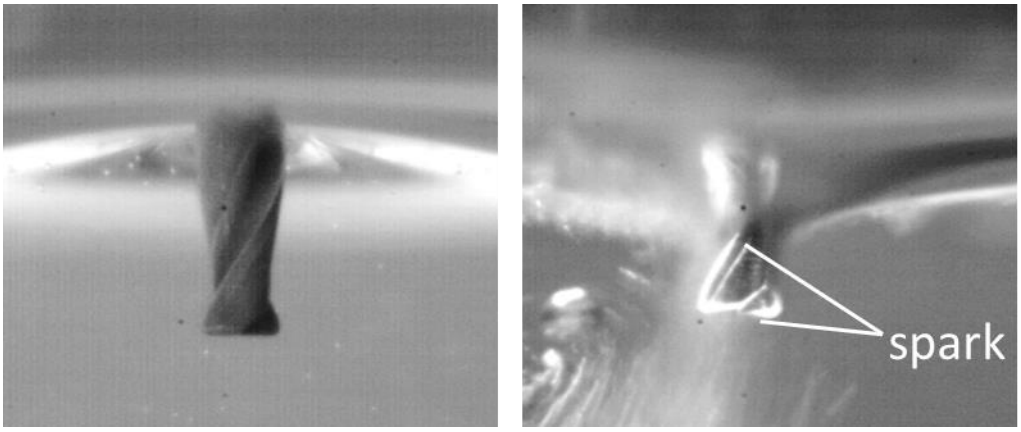

Figure 3.4(b). Electrochemical discharge phenomenon with flat end mill.

Table 3.1. Comparison of current glass machining processes.

Method	Material removal rate (mm^3/min)	Surface finish / Ra (μm)
ECDM	1×10^{-2}	Rough / 3
Ductile cutting	1×10^{-3}	Fine / 0.2
EDAC	*8×10^{-1}*	*Rough / 3*

3.3 Groove cutting

Groove cutting is a basic operation of any milling process. Figure 3.5 shows a groove cutting sample (38 V electrode voltage, 2 mm depth of immersion, 500 μm tool diameter, 160 rpm, 100 μm depth of cut). This section covers the following aspects of groove cutting in the EDAC: procedures, machining accuracy, and machining of complex features.

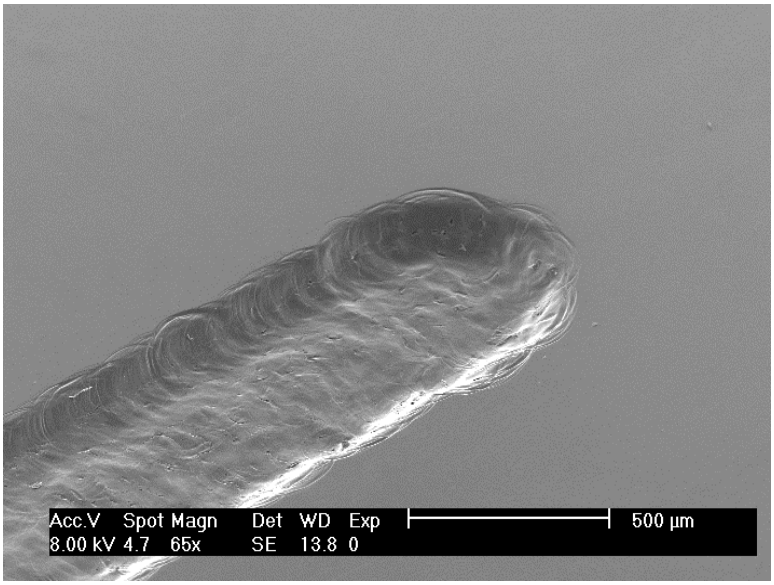

Figure 3.5. Groove cutting sample.

3.3.1 Procedures

Cutting a groove is trivial using conventional milling: plunge the tool into the workpiece and move the workpiece along a certain direction (Figure 3.6(a)), or "side cutting". However, the procedure of groove cutting in the EDAC is not as straightforward.

In many electrical related machining process, EDM for instance, groove cutting is achieved in another way. Instead of facilitating the cutting edges on the side, material removal is the result of electric discharge on the bottom surface of the tool electrode (Figure 3.6(b)), or "bottom cutting". The EDAC features combined material removal from both mechanical cutting and electric discharging. It would be ideal if bottom sparks can be utilized. However, the only way to enable physical cutting is to choose a side cutting approach, as a gap is required between the tool and the workpiece in bottom cutting to enable discharging.

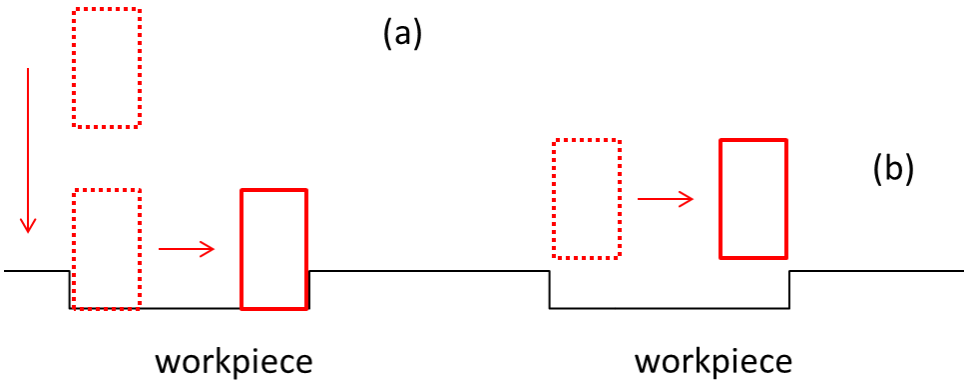

Figure 3.6. Two methods of groove cutting.

3.3.2 Machining accuracy

The important parameters that define the quality of a machining process are the geometric precision and the surface integrity. The inaccuracy in conventional cutting comes from many sources such as machine vibration, spindle runout, and tool damage. These factors also

come into play in the EDAC, but the uncertainty from electric discharges dominates machining behavior. The typical issues concerning material removal by electric discharging narrow down to overcutting and rough surfaces.

Overcutting is inevitable due to the nature of electric discharges as the sparks are always "around" the tool electrode, resulting in a larger area of material removal than the size of the electrode. This overcut can reach hundreds of microns in EDM depending on the electric power applied. However, the overcut is usually consistent during the machining process and therefore can be compensated in the tool path design. Therefore it is essential to determine the overcut under various machining conditions.

On the other hand, rough surface finishes result from craters created by sparks hitting the material. Similar to EDM, the tradeoff of fast material removal is a rough surface. Although many recent studies achieve near mirror surface finishes by EDM, there are many restrictions with these technologies and they cannot be applied to the EDAC. Characterizing surface roughness in groove cutting could contribute to defining the overall machining quality and accuracy.

Investigating the machining overcut and surface roughness is the objective of the EDAC groove cutting. Details are discussed through the following sections.

3.3.3 Overcut

Many factors can change the amount of overcut during the machining process. In experimentation of overcutting, three parameters unique to the milling process are highlighted: the electrode voltage, spindle speed, and feed rate. The size of the flat end mill is 500 μm, same as used in drilling experiments. Spindle speed is set to 160 rpm and 320 rpm, respectively. The

reason higher spindle speeds are undesirable is because spinning increases the instability of bubbles and the gas film and therefore suppresses discharging activity. Such phenomena are detailed in the discussion of process parameters in drilling in Chapter 2. The measurement of overcut is based on grooves with 2 mm in length. Groove cutting is repeated three times under each combination of process variables. The reported value for overcut is the average of three measurement points on the groove: the starting point, the middle, and the end point of the groove.

The cross sections of the grooves are trapezoidal, with a wider opening on the top (Figure 3.8). The overcut on the opening can reach as high as hundreds of microns. However, the bottom surface is not much wider than the size of the mill.

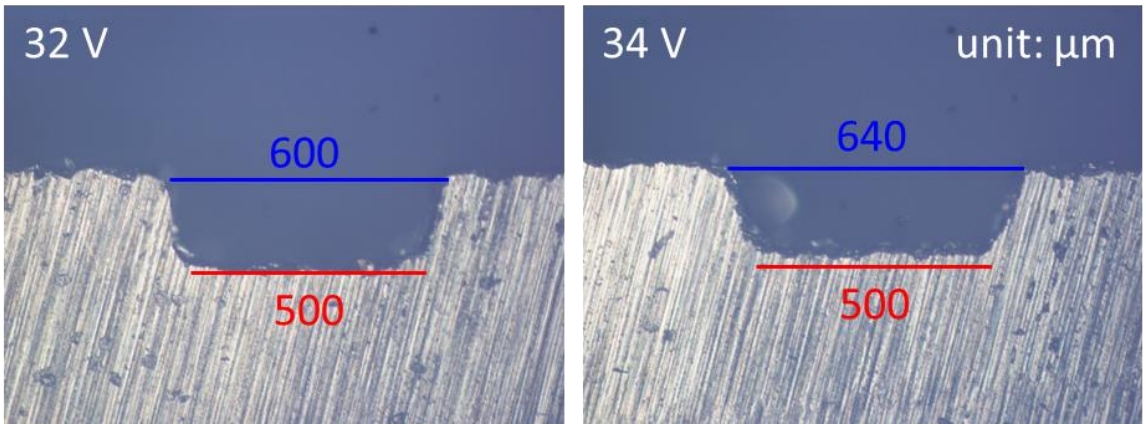

Figure 3.7. Cross sections of grooves under 32 V / 34 V electrode voltage.

By iterating through all combinations of parameters with 2-level spindle speed and feed rate, and 3-level electrode voltage, it appears that electrode voltage is the most significant factor that contributes to overcutting. Such a phenomenon is consistent with the mechanism of material removal in the EDAC milling where overcut comes from sparks around the tool. Higher electrode voltage directly increases the heat input to the workpiece, resulting in larger area of material to be removed by sparks.

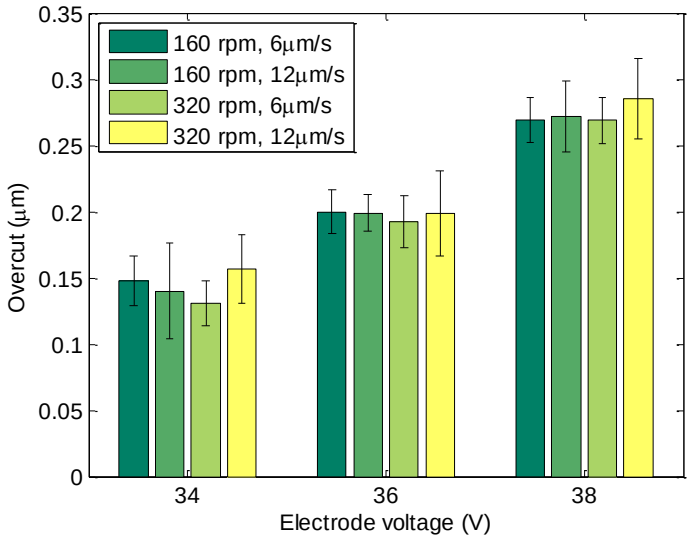

Figure 3.8. Overcut in groove cutting tests.

In traditional milling, milling a flat surface is straightforward. The increment between the groove cuts is usually set to be slightly less than the width of the cut. In the EDAC however, the spacing between the cuts has to be carefully set up due to the thermal overcut. If the spacing is too large, there will be a ridge between two cuts. On the contrary, there will be a groove if the spacing is too small. Figure 3.9 illustrates this phenomenon. In the SEM, the spacing between the cuts equals the tool diameter (500 μm) plus the pre-determined overcut (140 μm). It is determined from experiments that if the spacing equals the tool diameter plus half of the overcut, this issue can be resolved.

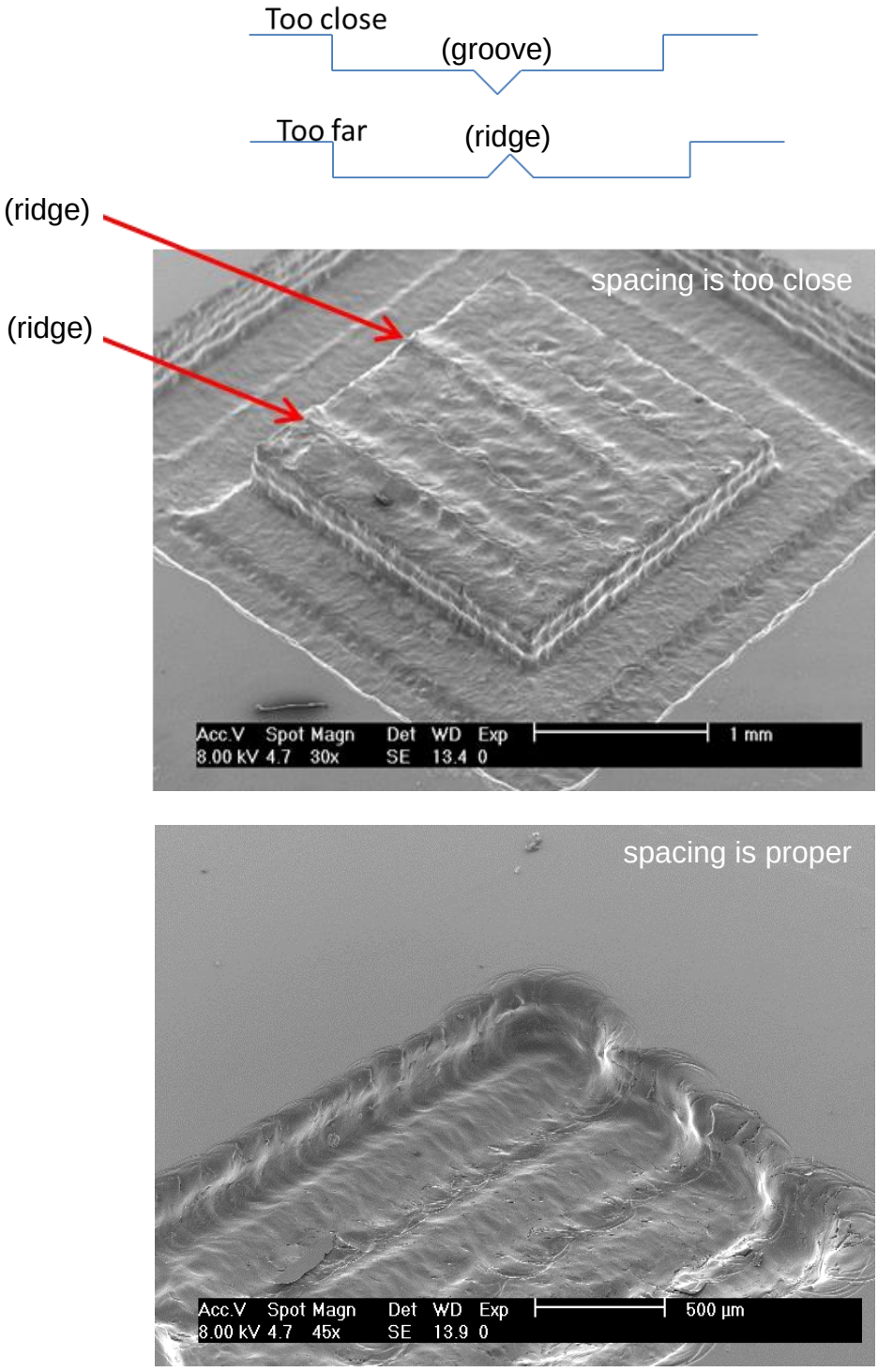

Figure 3.9. Spacing between cuts in surface milling.

3.3.4 Surface roughness

Surface roughness is one of the essential parameters to evaluate the precision of a machined product. In most electrical discharge machining processes, including EDM, the most noticeable tradeoff of high material removal rate is the rough surface finish. It can be visually indicated from Figure 3.5 that the surface finish of the groove is bad in the EDAC where sparks remove significant amounts of material. A quantitative inspection of the grooves is delivered through a white light interferometer (WYKO NT Optical Profiler, results shown in Figure 3.10).

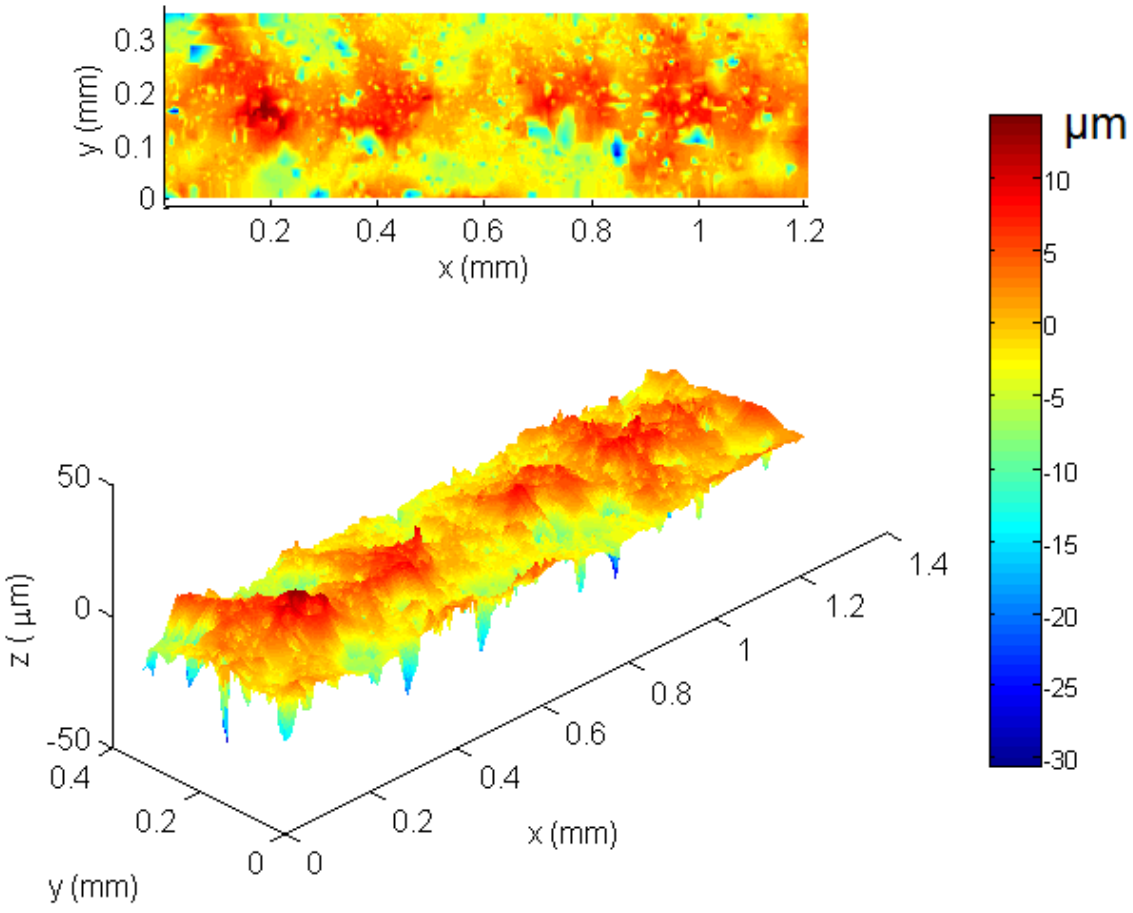

Figure 3.10. Reconstructed 3-D surface.

Several conclusions can be drawn from the surface profile. Figure 3.11 shows the cross sections of the groove. First, the bottom surface of the groove has a “crown feature”, where the center line is higher than the sides by about 10 μm (Figure 3.11(b)). The reason behind the crown feature is that discharging energy is higher at the rims, resulting in more material removal. Such phenomenon is similar to the “pivot” effects in the EDAC drilling, where more material removal takes place around the rim of the tool electrode, but the thickness of the pivot is much higher than the crown.

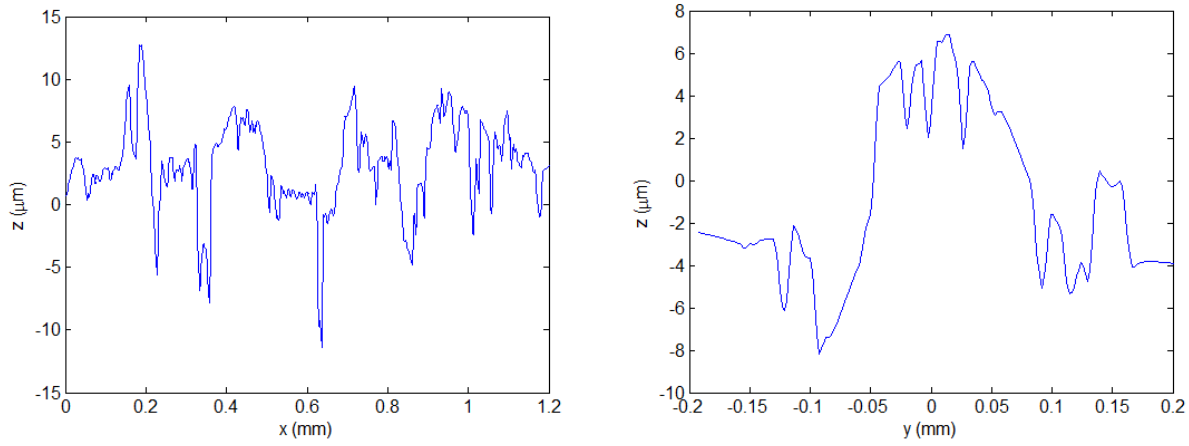

Figure 3.11. Cross sectional views of the groove.

(a) cut along the center line. (b) cut along the cross section

Second, the surface roughness *Ra* is around 3 μm, which is equivalent to that of the machined surface through rough mechanical milling. The reason for such low surface quality is due to sparks. As can be clearly seen from the surface plot, there are many deep small pits indicating the existence of sparks. On the other hand, such surface finish proves that electrochemical discharge assistance is significant in the EDAC milling.

The surface roughness has a correlation with electrode voltage since higher voltage enables stronger sparks. Tests are conducted with the highest electrode voltage to 40 V, which is

the maximum electrode voltage of operation to prevent cracks and subsurface damage. The highest *Ra* value observed is 3.9 µm, while the lowest one is 2.9 µm. Surface roughness data under different electrode voltages are listed in Table 3.2.

Table 3.2. Surface roughness of grooves cut by the EDAC.

Electrode voltage (V)	Ra (µm)	Uncertainty (µm)
36	2.9	0.4
38	3.4	0.2
40	3.9	0.4

In EDM, an easy way to improve surface finish is to reverse the polarity between the electrodes. Anode tool makes a smoother surface, while compromising material removal rate and tool wear. Therefore anode EDM is often used as fine machining. In the EDAC however, changing polarity is not a good way to improve surface finish. The reversed polarity not only changes the electron motion in discharging, but also replaces the hydrogen gas film with oxygen. The oxygen gas film is not as stable due to larger molecular weight and bubble size. It also reacts with the tool electrode at high temperature, especially with steel or copper tools.

3.4 Applications and impacts

The most significant impact of the EDAC milling technology is that it provides a time and cost efficient way of fabricating truly three dimensional geometries with minimum limitation on aspect ratio. The time for fabrication of the hemispherical part shown in Figure 3.12 is about two minutes, which is extremely fast comparing to micro-grinding or other technologies.

Meanwhile the geometric accuracy and surface integrity are preserved along with the high material removal rate. Cracks and sub-surface damages, which are common issues with processing brittle materials, are not noticeable with the EDAC.

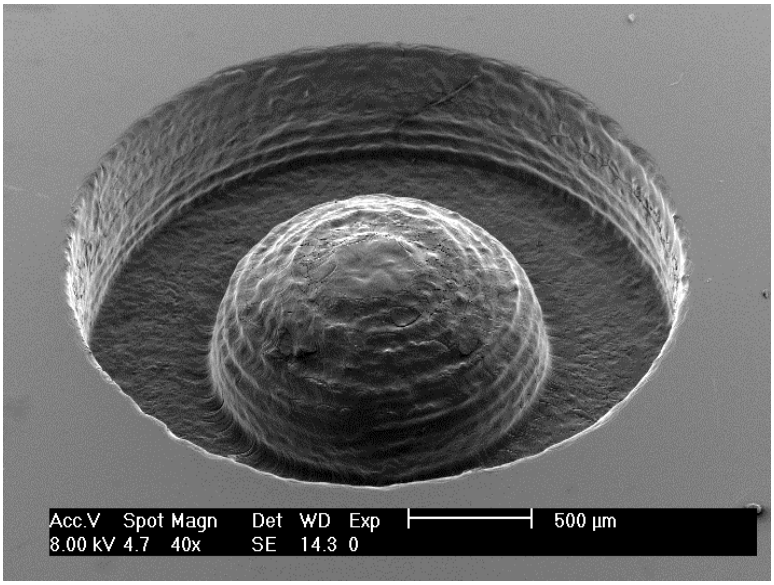

Figure 3.12. Hemisphere machined by the EDAC.

The development of the EDAC not only reduces the time and cost for the fabrication of hard-to-machine materials, but also changes the way people design miniature devices. Current design philosophy in MEMS is “2.5D”, where a product is laminated by limited layers of two dimensional design. Designers have to compromise many mechanisms and structures for manufacturability. The EDAC makes three dimensional fabrication feasible and that might leave a huge impact on future MEMS designs.

3.5 Conclusions

In this chapter, the micro-milling process by electrochemical discharge assisted cutting is introduced. Comparing to existing technologies, the EDAC milling has a much higher material

removal rate in glass cutting, with a decent surface finish and geometric accuracy. By using micro flat end mill as the tool electrode, electrochemical discharge can be combined with conventional cutting for enhanced material removal rate.

Intense sparks are aggregated at the cutting edges of the tool, resulting in minimized overheating and surface damages. Surface finish of the EDAC milling is around Ra 4 μm, which is similar to that obtained in conventional mechanical milling. Overcutting can reach as high as hundreds of microns, but compensation is possible during the stage of tool path planning since overcutting can be quantified given the combination of process parameters.

Chapter 4

Characterization of the Electrochemical Discharge Phenomenon

4.1 Introduction

The EDAC process makes use of the electrochemical discharge phenomenon, which takes place in electrolysis processes. Consider the case of water electrolysis where hydrogen is generated on the cathode and oxygen is generated on the anode. In most scenarios, hydrogen and oxygen are in forms of bubbles in the electrolyte. These bubbles leave the electrodes due to buoyancy to preserve the electrochemical reaction. However, if high electrical power is employed in the electrolysis and the electrodes are small in size, gas bubbles will emerge on electrode surfaces of and form stable gas films, insulating the electrodes. The gas film insulation breaks down under high electrode voltage, releasing thermal energy through electric discharging. This phenomenon is called the electrochemical discharge phenomenon.

In conventional applications of electrolysis, such a phenomenon should be prevented. The EDAC process, however, makes use of the sparks released for machining. Discharge can be restricted to desired locations of the electrode to create very high energy intensity by choosing electrodes with proper geometries. For example, if the cathode is a small cylinder with a high aspect ratio (20 mm in length and 0.2 mm in diameter, for example) and the anode is a large

block, discharge will release at the cathode tip. Material removal will be achieved if a workpiece is placed close to the discharging location.

The polarity in electrolysis can also affect machining quality. In most cases a cathode tool enables faster machining and prevents tool wear, compared to an anode tool (Jain & Adhikary, 2008). In fact, electrochemical discharge phenomenon can be employed with either a cathode or anode tool to achieve material removal. The machining mechanisms of cathode and anode tools are not the same due to different electrochemical reactions at the electrodes, resulting in discrepancy in machining speed, tool wear rate, and machining geometry (West & Jadhav, 2007).

A proper process model for EDAC can benefit from optimization and therefore improve machining speed and quality. Multiple physics are involved in the EDAC process, including electrochemistry, fluid dynamics, and material behavior. Setting up a process model that covers the entire process is difficult because each variable cannot be fully analyzed in EDAC application. A practical modeling approach is to separate the machining process into steps, including gas film formation, discharging activity, energy transfer to workpiece, and material removal.

In this chapter, the study of gas film formation and discharging activity is presented, including the hydrodynamic characteristics of separate bubbles, gas film evolution, the stability of gas film in electrolysis, and discharging energy.

4.2 Nomenclature

A	surface area of tool electrode (m^2)
C	constant (-)
C_b	buoyancy coefficient (-)
C_s	surface tension coefficient (-)
c	electrolyte concentration (wt. %)
d	tool electrode diameter (m)
δ	gas film thickness (m)
F	faraday constant (C mol^{-1})
F_b	buoyancy (N)
F_s	total surface tension (N)
g	gravity constant (m s^{-2})
I_{crit}	critical current (A)
j	current density (A m^{-2})
j_{crit}	critical current density (A m^{-2})
l	tool electrode length (m)
λ_{c1}	minimum film thickness (m)
λ_{c2}	maximum film thickness (m)
p	pressure of gas and electrolyte (Pa)
ϕ	contact angle (-)
R	radius of bubble (m)
R_d	radius of departure (m)
R_g	universal gas constant (J K^{-1} mol^{-1})

r radius in polar coordinate (m)

ρ density of electrolyte (kg m^{-3})

ρ_g density of gas (kg m^{-3})

σ surface tension (N m^{-1})

T temperature of gas (K)

t_d departure time (s)

u_r radial velocity of electrolyte (m s^{-1})

V volume of gas generated (m^3)

V_{crit} critical voltage (V)

V_d departure volume (m^3)

V_{dis} volume of dissipated gas (m^3)

z valence number (-)

4.3 The gas film

Gas film formation is one of the fundamentals of the electrochemical discharge phenomenon and is essential to EDAC. In the machining process, bubbles are generated on both electrodes through an electrolysis reaction, merge together and evolve into an insulating gas film. The formation of the gas film brings on a high electric potential gradient in the gas film leading to gas discharge. It is necessary to understand the electrochemical and dynamic properties of the gas film in order to improve the machining process.

Basak and Ghosh indicated that discharging could be modeled as a switching-circuit, in which the disruption of current flow was caused by blowing-off of bubbles (Basak & Ghosh, 1996). Jain et al. characterized electric properties of bubbles and gas film, with the consideration

of both joule heating and productive energy (Jain et al., 1999). Wüthrich and Hof derived a qualitative model for gas film thickness and demonstrated experimental approaches of decreasing film thickness by changing wettability of the tool electrode (Wüthrich & Hof, 2006). Han et al. designed a side-insulated tool to expose single bubble behavior and achieved better consistency (Han et al., 2008). However, the characteristics of the gas film still remain unclear, and it becomes a major barrier to achieving good repeatability in parts and high precision in small feature machining (Wüthrich & Hof, 2006). More controllability of the gas film can be obtained with a quantitative model of film formation and its electrochemical properties.

Gas film evolution is a complicated process. The modeling of gas film can be categorized into the following steps: bubble generation, bubble departure, and formation of the gas film.

4.3.1 Bubble development

Gas generated from the electrochemical reaction leaves the surface of the electrode in the form of bubbles on the surface of electrodes. These bubbles adhere to the electrode as their volume increases until surface tension no longer trap them. In this section, the characteristics of bubble development before departure are investigated. Assuming all bubbles around the electrode are identical (disregarding any geometric imperfections, electrical field irregularities, etc.), the case of single bubble development could represent all of the bubbles on the electrode. The parameter of particular interest is the radius of bubble-electrolyte interface, $R(t)$, as a function of time. A schematic is shown in Figure 4.1.

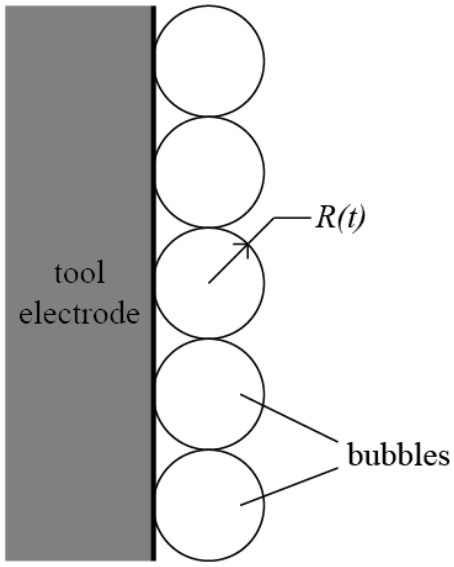

Figure 4.1. Bubble evolution on tool electrode.

It is assumed that the electrolyte is incompressible, and the viscosity of the electrolyte is negligible in the process of bubble development. By setting up a spherical coordinate system and assuming the bubbles to be spherically symmetric, the Navier-Stokes equation can be written as:

$$\rho_l\left(\frac{\partial u_r}{\partial t}+u_r\frac{\partial u_r}{\partial r}\right)=-\frac{\partial p}{\partial r} \tag{4.1}$$

$u_r(t, r)$ represents the radial velocity of any point in the electrolyte. The density of electrolyte, ρ_l, is considered as constant. The pressure of electrolyte, p, is a function of time and distance to center. The velocity field is related to the boundary of bubble through the equation of continuity,

$$\frac{1}{r^2}\frac{\partial\left(r^2u_r\right)}{\partial r}=0 \tag{4.2}$$

Assume the radius of the interface of bubble and electrolyte is *R*. Integrating the equation of continuity from *R* to any arbitrary radius *r* in the electrolyte, the radial velocity can be written as a function of *R* and the time derivative of *R*,

$$u_r = \dot{R}\left(\frac{R}{r}\right)^2 \tag{4.3}$$

With this expression, the Navier-Stokes equation can be rewritten in terms of the radius of bubbles.

$$\frac{2R\dot{R}^2 + R^2\ddot{R}}{r^2} - \frac{2\dot{R}^2R^4}{r^5} = -\frac{1}{\rho_l}\left(\frac{\partial p}{\partial r}\right) \tag{4.4}$$

Integrating Equation 4.4 from the boundary *R* to infinity and differential equation of *R* can be obtained.

$$R\ddot{R} + \frac{3}{2}\dot{R}^2 = \frac{p(R) - p_\infty}{\rho_l} \tag{4.5}$$

The pressure at the boundary interface is related to the internal pressure of bubble, p_i, and the surface tension. Therefore the final form of the bubble development equation is:

$$R\ddot{R} + \frac{3}{2}\dot{R}^2 = \frac{1}{\rho}\left(p_i - p_\infty - \frac{2\sigma}{R}\right) \tag{4.6}$$

Equation 4.6 is the differential equation of single bubble development. The solution, $R(t)$, represents the growth of bubble radius as a function of time. The constants in the equation include the density of the electrolyte, boundary and ambient pressure, and the surface tension coefficient, which are determined from chemical and mechanical properties of the electrolyte.

4.3.2 Bubble departure

As described above, bubbles are generated on the tool electrode during electrolysis. As the bubbles grow, the force balance is broken once a threshold size is reached. Bubbles sustain the following forces on the surface of tool electrode: buoyancy, surface tension, and the inertia forces due to liquid motion when bubble expands (Figure 4.2) (Chang, 1957).

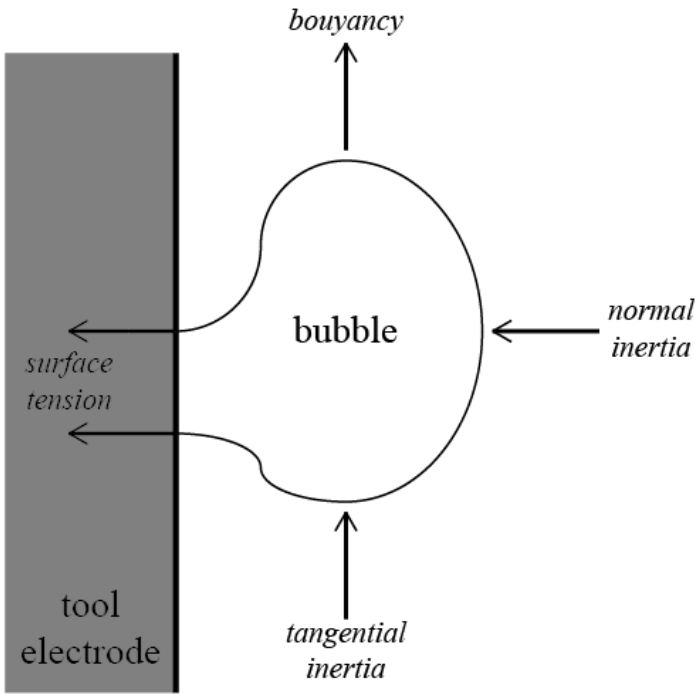

Figure 4.2. Equilibrium of a single bubble on tool electrode

A simplified model only accounts for buoyancy and surface tension by assuming the inertia forces of the ambient liquid are small and negligible. The buoyancy force and the surface tension are the most significant forces in the balance, derived by

$$F_b = C_b g R^3 \left(\rho_l - \rho_g\right) \tag{4.7}$$

$$F_s = C_s \sigma R \tag{4.8}$$

where C_b and C_s are constant coefficients, ρ_g is the density of hydrogen gas. The balance of buoyancy and surface tension give an estimation of a static departure size of bubble, given by

$$R_d = C\left[\frac{\sigma}{g(\rho_l - \rho_g)}\right]^{1/2} \tag{4.9}$$

Several empirical studies have been conducted to determine the coefficient in the equation of bubble departure size. Fritz determined the coefficient from experiments on hydrogen and water vapor and considered the contact angle, ϕ, between bubble and the solid surface (Fritz, 1935):

$$R_d = 0.0148\frac{\phi}{2}\left[\frac{2\sigma}{g(\rho_l - \rho_g)}\right]^{1/2} \tag{4.10}$$

Cole and Shulman concluded a model considering various fluids, and appended a refinement term to the model (Cole & Shulman, 1967):

$$R_d = 0.0148\frac{\phi}{2}\left[\frac{\sigma}{g(\rho_l - \rho_g)}\right]^{1/2}\left[1 + 0.005\left(\frac{dR}{dt}\right)^{3/2}\right] \tag{4.11}$$

4.3.3 Gas film formation

To investigate the formation and evolution of the gas film, it is necessary to take a look at Taylor instability. If two fluids of different density share a common interface and are accelerated in a direction perpendicular to the boundary, the interface will be affected by perturbations. If the acceleration is from the lighter to denser fluid, the perturbation will tend to decay over time. On the contrary, if the acceleration is in reverse direction, the interface will become unstable and will no longer be a plane. Such instability is often exhibited by liquid-gas interaction in real life.

A good example is a small tube with one end blocked and filled with water. Water will remain in the tube even if it is turned upside down as long as the tube is thin enough. On the other hand, water falls down in such a turbulent way that water splits into drops if the inner radius of the tube is larger than the critical value of stability.

This stability phenomenon is called “Taylor instability”, and is mathematically modeled and experimentally verified. Assuming small perturbation, the interface is modeled to have wave motion. The interface is guaranteed to be stable if the wavelength of motion is larger than a critical value, λ_{c1} (Zuber, 1959):

$$\lambda_{c1} = 2\pi\left[\frac{\sigma}{g(\rho_l - \rho_g)}\right]^{1/2} \tag{4.12}$$

However, this criterion is weak in judging the stability of thin gas film on gas-liquid surface. A stronger version of this criterion makes use of a longer characteristic wavelength of second mode, λ_{c2} (Basak & Ghosh, 1996):

$$\lambda_{c2} = 2\pi\left[\frac{3\sigma}{g(\rho_l - \rho_g)}\right]^{1/2} \tag{4.13}$$

The gas film is considered stable and lasting if the intrinsic wavelength is larger than λ_{c1} but smaller than λ_{c2}. In the process of gas film formation, the actual perturbation wavelength, λ, can be estimated by the average distance of nucleation sites, and can be estimated from the thickness of the gas film. The gas-liquid interface is considered stable if the thickness falls in the range between λ_{c1} and λ_{c2}. In other words, the gas film is lasting and suitable for discharging activities if and only if these criteria are satisfied.

4.3.4 Gas film in electrolysis

Gas film is critical in electrolysis and discharging because it creates a gap of insulation between tool electrode and electrolyte. High electric potential is not established near the tool electrode if it is not fully detached from electrolyte, which is similar to a "short circuit" in EDM processes. Therefore, it is essential to study the electrochemical properties of the gas film in electrolysis.

The dynamics of bubble and the gas film from the aspect of fluid dynamics are discussed in previous sections. The following properties are investigated: Bubble radius as a function of time, bubble radius at departure, and critical thicknesses of the gas film. In this section, modeling of gas film formation in electrolysis is presented.

To correlate these properties to electrolysis, the rate of gas generation should be considered. The total volume of gas generated can therefore be derived by assuming all bubbles around the tool electrode have similar properties. Gas generation can be estimated from current flow in electrolysis because the formation of every hydrogen molecule absorbs two electrons, which resembles the statement of Faraday's first law of electrolysis. For gas generation, this relation can be expressed as:

$$\dot{V}(t) = \frac{j(t)A}{zF} \cdot \frac{R_g T}{p} \tag{4.14}$$

where V is the total volume of gas generated in electrolysis; F is the Faraday constant; z is the valency number of altered substance; j is the transferred current density; A is the total surface area of electrode; R_g is the gas constant; T and p are temperature and pressure of gas, respectively. Since the environment is surrounded by boiling sodium hydroxide electrolyte, heat transfer

between the heated gas and the electrolyte cools down the gas to the boiling point of the electrolyte due to the large ratio in total heat capacity.

The current density in the electrolysis is related to the kinetics of electrochemical reaction, and can be determined either by experimental measurement or from empirical relations, such as the Butler-Volmer relation (Wüthrich & Hof, 2006).

It can be observed that bubble dissipation is negligible in the time before the merging of bubbles. This is because small bubbles will attach to the electrode until departure size has been reached. Therefore it is reasonable to assume that the volume of gas adhered to the electrode is equal to the total volume of generated gas from electrolysis. A corollary of such an assumption is that the total volume of adhered bubbles right before bubbles begin to leave the electrode follows the equation:

$$V_d = \int_0^{t_d} \dot{V}(t)dt \tag{4.15}$$

where t_d is the time at departure, solved by

$$R(t_d) = R_d \tag{4.16}$$

Assuming bubbles distribute uniformly over the electrode, the average thickness of the bubble covered regime, δ, can be deduced by dividing V_d by the surface area of the electrode. If the dissipation of bubbles occurs at a constant rate, the thickness of gas film can be derived from:

$$\delta = \frac{V_d}{A} = \int_0^{t_d} \left(\frac{j(t)}{zF} \cdot \frac{RT}{p} + \dot{V}_{dis} \right) dt \tag{4.17}$$

A simplified form of Equation 4.17 can be obtained if current density in the process is constant (Equation 4.18). That thickness of the gas film turns out to be linearly correlated with current density, with an offset due to dissipation.

$$\delta = \frac{RTt_d}{zFp} j + \dot{V}_{dis} t_d \tag{4.18}$$

Considering the stability of gas film, it is determined that the gas film is stable if $\lambda_{c1} < \delta < \lambda_{c2}$. In the case of a large gas film thickness for which Taylor stability is not satisfied, surface stability cannot be guaranteed. In real electrolysis process, however, bubble development and departure do not observe the listed hydrodynamic properties because interaction among bubbles will dramatically change the characteristics of bubble development. In experimental investigations, there is not an upper limit of gas generation rate for a stable gas film generation.

4.4 Experimental investigation of gas film

Experimental investigation is used to reveal the gas film evolution process. An apparatus for ECDM is developed (Figure 4.3). A cylindrical tool with 0.5 mm diameter, as is widely used in conventional ECDM, is immersed into 30 wt.% NaOH electrolyte by 2 mm.

4.4.1 Qualitative analysis

A DC electrode voltage of 34 V, which is higher than the critical voltage to initiate the electrochemical discharge phenomenon, is applied to the electrodes. The process of gas film evolution is recorded using a high speed camera at 10k fps. Before the power is turned on, the tool electrode is clean and the electrolyte is stable [Figure 4.4(a)]. Once the DC power is turned on, bubbles start to form on the tool electrode [Figure 4.4(b)]. Almost all the bubbles are

attached to the surface of electrode at this point (bubble departure could not be observed). After 2 ms, bubbles cover the entire electrode surface as more bubbles are generated and begin to merge [Figure 4.4(c)]. All the bubbles eventually evolve into a single bubble surrounding the electrode, giving birth to insulation and interrupting electrolysis [Figure 4.4(d)]. The large bubble then begins to shrink afterwards because no more bubbles are generated once tool electrode is insulated. The bubble eventually reaches a size appropriate for discharging and becomes a stable gas film supporting the electrochemical discharge phenomenon. It is experimentally determined that the discharging delay is approximately 10ms, consistent with the high speed camera imaging results.

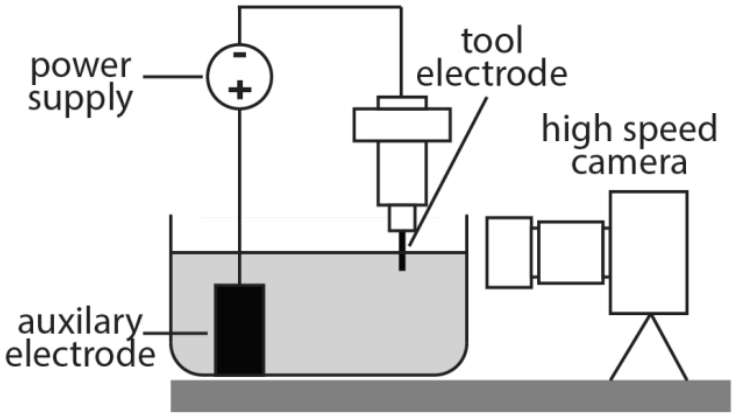

Figure 4.3. Experimental apparatus for ECDM.

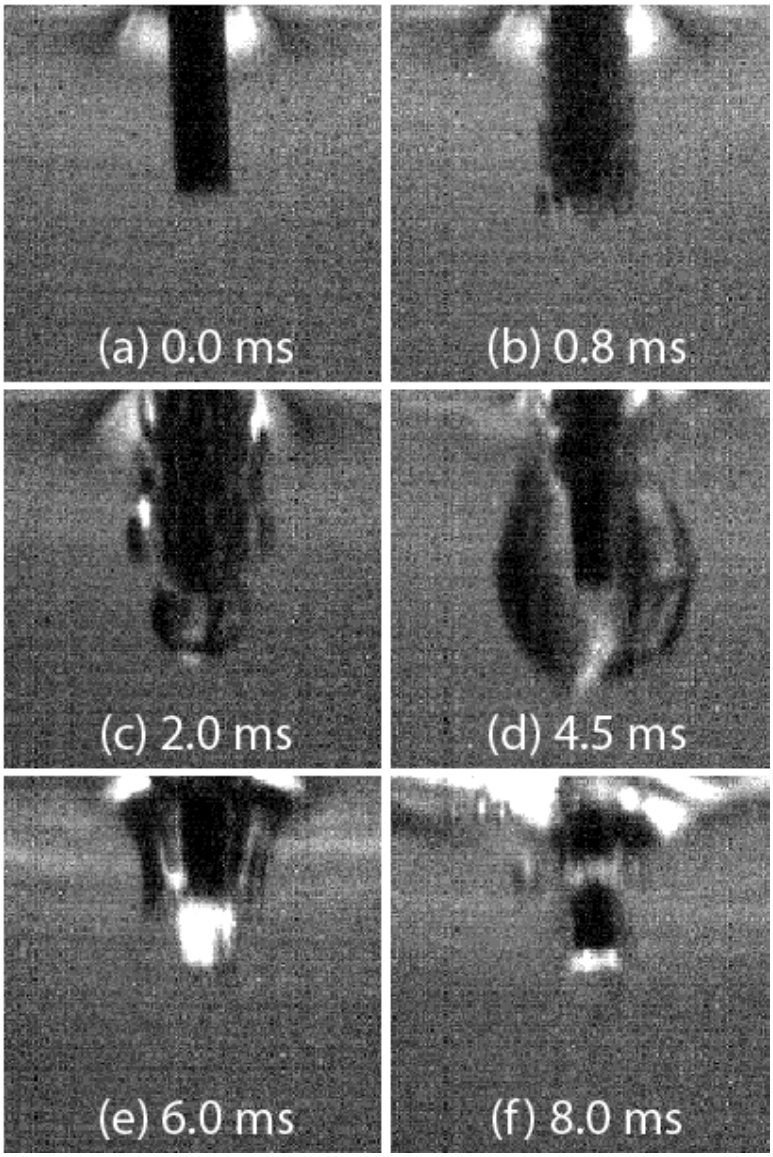

Figure 4.4. High speed camera images of electrochemical reaction in discharging regime

In the case of a lower electrode voltage (30 V), under which electrochemical discharge phenomena do not take place, bubble evolution follows a different pattern. The initial stages of bubble generation are similar to those under high electrode voltage [Figure4.5(a), 4.5(b)]. However, the bubbles surrounding the tool electrode fail to merge into a single layer even if the electrode is fully covered. It can be implied that full area coverage is not a sufficient condition of gas film formation. Other requirements, such as stability criterion must be satisfied.

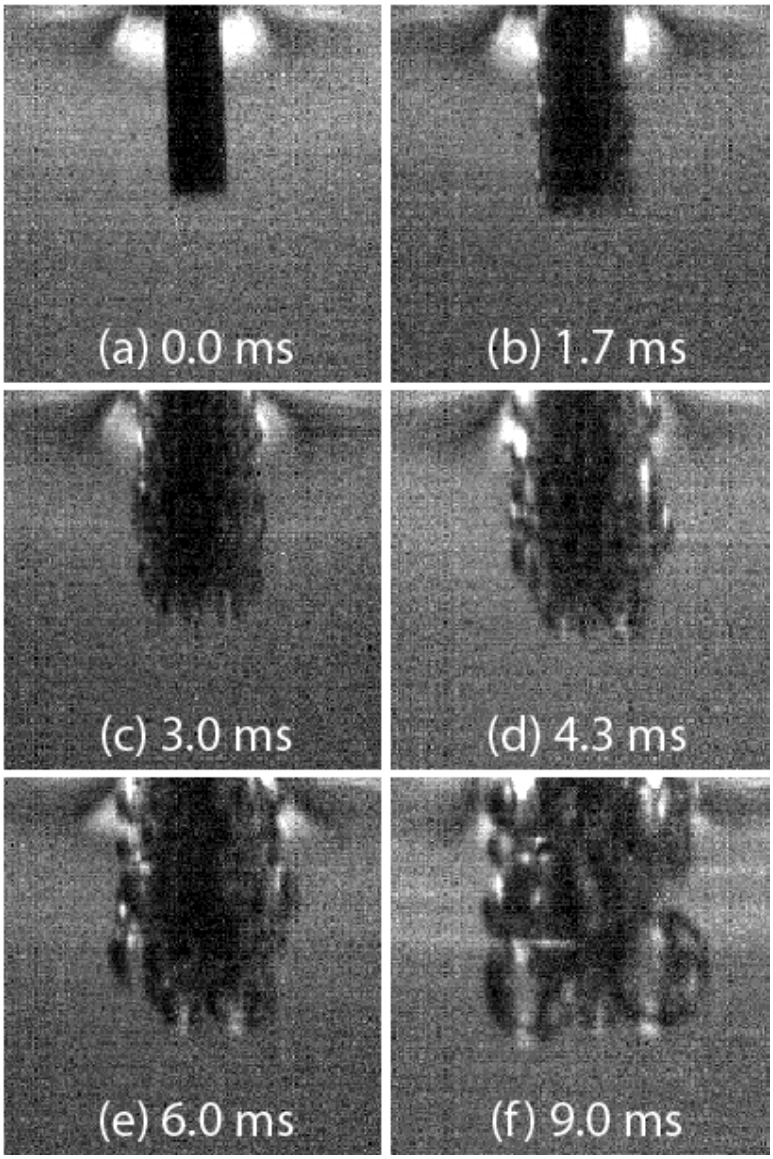

Figure 4.5. High speed camera images of electrochemical reaction with low electrode voltage

4.4.2 Thickness of gas film

Equations 4.12 and 4.13 describe a theoretical estimation of the thickness of the gas film on the tool electrode. Gas film thickness is linearly correlated with the square root of surface tension and the density of electrolyte. Sodium hydroxide can significantly increase surface tension and electrolyte density at different concentrations. Properties for sodium hydroxide

solutions are listed in Table 4.1. The range of stable gas film thicknesses are also calculated and shown.

Table 4.1. Properties of NaOH solution and calculated film thickness.

(density data from Lide et al., 2004; surface tension data from Abramzon and Gaukhberb, 1993)

NaOH (wt. %)	Density (kg/m^3)	Surface tension (dyn/cm)	λ_{c1} (μm)	λ_{c2} (μm)
10	1.109×10^3	76.03	16.62	28.78
20	1.219×10^3	85.47	16.80	29.01
30	1.328×10^3	96.13	17.07	29.57

It can be seen that although surface tension and the density of sodium hydroxide solution change dramatically at different concentrations, gas film thicknesses are not significantly affected. A picture of discharging in 30 wt. % NaOH electrolyte is used to compare the theoretical estimation to experiments (Figure 4.6). The overall diameter of the electrode and the gas film increases from 500 μm to 548 μm, indicating the thickness of the gas film is 24±5 μm, which falls in the range of theoretical estimations.

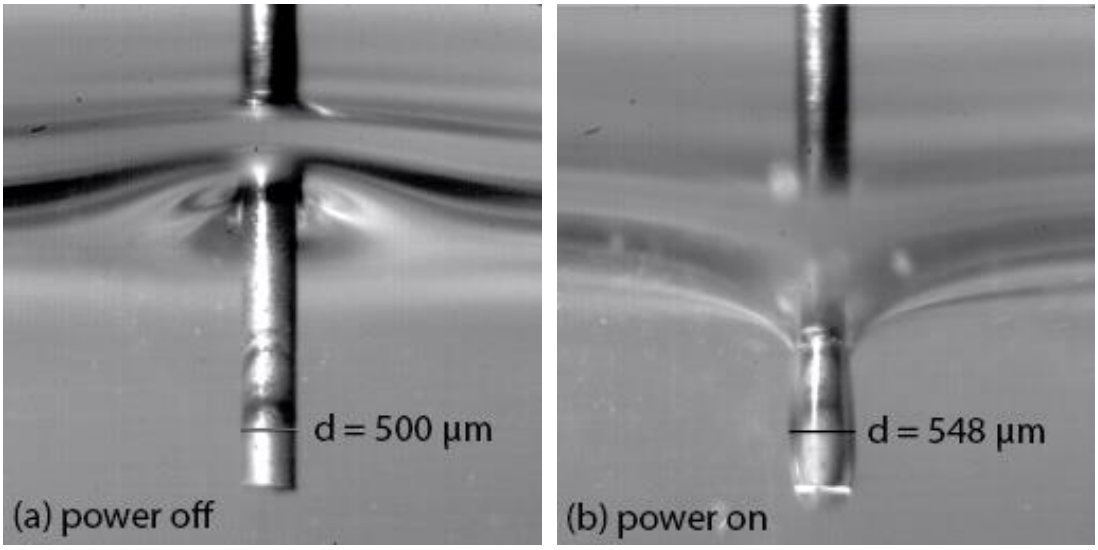

Figure 4.6. Experimental evaluation of gas film thickness.

4.4.3 Critical voltage and current

The critical voltage to trigger the discharge phenomenon is also an important factor to consider. If the critical voltage in a specific machining environment is too high, machining quality can be highly affected due to high energy of the discharge. To quantitatively determine critical voltage, a set of commonly used ECDM parameters are chosen for testing critical voltage, including the concentration of electrolyte, and the diameter and immersion of tool electrode, as shown in Table 4.2.

A full factorial experiment is completed to determine critical voltage and current. Critical voltage is generally considered to be the most important characteristic of discharging. However, volume of gas generated is proportional to current density rather than voltage on electrodes (Equation 4.14). Electrical voltage and current are recorded three repeated experiments, with the current density derived from total current and area of immersion (Table 4.3).

Table 4.2. Parameters for critical voltage test.

NaOH concentration *c* (wt. %)	10, 20, 30
Tool diameter *d* (mm)	0.5, 1.0
Tool immersion *l* (mm)	1.0, 1.5, 2.0

The critical thickness of stable gas film can be derived from Equations 4.12 and 4.13. The results are compared to the average current density of all experimental results under same concentration (Figure 4.7). From the results, it can be concluded that current density in experiments are linearly related to theoretical values of film thickness, which is consistent to the relation presented in Equation 18.

Critical current in the ECDM process can therefore be predicted using the model. The critical current with typical ECDM process parameters are listed in Table 4.4.

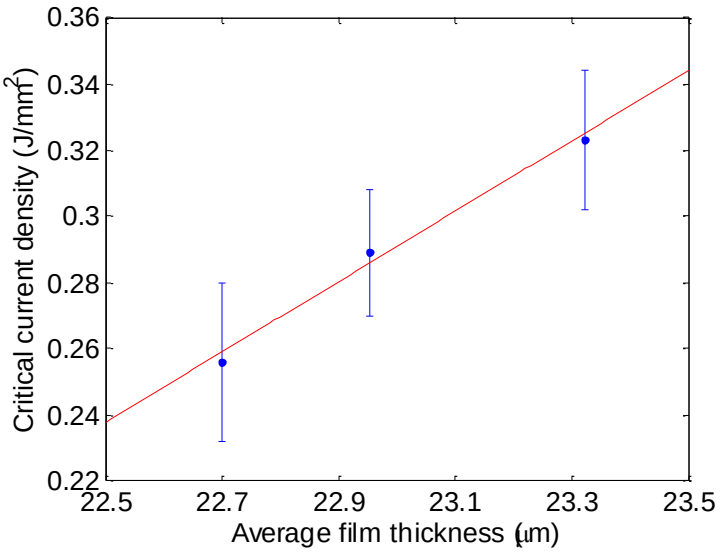

Figure 4.7. Critical current density against average gas film thickness.

Table 4.3. Critical voltage and current density of electrical discharging.

c (%)	d (mm)	l (mm)	V_{crit} (V)	j_{crit} (A/mm^2)
10	0.5	1.0	31.4±0.3	0.358±0.007
10	0.5	1.5	33.9±0.2	0.278±0.002
10	0.5	2.0	36.5±0.6	0.260±0.006
10	1.0	1.0	31.5±0.3	0.190±0.002
10	1.0	1.5	40.8±0.5	0.230±0.005
10	1.0	2.0	44.6±0.5	0.219±0.003
20	0.5	1.0	27.3±0.5	0.369±0.002
20	0.5	1.5	30.5±0.4	0.289±0.002
20	0.5	2.0	32.9±0.2	0.282±0.003
20	1.0	1.0	33.5±0.2	0.301±0.008
20	1.0	1.5	36.9±0.4	0.251±0.005
20	1.0	2.0	42.5±0.6	0.239±0.006
30	0.5	1.0	26.7±0.3	0.341±0.005
30	0.5	1.5	33.6±0.5	0.320±0.005
30	0.5	2.0	38.6±0.6	0.315±0.009
30	1.0	1.0	38.4±0.9	0.397±0.011
30	1.0	1.5	41.3±0.2	0.307±0.001
30	1.0	2.0	41.1±0.5	0.256±0.011

Table 4.4. Critical current with common tool and electrolyte in ECDM.

c **(wt. %)**	**d (mm)**	***l*** **(mm)**	I_{crit} **(A)**
10	0.5	1	0.47
10	0.5	2	0.89
10	1.0	1	1.04
10	1.0	2	1.88
20	0.5	1	0.52
20	0.5	2	0.98
20	1.0	1	1.15
20	1.0	2	2.07
30	0.5	1	0.59
30	0.5	2	1.11
30	1.0	1	1.30
30	1.0	2	2.35
40	0.5	1	0.67
40	0.5	2	1.26
40	1.0	1	1.49
40	1.0	2	2.68

4.5 Energy of discharging

Energy release through discharging activity is crucial to process modeling since it determines the gross thermal input to the material. Experimental calibration of discharging energy, however, is often indirect and inaccurate. There are various reasons that result in such difficulty. First, the discharging and material removal process is very sensitive and vulnerable to changes in ambient conditions, which causes low repeatability in experiments. Second, real-time

observation is not feasible for micro-scale machining, especially in high temperature alkali solution. Sensors installed in the machining area could interfere with the original setup and thus change the electrochemical and fluid dynamic characteristics of the process.

In this section, process modeling for spark generation is presented. Spark energy is experimentally determined and fit into a stochastic model. A sharp tool electrode is fabricated and employed in the experiments to increase the consistency of spark generation. A finite element model is developed to correlate spark energy to material removal. Experiments are conducted to validate the models.

4.5.1 Sharp tool electrode

The conventional rod is not an ideal object for investigation due to the "fringing effect": the release of sparks is distributed around the rim. Replacing the cylindrical tool with a sharp tool, however, could make discharges focus on a concentrated region.

A finite element simulation is deployed to investigate electrochemical reactions in the machining process. The tool electrode is chosen to be tungsten with 250 μm diameter and the electrolyte is 30 wt. % NaOH. Electrode voltage is set to 30 V. The simulation proves that fringing effects exist for cylindrical tools, while conic tools have only one spot for spark generation. Figure 4.8 shows the current density around the tool electrode (brighter color represents higher current density). It can be seen that current density is more intense near the rim for cylindrical tools. Thus, sparks tend to generate from any point along the rim of the tool electrode, if not considering any geometrical defects. However, sparks can only be generated at the tip of tapered tools, and thus increase consistency in spark generation.

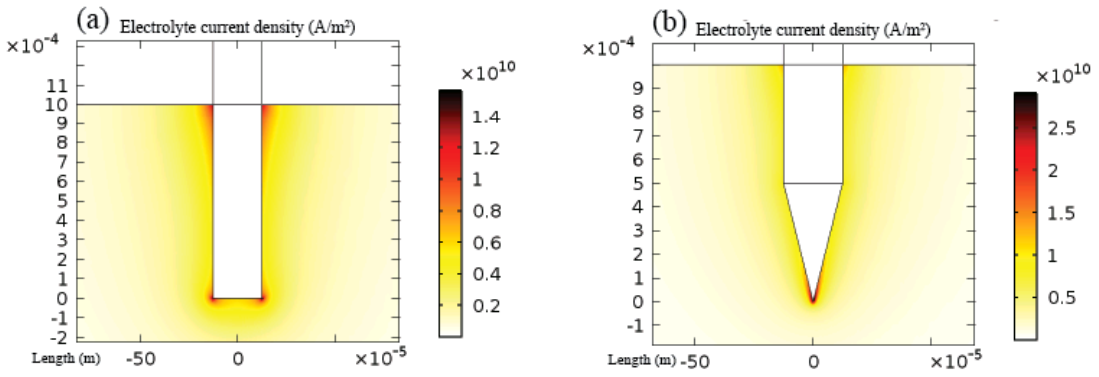

Figure 4.8. Finite element simulation of current density in electrochemical reaction.

(a) cylindrical electrode. (b) sharp electrode.

Electrochemical machining (ECM) is used to fabricate tools with tapered end (Figure 4.9). Sharp tools are made from tungsten rods with 250 µm diameter. The rods are cut to approximately one inch long and clamped on the chuck. Tool and chuck are connected to the power supply as the anode in the ECM process. The auxiliary electrode is made of stainless steel. A hole is drilled in the center of auxiliary electrode, surrounding the tool electrode to create an axisymmetric electrical field in the electrochemical reaction. The auxiliary electrode is immersed 1 mm under the upper surface of the electrolyte (8 wt. % NaOH).

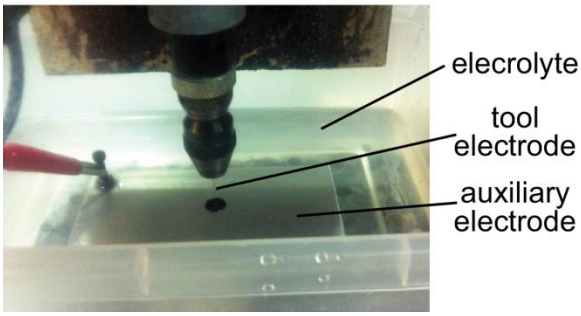

Figure 4.9. Tool electrode fabrication by ECM

By adjusting electrode voltage and the vertical position of the tool in the ECM process, tool electrodes with different geometries can be fabricated (Figure 4.10). Chiou et al. (2012) empirically modeled the ECM process for high-aspect micro-rods to correlate machined geometry, including rod width and shape, with machining times ranging from 0 to 80 min. Mochimaru et al. (2012) studied ECM of micro-tool electrodes by investigating micro-flow from variation of tool geometry in experiments. Tool electrodes, made of tungsten, act as anodes in electrochemical reaction. The tool electrode dissolves faster at the rim of the auxiliary electrode (cathode) because of higher electrical field intensity. Tools with different shapes can be fabricated by changing the relative position to the cathode. As a result, tool electrodes fabricated can either have long tapered tips with high aspect ratio, or have short tapered ends with high stiffness. Some other geometries (such as two-section tools) can also be achieved by choosing process parameters appropriately.

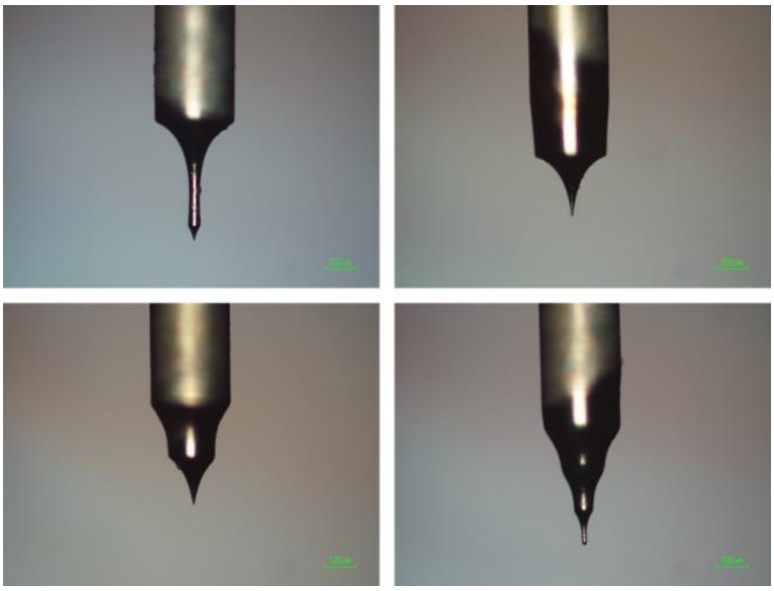

Figure 4.10. Conic tool electrodes with different shape.

4.5.2 Experimental measurement of spark energy

The energy of sparks can be explicitly calculated using the integral of the product of current and voltage. The current waveform (Figure 4.11) indicates the duration of single sparks is around 0.1 to 0.2 ms. The current sensor employed has a measuring bandwidth of 200 kHz, resulting in a resolution of 5 μs, and therefore preventing aliasing in sensing

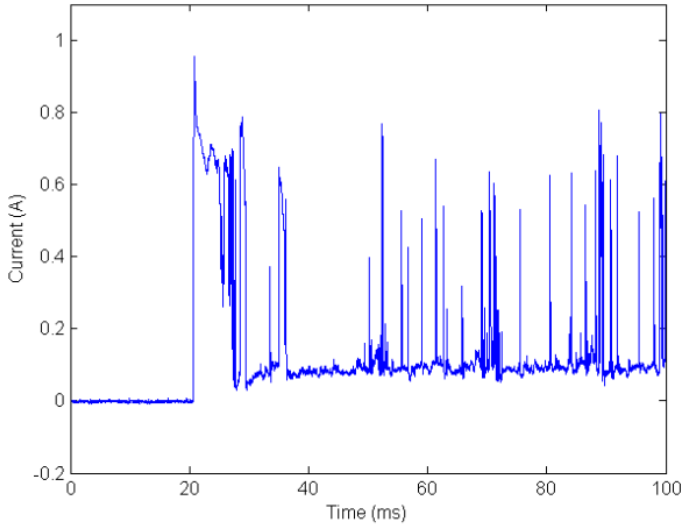

Figure 4.11. Current output of DC power supply in discharging regime.

Electrode voltage is 35 V.

Note that current output peaks at 1 A and is maintained at a high level for approximately 15 ms after power is turned on, indicating that the gas film has not fully developed and the electrochemical reactions are not in discharging regime. In this case, even if the electrode voltage is set to be higher than the critical voltage for discharging, sparks are not generated instantly due to the instability of gas film in the transient phase. In the experiments, the minimum pulse width of the power supply (if using pulse output) is set higher than 30 ms to ensure a safety factor of 2.

However, uncertainties are involved in discharging activity during ECDM due to high instability of the gas film. Duration and peak current vary among discharges, and therefore change the energy releasing rate. A histogram (Figure 4.12(a)) shows the distribution of energy released by sparks with a tapered tool electrode (energy is labeled in logarithm scale). As a benchmark, energy histogram of sparks generated by a cylindrical tool is also presented in Figure 4.12(b). Figure 4.12 illustrates that the energy of sparks generated by tapered tool electrode distributes around one value, while the distribution peaks twice in the case of using cylindrical tool electrode.

Figure 4.12 suggests that the energy of sparks follows 2-component mixture log-normal distribution with form shown in Equation 4.19:

$$P(\log q) = p_1 \frac{1}{\sigma_1\sqrt{2\pi}} \exp\left(-\frac{(\log q - \mu_1)^2}{2\sigma_1^{\,2}}\right) + p_2 \frac{1}{\sigma_2\sqrt{2\pi}} \exp\left(-\frac{(\log q - \mu_2)^2}{2\sigma_2^{\,2}}\right) \tag{4.19}$$

where q is the energy of single spark, while the function P (log q) gives an estimation of the probability of spark generation given certain energy. p_1, p_2, μ_1, μ_2, σ_1, σ_2 are parameters of fitting, as shown in Table 4.5. p_1, p_2 are weights of log-normal distributions, μ_1, μ_2, σ_1, σ_2 are the average and the standard deviation, respectively.

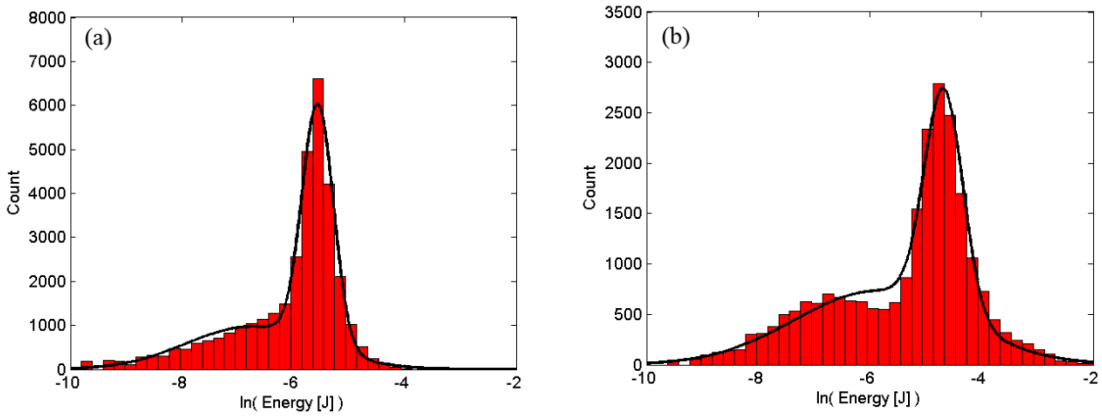

Figure 4.12. Energy distribution of sparks (a) sharp tool electrode. (b) cylindrical tool electrode

Table 4.5. Fitting parameters of energy distribution of single spark

	Tapered	Flat
p_1	0.57	0.41
p_2	0.42	0.58
μ_1	-5.56	-4.67
μ_2	-6.74	-5.86
σ_1	0.28	0.34
σ_2	1.16	1.48

Figure 4.12 illustrates that sharp tools create more consistent sparks comparing with flat-end tools. To be specific, the proportion of sparks with low energy is larger when using flat-end tools (reflected by fitting parameters in Table 4.5), indicating two possible discharging releasing mechanisms. For a cylindrical tool electrode, sparks tend to release from the edge because of the higher electrical field intensity. Meanwhile, minor discharges take place at the flat section of the tool, corresponding to the minor peak in the distribution. The tapered tool electrodes, however, eliminate the minor discharging effect, resulting in uniform sparks.

Considering the single spark energy releasing model, the spark energy follows a log-normal distribution if not accounting for sparks with very low energy. Considering the fact that sparks with energy lower than 30% do not remove material from the workpiece, it is reasonable to neglect them. Specifically, the mean spark energy is exp ($-\mu_1$), i.e. 3.8mJ.

4.6 Conclusions

Gas film formation is a critical element in EDAC that is closely related to productivity, accuracy, and repeatability of machining. Controlling film thickness is essential to preserve the quality of machining, and therefore setting up a model for gas film evolution is necessary. This chapter presents modeling and experimental investigation of gas film in EDAC to characterize film thickness and transient behavior. A physics-based model is derived for gas film dynamics and electrolysis to correlate film characteristics with various process parameters. Meanwhile, the mechanisms of the discharging phenomena are revealed through modeling and experimentation, including the process of bubble growth and the criterion of the transition from bubbles to gas film. The specific findings are:

- A necessary condition of triggering discharging activity is the existence and integrity of the gas film. The mechanism and interaction between discharging and the gas film has long been a controversial topic. In this research, sets of high speed camera images are innovatively utilized to demonstrate the film evolution process. These images clearly indicate that the presence of gas film is required for sparks to take place.

- Gas film behavior is not only influenced by electric power input, but is also closely related to physical properties of the electrolyte. The surface tension and density of the electrolyte can significantly affect bubble development and film evolution, as is indicated from the model of film evolution. It is also determined from the model that film thickness is typically in the range of 17 to 29 μm. In addition, thinner gas film is desirable because critical voltage and current can be lowered and therefore suppress overcutting in machining. This can be achieved by reducing surface tension or increasing density of the

electrolyte. In this case adding surfactant to the electrolyte is a practical approach of reducing surface tension.

- Current density near the tool electrode is a more generic parameter to initiate sparks from the aspect of electrochemistry. The model of electrolysis indicates that the reaction rate of generating bubbles and films is proportional to current density. Reducing the tool size and the depth of immersion can amplify current density without changing power supply to the electrolysis.

- Fabricated by ECM, conic tool electrodes can enhance consistency in spark generation comparing with conventional tools. The energy level of each spark generated is measured and is fit in a stochastic model with a two-component mixture log-normal distribution. The energy distribution proves that conic tool improves the consistency of spark generation and suppressed the generation of minor discharges. The average energy for sparks is 3.8 mJ with 34 V electrode voltage.

Chapter 5

Process Modeling of the Electrochemical Discharge Assisted Cutting

5.1 Introduction

The EDAC is a process that removes material using electrochemical discharge and mechanical cutting. The process cannot be improved and optimized without proper understanding of the material removal mechanism. However this process is complicated due to the hybrid physics involved. The major challenges come from the following aspects:

(1) Mechanical behavior of amorphous materials at high temperature. As electrochemical discharge brings heat to the workpiece, temperature rises dramatically inside the workpiece and changes the mechanical properties significantly. The status of material is not only a combination of two or three states, like most metals or crystal materials, but changes continuously over material temperature. The material can be rather viscous, and the viscosity is highly temperature dependent.

(2) Temperature profile in the material. The discharge at the gas film occurs near the cutting edge of the tool. The way that the workpiece material is heated is related to many process parameters, including the electrode voltage, feed rate, and depth of cut. It is

essential to determine the temperature profile so that it can be made possible to further determine the mechanical behavior of the material.

(3) Cutting force and other mechanical concerns. Cutting force is involved wherever mechanical contact takes place. Many aspects of machining are related to cutting force including surface finish and tool wear. The conventional cutting force model is not applicable to the EDAC due to different material removal mechanisms.

This chapter covers all of the aspects listed above and eventually leads to a material removal model with the EDAC. The results are validated by comparing simulation results with experiments under the same process parameters.

5.2 Mechanical behavior of amorphous material under high temperature

In conventional EDM processes, a typical material removal scenario is that the material closest to the tool is molten and gets pushed out with high heat induced pressure in dielectric flow. Meanwhile the material that is further away forms a recast layer. The classic EDM material removal theory does not apply to the EDAC for one critical reason: the status of metal is "binary", in other words evaluating the proportion of molten material is key to model material removal in EDM.

Amorphous materials are not "binary". Take silicate glass as an example. The nominal melting point of glass is around 1700 K, where glass forms a tacky liquid and silicon-oxygen bonds are broken (Brown et al., 2000). If the heating continues, the experiment curtails after a while (Ellis, 1998). But before reaching the melting point, glass is softened and acts like a very

viscous fluid. The correlation between viscosity and temperature can be found in the following figure.

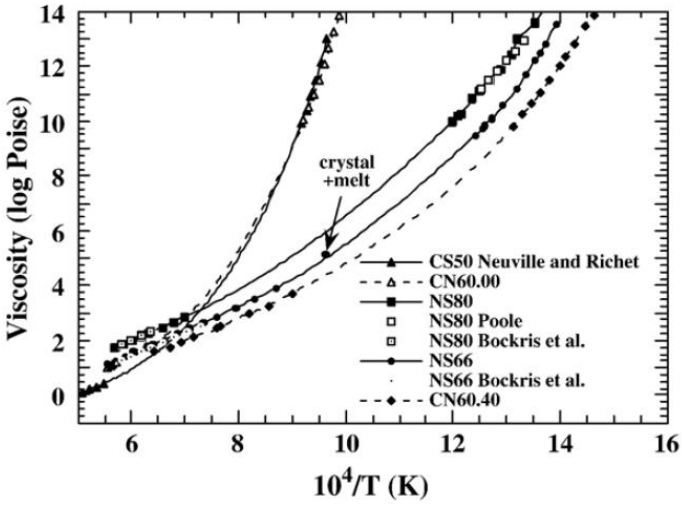

Figure 5.1. Viscosity of glass. CN60.40 represents a SiO2-Na2O-CaO system.

(Neuville, 2006)

It can be seen from the figure that the viscosity of soda-lime glass at the boiling point is about 1 Poise, or 0.1 Pa·s, about 10 times higher than the viscosity of water. The viscosity starts to decrease once the temperature reaches 680 K, where the viscosity is reported to be 10^{13} Pa·s. With such a high viscosity, the material is still too hard to be effectively cut via mechanical approach.

There must be a certain point that the material is softened enough that mechanical cutting becomes effective. It has been found that if the mechanical load is less than 23 MPa, parameters including depth of cut and feed rate become insensitive and glass can always be cut in ductile mode (Arif et al., 2011). The corresponding viscosity to prevent brittle cutting is 4×10^9 Pa·s. And the equivalent transition point is 800 K respectively.

5.3 Temperature profile in the material

As can be concluded from the discussion above, the mechanical properties of an amorphous material are highly temperature dependent. Therefore it is essential to obtain a temperature profile of the material. To solve this problem, there are two major challenges: heat input from the tool and heat transfer inside the material.

5.3.1 Heat input from electrochemical discharging

The electrochemical discharges serve as a strong source that heats up the material. Total heat input to the material equals the product of electric power and the heat absorption ratio. Total electric power consumption can be tracked by voltage and current sensors. Many researchers have empirically determined the average absorption heat ratio in EDM or ECDM processes (Kunieda et al., 2005; Wei et al., 2011).

However, the spatial distribution of such heat input remains unclear. A common way to deal with this issue in EDM is to use Gaussian distribution around the center axis for cylindrical electrodes. However this is not applicable to the EDAC process because:

- Helical tools are very different from cylindrical tools. Applying Gaussian distributions eliminates all details about the tool geometry and only gives an averaged estimate.
- By taking the picture of discharging (Figure 3.4), sparks are very intense at the cutting edges and sharp corners. Gaussian distributions around the center axis do not characterize this feature very well.

A good way to understand the discharging is to look at the physics. Gas discharge is the result of electron drifting. Although electrons move randomly at high speed, electrons can move

systematically in the presence of some external factors, for example an electric field. The drift velocity, v_d, is proportional to the electric field intensity by the scale μ_e, the mobility of electrons. μ_e is proportional to the gas pressure, p, as well (Raizer and Allen, 1997).

$$v_d = \mu_e E \tag{5.1}$$

$$\mu_e = \nu_e p \tag{5.2}$$

The mobility of electrons is a constant physical property of gas. Hydrogen is the discharging gas in cathode tool in the EDAC. The coefficient of electron mobility, ν_e, is constant for hydrogen gas: 37 m^2 Torr V^{-1} s^{-1}. Pressure inside the hydrogen gas film is assumed to be constant in the machining process because the film exhibits stable fluid dynamic behavior.

The current density in gas discharge is proportional to the drift velocity, scaled by the product of unit electron charge e and density of electrons n_e.

$$j = en_e v_d \tag{5.3}$$

Heat is released in gas discharge as current flows through the gas. Similar to joule heating in circuit, where the heat generation is the product of voltage and current, the amount of heat Q in gas discharge is the product of electric field E and current density j.

$$Q = jE \tag{5.4}$$

Substituting the current density equation into Joule heat equation, it can be indicated that the heat generation in gas discharge in proportional to the square of electric field.

$$Q = en_e \mu_e E^2 \tag{5.5}$$

Therefore heat release in electrochemical discharging can be calculated once the electrical field intensity is determined. Solid electrodes have much lower electric resistance than the electrolyte, and therefore can be assumed to have the uniform electric potential. The electrochemical governing equation of the electrolyte is (Nann & Heinze, 1999):

$$\frac{\partial c_e}{\partial t} = \nabla \cdot \left(D_e \nabla c_e\right) - \nabla \cdot \left(\frac{t_+}{z_+ F}\,\mathbf{j}_e\right) + \nabla \cdot \left(\frac{D_e c_e k_{T,e}}{T}\nabla T\right) \tag{5.6}$$

with the boundary conditions at the electrode surface

$$\begin{aligned} \mathbf{j_s} \cdot \mathbf{n_s} &= i_{se} \\ \mathbf{N}_{+,s} \cdot \mathbf{n}_s &= \frac{i_{se}}{z_+ F} \end{aligned} \tag{5.7}$$

where c_e is the concentration of the ions, D_e is the interdiffusion coefficient, t_+ is the transference number of ions, z_+ is the charge of ions, $k_{T,e}$ is the Soret coefficient, T is the temperature, $\mathbf{j}$ is the electrical current, $\mathbf{N}_+$ is the ionic flus, ns is the normal vector of the boundary, i_{se} is the current density across the surface.

The electric field distribution can be simulated by the finite element method (FEM). The FEM simulation is deployed in Comsol Multiphysics software using the electrochemistry module. As an example, Figure 6 demonstrates the distribution of electric field, as a function of distance from the center. It can be found that fringing effects are quite severe: the electric field is four times stronger at the rim than at the center. That corresponds to 16 times of energy at the rim comparing with those at the center.

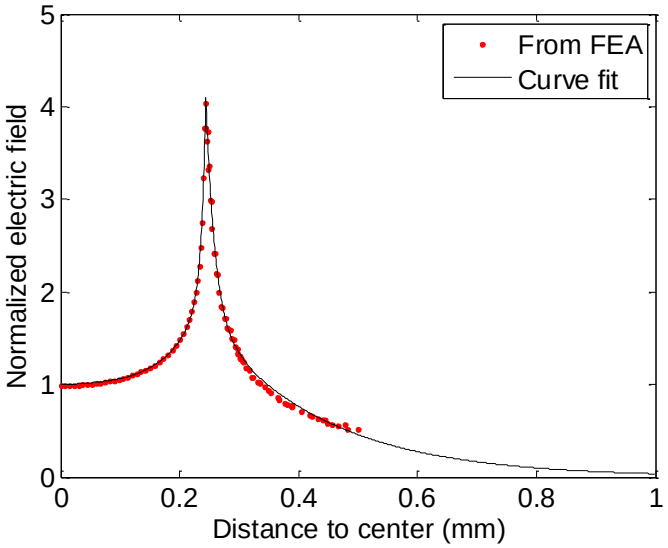

Figure 5.2. Electric field intensity distribution of a 0.5 mm diameter cylindrical tool.

The fringing effect from the simulation is consistent with observations (Figure 5.3). The simulated electric field intensity is much higher at the tips and edges, while sparks can only be found on the edges in experiments. Since discharging is far more intense at the cutting edges, they are treated as line heat sources in the heat transfer simulations. The simulated electric field intensity along the cutting edge is shown in Figure 5.4. The computational error is relatively large because the electric field is the derivative of the voltage field and therefore the error is magnified.

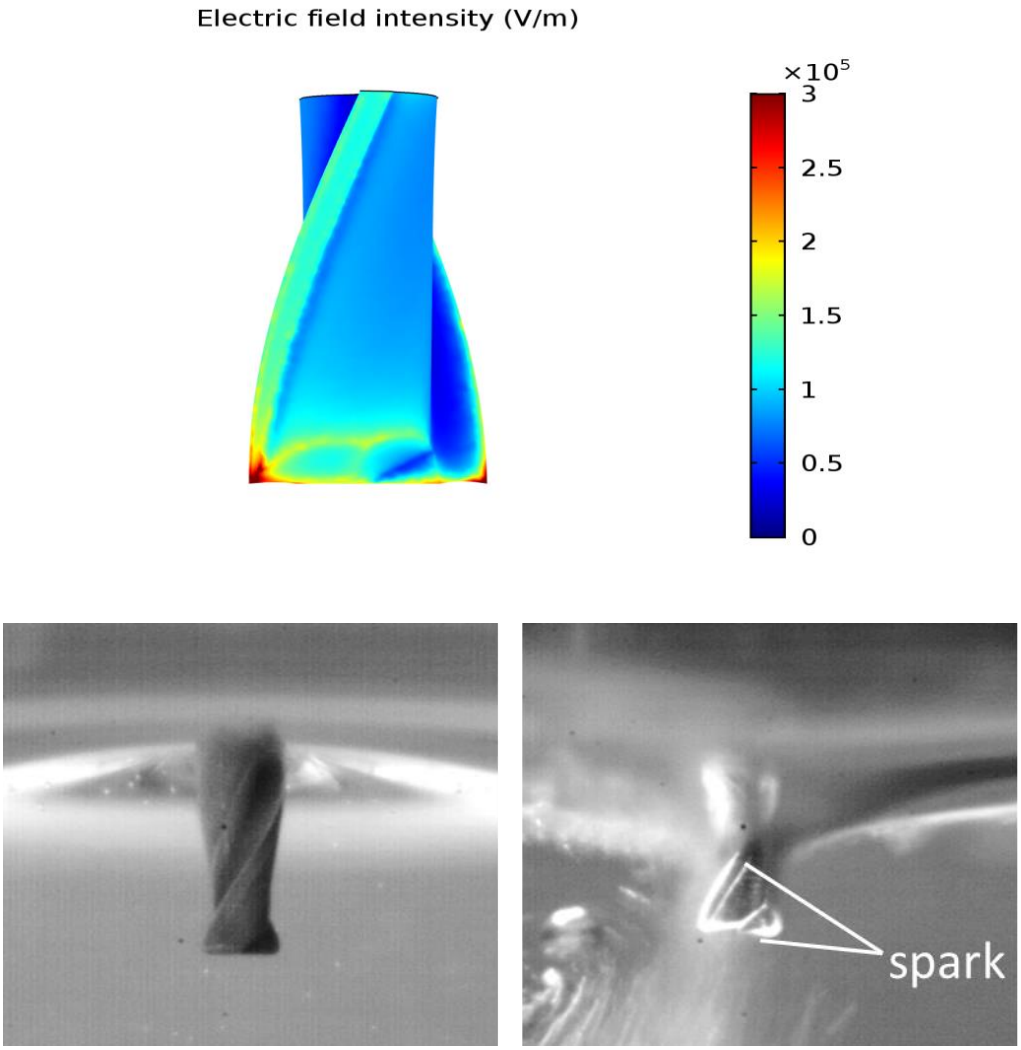

Figure 5.3. Electric field simulation vs. discharging experiment.

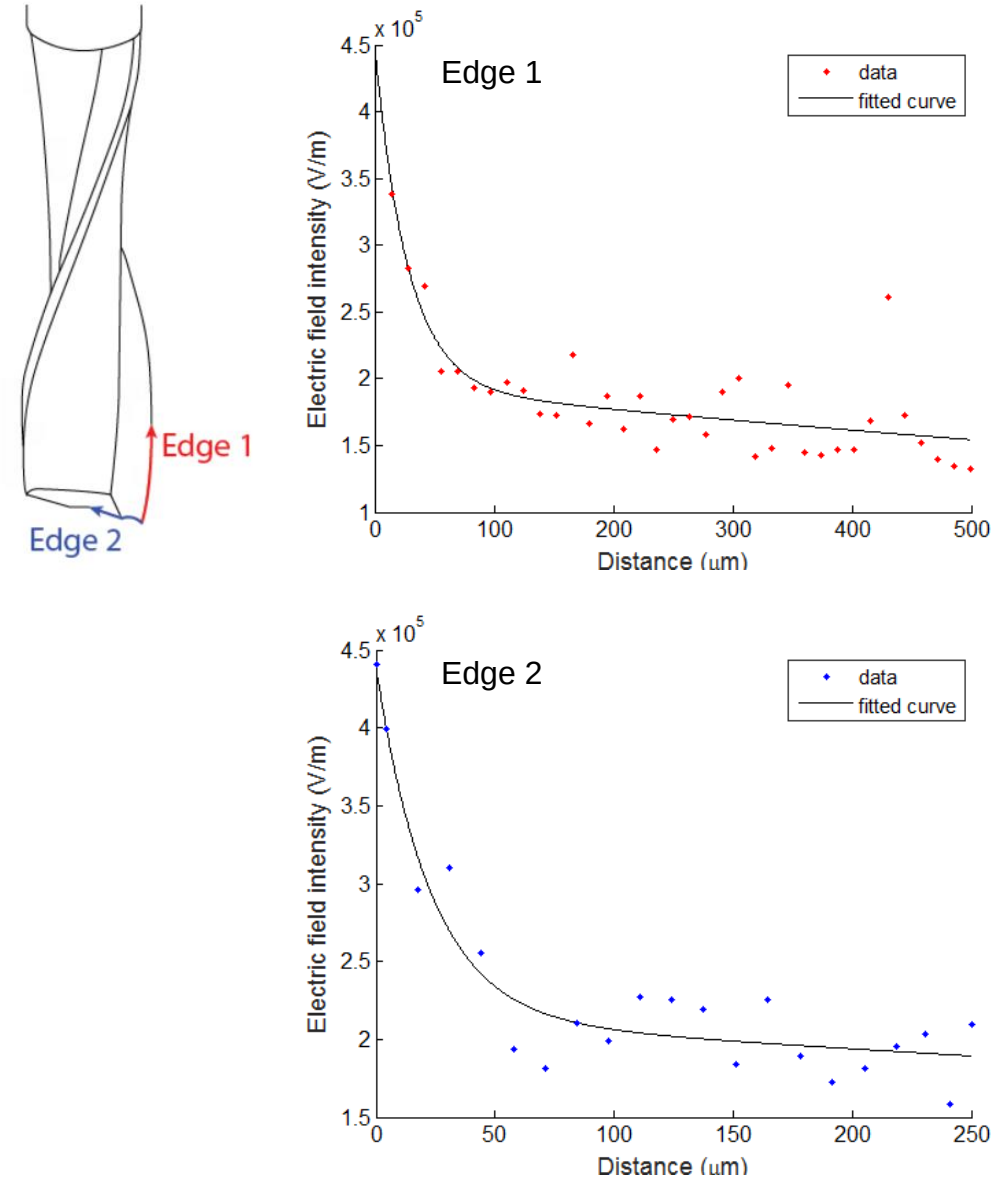

Figure 5.4. Electric field magnitude along cutting edges.

5.3.2 Heat transfer in the material

Once the heat source for discharging is determined, the following step is to set up the heat transfer problem inside the material. There are some concerns in this scenario that do not pertain to a classic heat transfer problems:

- Material is being removed, by heat and by mechanical force. The geometry is changing in the simulation process.
- Material being heated during the process. As the process goes, the material is getting heated with every cut due to the additional energy brought in to the material.

The governing equation for heat transfer in solids is:

$$\frac{\partial T}{\partial t} - \alpha \nabla^2 T = 0 \tag{5.7}$$

where T is the temperature field, α is the thermal diffusivity of the material. The boundary conditions are:

$$-k \frac{\partial T}{\partial n} = h\left(T - T_\infty\right) \tag{5.8}$$

where k is the heat conductivity, h is the heat transfer coefficient, T_∞ is the ambient temperature.

The problem is simulated with FEA in Abaqus. The schematic is shown in Figure 5.5.

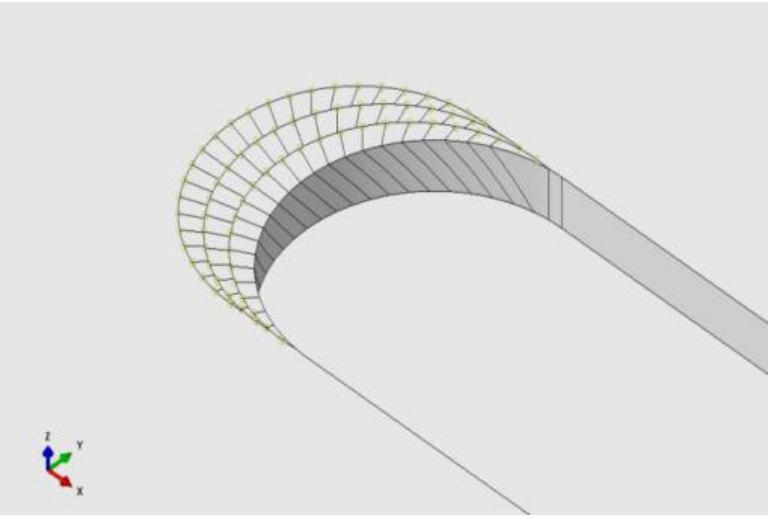

Figure 5.5. FEA setup of heat transfer in the material.

As is shown in the figure, a groove cutting process is simulated. The partitioned area in the center is the material to be removed in the process. As simulation time goes, these pieces are removed one by one according to actual tool angular velocity to emulate the mechanical material removal. A total of 3 half-revolution are simulated to validate the “warm-up” effect.

The line heat source is applied right next to the most recently removed piece. The distribution of heat source follows the simulation results of the electric field intensity (squared).

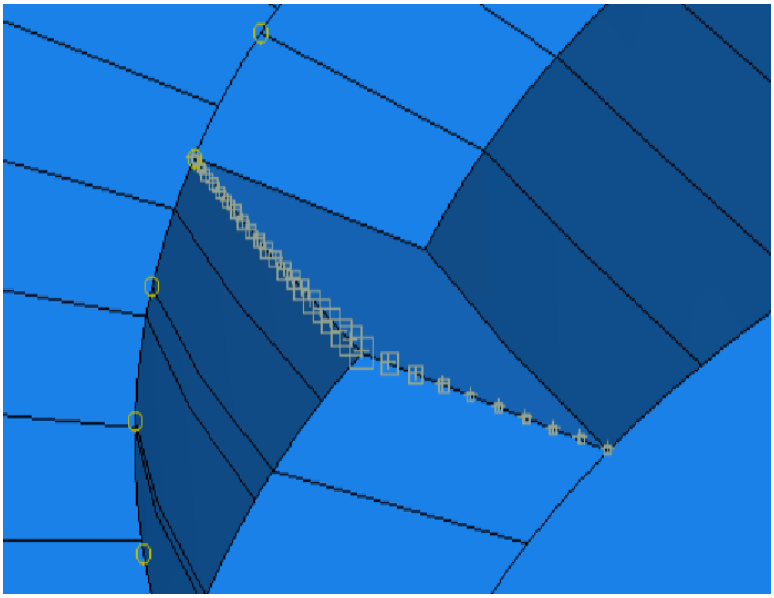

Figure 5.6. Element removal and node heat input in FEA.

All exposed surfaces are subject to natural convection with the electrolyte. The simulated workpiece is a square with 25 mm in length and 1 mm in thickness. Comparing with the 0.5 mm groove width, the workpiece is large enough so that the boundary effects are negligible.

An example of simulation result is shown in the following figure. The core area with a brigher color is the region with high temperature and is removed by heat. The outer area has a lower temperature and is presumably removed by mechanical force.

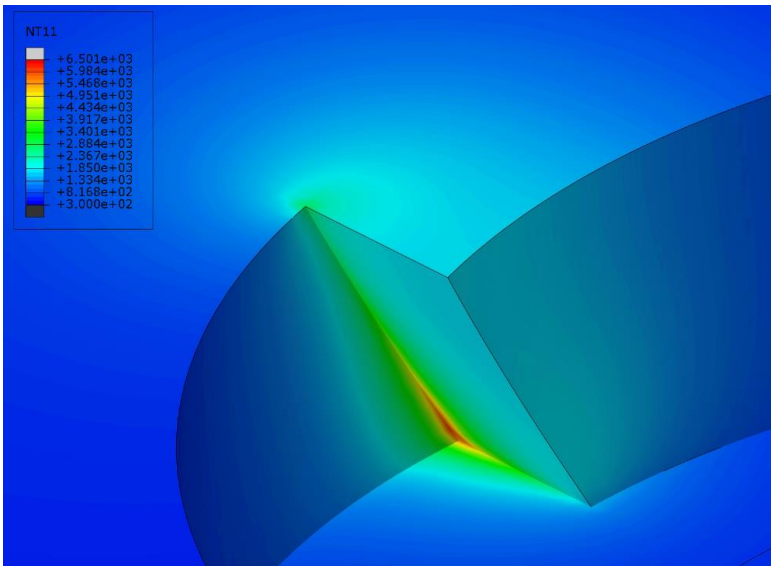

Figure 5.7. Temperature profile inside the material.

5.3.3 Discussion and validation

There are a few things that can be noticed in the simulation.

Short term "warm-up" effects are negligible in the simulation. The simulation goes through three cutting cycles and the temperature profile near the cutting area is very consistent. The discrepancy in the heated zone is less than 5% within the three cycles. The heat capacity of the electrolyte is much higher than the workpiece and can effectively remove heat from the material through convection. On the other hand, if the process operates for a long time, the rise in electrolyte temperature may affect the accuracy of the simulation.

A recolored contour plot demonstrates the status of the material. A small area near the cutting edge with the red color indicates the material removed by heat. A larger area outside of that indicates the softened material, in which the temperature does not reach the melting point, is removed by mechanical cutting force. The softened material is much larger in volume, demonstrating the vast potential in enhancing material removal rate with the hybrid process.

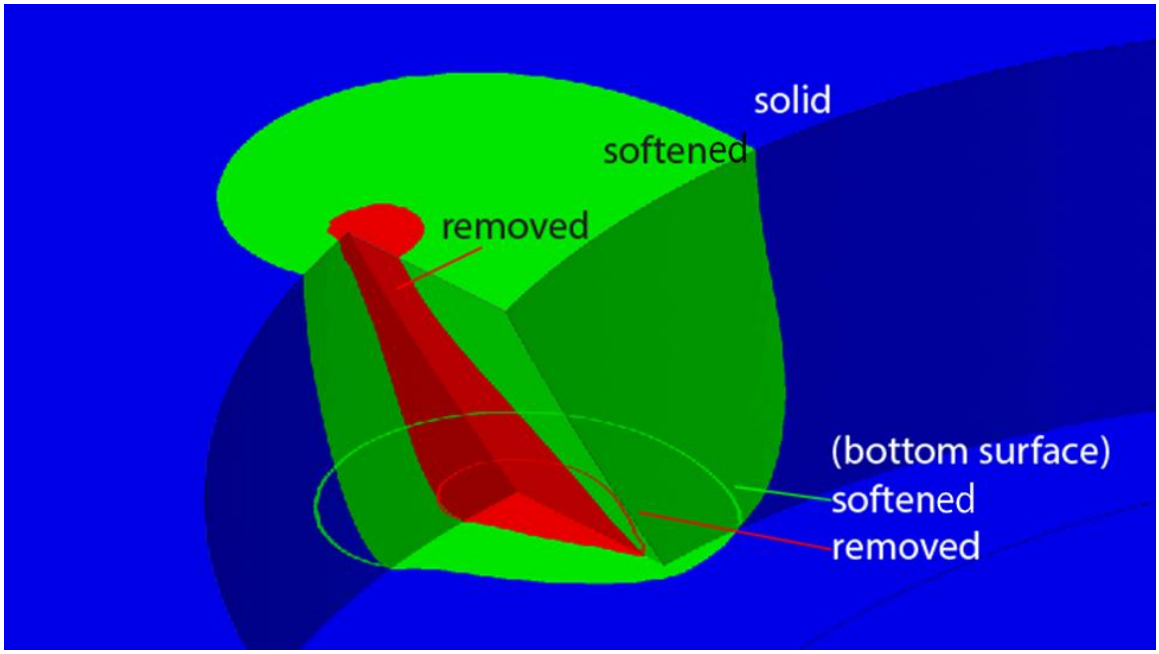

Figure 5.8. Temperature contour plot, showing three material status.

There are some measures that can be quantified from the simulation. For the purpose of better illustration, a 2-D schematic is provided in Figure 5.9. The margins are exaggerated for better visual effects.

The material chip thickness reaches a maximum around the midpoint and requires the most heat or cutting force within a cycle. To simplify the scenario, two temperature lines are drawn to illustrate the regions of three material statuses: molten, softened, or solid. In the figure, d_1 represents the width of thermally removed region. If the feed distance between two cuts is less than d_1, thermal power is capable of removing any material along the tool trajectory and therefore no mechanical cutting is involved in the process. Another metric in figure is d_2, the width of thermally softened region. To prevent cutting cold solid material, the feed distance should be less than d_2.

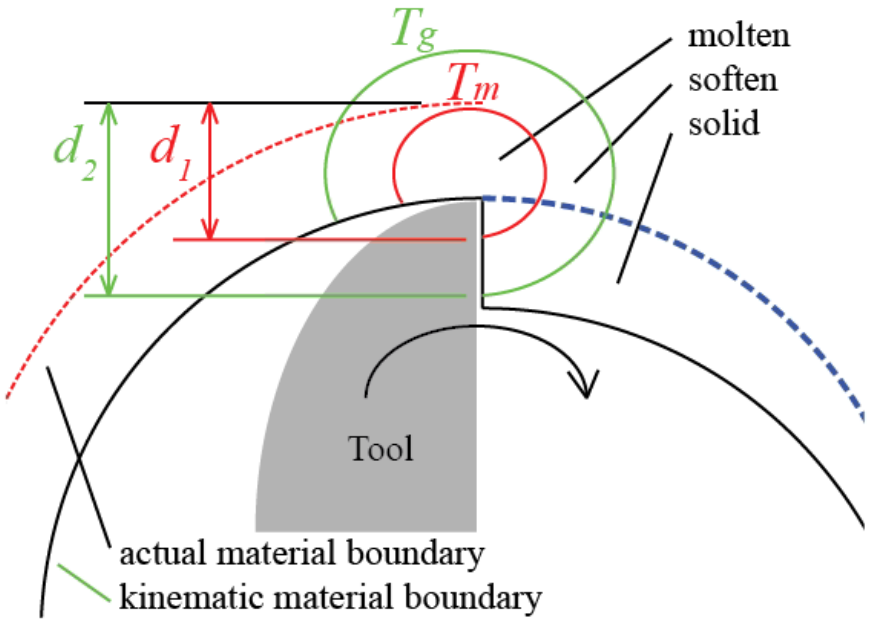

Figure 5.9. Schematic of temperature contour plot.

One interesting observation from Figure 5.8 is that molten area is wider on the bottom surface, while the softened area is wider on the top surface. It is quite straightforward that material closer to the bottom receives more heat input due to the intense discharging near the tip of the tool, and therefore results in larger thermally removed area. Softened material behaves differently though. The width of softened zone is slightly wider at the top, where heat input is actually the lowest. This phenomenon is related to the geometry of the helical cutting tool. The nature of helical shape makes the upper part of the tool lags in phase comparing with the lower part. Therefore the heat from the lower cutting edge takes a shortcut and preheats the material before the cutting edge reaches any point at the top surface. It can be indicated that minimum thermal removal (d_1) is at the top surface, while minimum softening (d_2) is at the bottom surface.

The validation of the model is closely related to d_1 and d_2 from the simulation. If the feed distance between cuts is less than d_1, the tool tip cannot reach the material boundary created by the previous cutting cycle, resulting in no mechanical contact and zero cutting force. If the feed

distance is more than d_2, the tool reaches beyond the softened material zone and cuts solid material, while causes undesirable cracks and surface damages.

Such phenomenon can be observed from the groove cutting experiment. The dynamometer under the fixture records the cutting force with high bandwidth due to the rigidity of the fixture. An example of force signals is shown in Figure 5.10.

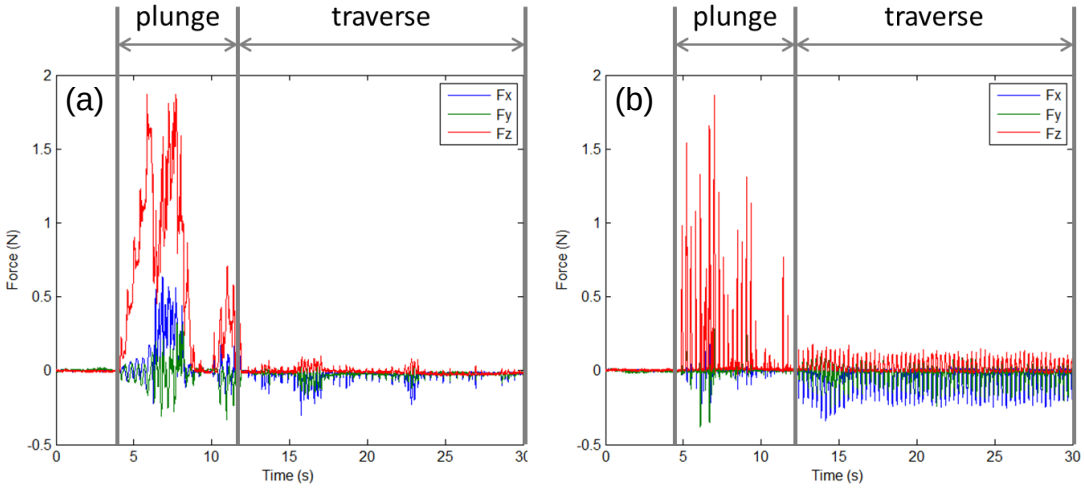

Figure 5.10. Cutting force signals in groove cutting experiments.

(a) No mechanical cutting. (b) Consistent mechanical cutting.

There are two stages in the groove cutting experiments. First, a hole is drilled and the flat end mill reaches the desired depth of cut. This corresponds to the "plunge" stage in the figure, where z-direction force is very large. Then the workpiece moves along a certain direction, and this corresponds to the "traverse" stage in the figure. The two set of experiments in Figure 5.10 illustrate two process statuses: with and without mechanical removal of material. Although the cutting force in the traverse stage of Figure 5.10(a) is not strictly zero, the non-consistent cutting force is due to the instability of electrochemical discharging. On the contrary, the cutting force in Figure 5.10(b) demonstrates a stable, cyclic pattern.

If the feed rate continues to rise, there is a chance that failure may occur. Instead of breaking the tool or workpiece immediately, the tool bends elastically at the beginning and breaks once the maximum strength is reached. Sometimes the increased contact force from elastic bending can increase the mechanical removal and prevents further tool deformation, resulting in a marginal failure pattern where the cutting tool is elastically deformed through the entire cutting process. In both cases cutting happens outside the softened material region and is not desirable in the process.

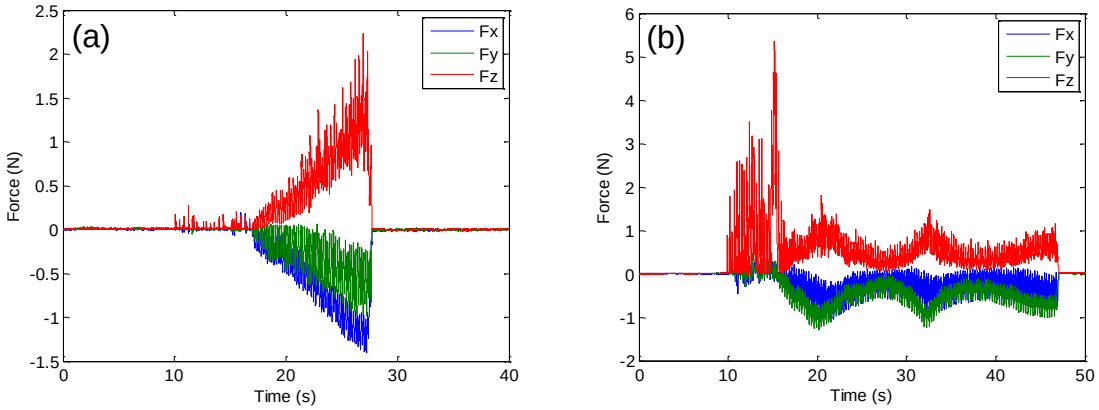

Figure 5.11. Cutting force signals in groove cutting experiments.

(a) Failure. (b) Marginal failure.

By adjusting the feed rate and comparing the force signals, two transition points can be found. There is a certain feed rate that uses maximum thermal power and one that uses maximum thermal plus mechanical power.

To validate the heat transfer model, a series of groove cutting experiments are carried out. The electrode voltage is 42 V, with tool immersion depth of 2 mm. Spindle speed is set to 160 rpm. Depth of cut changes from 50 – 200 μm. Each test is repeated three times. The results are

shown in Table 5.1. The major source of uncertainty comes from the resolution error of the CNC machine as the programmable minimum feed rate increment is 2 mm/min, or 3.1 μm/teeth.

Table 5.1. Critical feed rate in groove cutting experiments.

Experiment results		
Depth of cut μm	**Feed rate (no force)** d_1 μm	**Feed rate (tool break)** d_2 μm
50	40.6	78.1
100	21.9	46.9
150	9.4	28.1
200	3.1	21.9

Table 5.2. Critical feed rate in groove cutting simulations.

Simulation results				
Depth of cut	d_1	d_2	**Error** d_1	**Error** d_2
μm	μm	μm	μm	μm
50	37.7	82.4	-2.9	4.3
100	18.3	50.0	-3.6	3.1
150	6.1	29.7	-3.3	1.6
200	4.3	24.9	1.2	3.0

The material heat transfer simulations are set up using the same process parameters. The results are shown in Table 5.2. It can be seen from the table that the prediction is consistent with the experimental results. There is a slight under estimation of thermally melted material, as well as a slight overestimation of the softened material. A potential reason for this is that the material

properties of the workpiece used in the experiments do not perfectly line up with parameters used in the simulation. But the overall quality of the heat transfer model is reasonable enough and the model can be validated with experiments.

5.4 Cutting force

Cutting force during machining is closely related to product quality. A common concern in brittle material machining is surface fracture and sub-surface damage due to high cutting force. With the aid of discharging, material can be softened so that fracture can be significantly reduced. However, cracking could still take place with any excessive load. It is essential to ensure that the material does not sustain high stress to avoid cracks or rough surfaces. Therefore the cutting force becomes an essential performance variable in the machining process. A comprehensive model that precisely predicts cutting force based on various input process parameters can be very helpful in terms of tracking and optimizing the process, including determining maximum material removal rate, feed rate, spindle speed, and depth of cut.

It has been decades since researchers started to investigate the mechanical cutting force in a variety of applications. The achievements cover the majority aspects of conventional mechanical cutting. However, the conventional cutting force models are not applicable to the EDAC process due to the following reasons:

- The mechanical properties of amorphous materials are highly temperature dependent. As electrochemical discharging heats up and softens the material, it behaves like viscous fluid. This differs from classic cutting force model in fundamentals and intrinsic equations.

- Thermally removed material makes it hard to evaluate the geometric factors in cutting using the classic theory. A critical parameter in classic cutting force models is the chip thickness. The involvement of thermal removal reduces the geometric chip thickness and therefore makes the classic model invalid.

A generic cutting force model is established to predict local and global cutting force. The input covers the fundamentals of tool and material properties, including tool geometry, mechanical properties of glass, as well as process parameters such spindle speed, feed rate, and depth of cut. Machining defects and tool failure should be predicted based on the estimation of cutting force by the model.

5.4.1 Elemental cutting tool and governing equations

Cutting force, by definition, comes from the mechanical interaction between the tool and the workpiece. The geometry of the tool, however, can be very complicated. In early days, researchers treat the cutting process as a black box and empirically build correlations between the tool properties including size, helix angle, and number of flutes (Koenigsberger and Sabberwal, 1961). This restricts the scope of application and reduces the robustness of the cutting force model. Modern models overcome such weakness by virtually breaking the tool into small pieces and modelling them independently. There are many successful attempts using similar principles like this, under the name of elemental cutting tool method (Kline et al., 1982, Omar et al., 2007).

The essential idea of developing the force model is to analyze a simplified scenario, where the cutting tool with complex geometry is decomposed into small, linear, 2-D cutting elements, or elemental cutting tool (ECT). The global forces will be obtained by traversing

through every point on the real tool and adding up the cutting force on each of the ECT blades. Figure 5.12 illustrates an example of tool partitioning and force components. The tool is partitioned into horizontal discs with 4 μm thickness. Each disc contains 2 ECTs as two-flute mill bits are used.

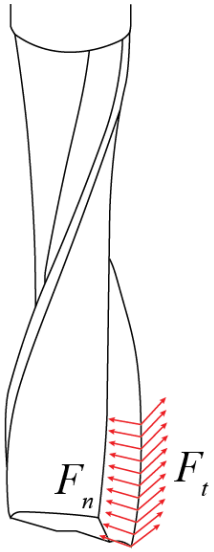

Figure 5.12. Elemental cutting tool (ECT).

The basic cutting scenario with every one of the ECTs is shown in Figure 5.13: the blade moves at a certain velocity to cut the material with a certain thickness.

The conventional cutting model builds a simple intrinsic correlation under this scenario. It is believed that both incremental tangential and normal cutting forces are proportional to the chip thickness t_c and width w (Omar et al., 2007):

$$\begin{aligned} \Delta F_t &= K_t t_c w \\ \Delta F_n &= K_n t_c w \end{aligned} \tag{5.10}$$

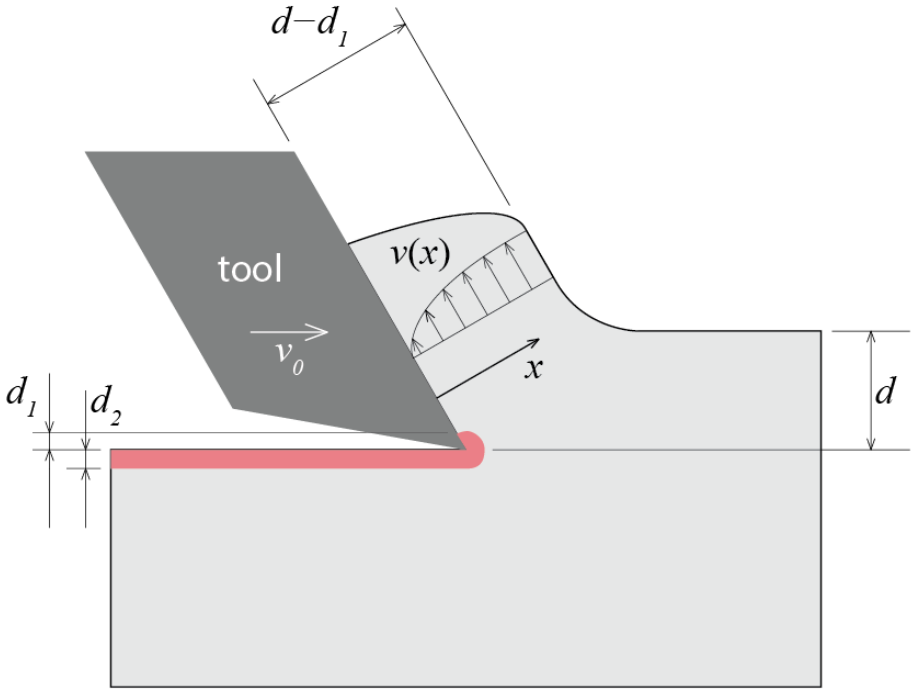

Figure 5.13. Basic cutting scenario with an ECT.

The coefficients K_t and K_n are either constants derived from the material properties, or functions of process parameters including cutting speed and angle (Chandrasekharan et al, 1995). However amorphous materials have a large transition phase between its solid and liquid state. The transition state of glass behaves like a viscous fluid with extremely high viscosity. High viscosity makes the flow fully laminar and therefore analytical solution becomes possible. It should be addressed that the viscosity is also highly temperature dependent so that temperature gradient inside the material will be taken into account.

Assume the removed material forms a fully developed flow on the surface of the blade. Hence the change in fluid velocity, *v(x)*, only occurs in perpendicular directions. The cutting force on the blade is equal to the shear force of the fluid, *τ(x)*, at the interface. The temperature distribution and the fluid viscosity are denoted as *T(x)* and *μ(T)* respectively.

The shear force of the Newtonian fluid is proportional to the velocity gradient of the fluid:

$$\tau = \mu \frac{dv}{dx} \tag{5.11}$$

The shear force should maintain constant in free laminar flow. Hence a differential equation of fluid motion can be derived by setting the derivative of shear force to be zero:

$$\frac{d\tau}{dx} = \frac{d}{dx}\left(\mu \frac{dv}{dx} \right) = 0 \tag{5.12}$$

$$\frac{d\mu}{dT}\frac{dT}{dx}\frac{dv}{dx} + \mu \frac{d^2 v}{dx^2} = 0 \tag{5.13}$$

In the equation of motion, velocity function is the only unknown function: viscosity is given by material properties and temperature distribution can be determined by the thermal model. The corresponding boundary conditions are as following:

$$\begin{aligned} v(0) &= 0 \\ v(d) &= v_0 \end{aligned} \tag{5.14}$$

Once the velocity function is determined, the shear force on the blade interface can be determined.

5.4.2 Chip formation

In this section, chip formation processes in the EDAC are discussed. An analytical model is developed to predict chip thickness, entrance angle, and the exit angle.

A major difference between the EDAC and the traditonal cutting is the thermal overcut. This results in differenct chip formation process. Figure 5.14 shows a comparision of the basic cutting schematics.

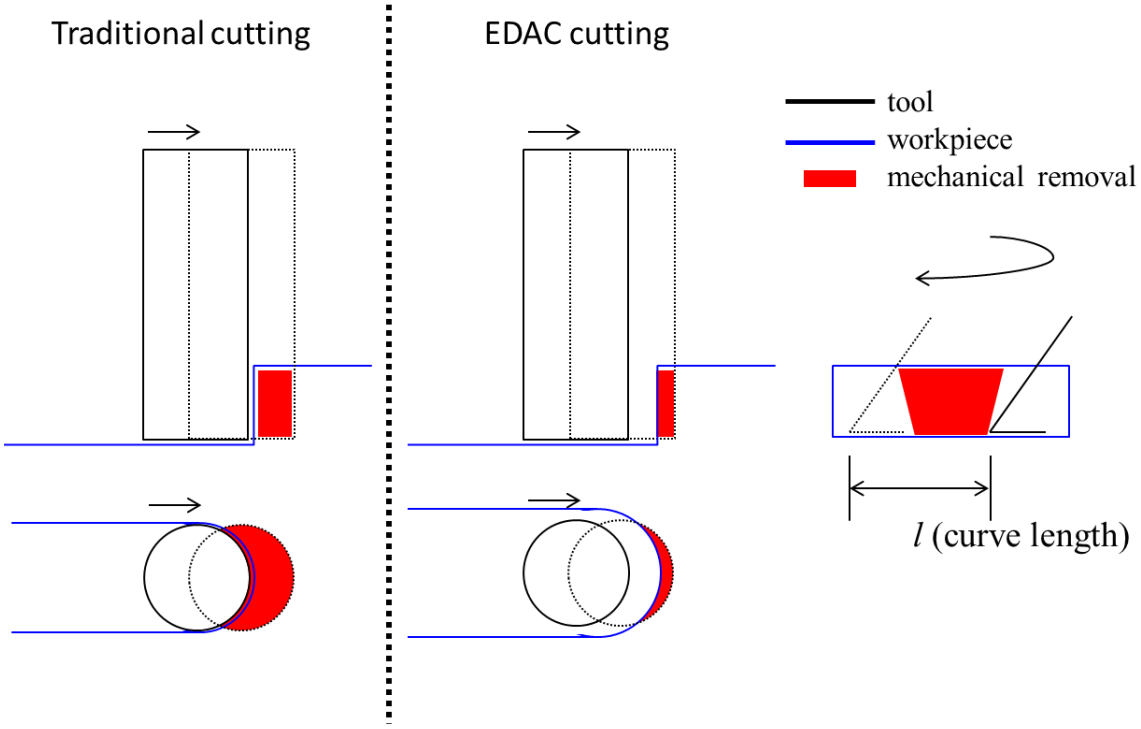

Figure 5.14. Cutting schematic. Traditional cutting vs. EDAC.

If can be found that the chip in the EDAC is much smaller than tha in the traditonal counterpart under the same feed rate and spindle speed. Another interesting observation is that mechanical cutting only takes place in a window during a cutting cycle. The width of the window may or may not cover the entire cutting cycle. If the length of the cutting window *l*, is less than the arc length of the tool tip trajectory, the mechanical engagement only partially covers the cycle. In other words, mechanical cutting only takes place in a proportion of time in a cutting cycle. Such phenomenon can be found from the groove cutting experiments (Figure 5.15). In both tests electrochemcal power is the same (electrode voltage = 40 V; emmersion depth = 2 mm;

NaOH concentration = 30%). With higher feed rates (8 mm/min) and depths of cut (200 μm), the force signal is continuous. While the gaps between loads are obvious with lower feed rate (4 mm/min) and depth of cut (200 μm).

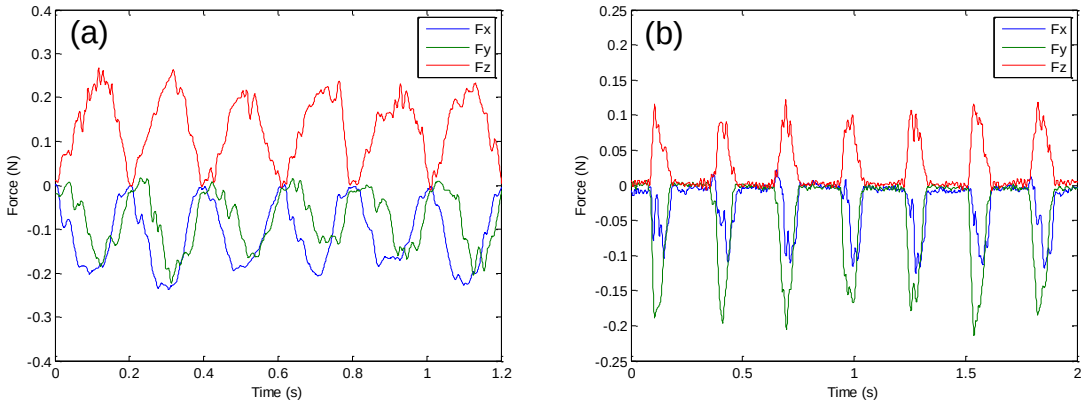

Figure 5.15. Cutting force signals in groove cutting.

(a) Continuous loads. (b) Discountinuous loads.

5.4.3 Chip thickness model

One option to model chip formation in the EDAC is to adpat the model for traditional cutting with overcut. However, the overcut in the EDAC can be very significiant, and it magnifies the asymmetricity between the entrace and the exit point. Therefore a chip formational model is created to predict the chip thickness as a function of time, as well as the entrance and exit points. The following figure shows the schematic of the formation of a single chip. The red line indicites the trajectory of the cutting edge. The solid blue line is the trajectory of the previous cut. With the thermal overcut, the actual material boundary is pushed further back, as is indicated by the dotted blue line. The moon shape area between the dotted blue line and the red line is the material to be removed.

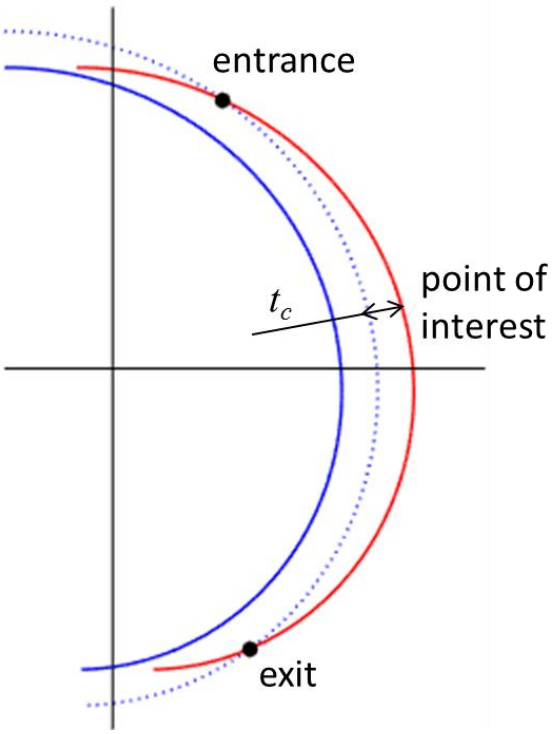

Figure 5.16. Schematic of single chip formation.

The dotted blue line, as a function of time, is noted by ($x_0(t)$, $y_0(t)$), and can be defined as the following:

$$\begin{aligned} x_0(t) &= v_f t + (r + r_{oc})\cos\left(-\omega t - \frac{\pi}{2}\right) \\ y_0(t) &= (r + r_{oc})\sin\left(-\omega t - \frac{\pi}{2}\right) \end{aligned} \tag{5.15}$$

where r is the tool radius, r_{oc} is the overcut, v_f is the feed rate, and ω is the angular velocity of the tool. Similarly, the red line, with the cordinates of ($x(t)$, $y(t)$), can be written as

$$\begin{aligned} x(t) &= v_f t + r\cos\left(-\omega t + \frac{\pi}{2}\right) \\ y(t) &= r\sin\left(-\omega t + \frac{\pi}{2}\right) \end{aligned} \tag{5.16}$$

The entrance and exit points are the points of intersection, where

$$\begin{aligned} x_0(t_1) &= x(t_2) \\ y_0(t_1) &= y(t_2) \end{aligned} \tag{5.17}$$

Combining Equations 5.11 - 5.13, the equations for entrance and exit points are as the following:

$$\begin{aligned} & v_f(t_1 - t_2) + (r + r_{oc})\cos\left(-\omega t_1 - \frac{\pi}{2}\right) - r\cos\left(-\omega t_2 + \frac{\pi}{2}\right) = 0 \\ & (r + r_{oc})\sin\left(-\omega t_1 - \frac{\pi}{2}\right) - r\sin\left(-\omega t_2 + \frac{\pi}{2}\right) = 0 \end{aligned} \tag{5.18}$$

where t_1 and t_2 are the only unknown variables. The solutions within range

$$\begin{aligned} t_1 &\in \left(0, \frac{\pi}{\omega}\right) \\ t_2 &\in \left(\frac{\pi}{\omega}, \frac{2\pi}{\omega}\right) \end{aligned} \tag{5.19}$$

indicate the time that the tool tip passes the entrance and exit points. The corresponding coordinate is ($x(t_1)$, $y(t_1)$) and ($x(t_2)$, $y(t_2)$), respectively.

To determine the chip thickness, consider an arbitary point on the red line ($x(t)$, $y(t)$). The velocity at the point is

$$\begin{aligned} v_x(t_1) &= \left.\frac{dx}{dt}\right|_{t=t_1} = v_f + \omega r \sin\left(-\omega t_1 + \frac{\pi}{2}\right) \\ v_y(t_1) &= \left.\frac{dy}{dt}\right|_{t=t_1} = -\omega r \cos\left(-\omega t_1 + \frac{\pi}{2}\right) \end{aligned} \tag{5.20}$$

Chip thickness is calculated at the direction perpendicular to velocity, by solving the following equation:

$$x(t_1)+t_c\frac{v_y(t_1)}{\sqrt{v_x{}^2(t_1)+v_y{}^2(t_1)}}=x_0(t_0)$$
$$y(t_1)-t_c\frac{v_x(t_1)}{\sqrt{v_x{}^2(t_1)+v_y{}^2(t_1)}}=y_0(t_0) \tag{5.21}$$

$$t_0\in\left(0,\frac{\pi}{\omega}\right)$$
$$t_c\in\left(0,\frac{\pi v_f}{\omega}\right) \tag{5.22}$$

where t_1 is the input, t_c and t_0 are unknowns. Functions x, y, x_0, y_0, v_x, v_y are defined by Equation 5.12 - 5.16.

Since the point of interest is arbitrary, the function of chip thickness can be obtained by iteratively going through all points on the active trajectory. For example, using the process parameters in the experiment in Figure 5.15 (right), the chip thickness function within a cycle can be determined.

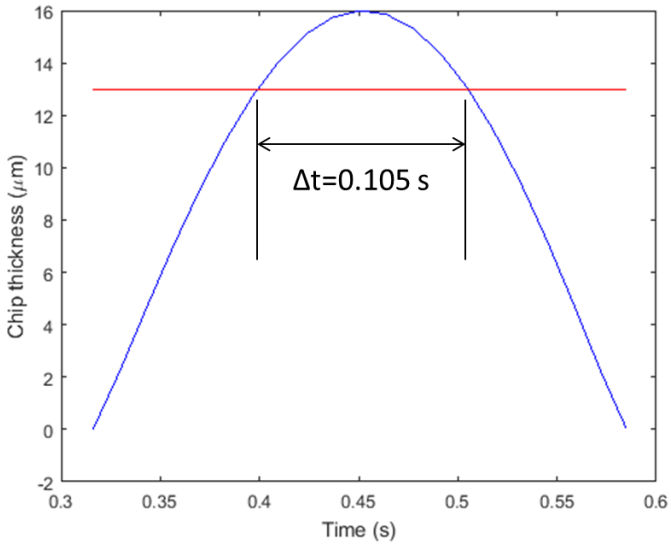

Figure 5.17. Chip thickness variation.

As is previously discussed that mechanical cutting only takes place if the geometricl chip thickness is larger than the thermal overcut. By drawing a horizontal line at that level, the active time interval for cutting can be evaluated. The simulated value of 0.105 s (35%) is consistent with the experimental measurement of 0.114 ± 0.011 s (38 ± 4%).

5.4.4 Validation

To validate the chip thickness model, a series of experiments are conducted. The eletrochemical power remains the same through all tests with 40 V electrode voltage, 2 mm immsersion depth, and 30% NaOH concentration. By changing the depth of cut (DOC) and feed rate, different mechanical load percentage can be obtained. The results are shown in Table 5.3. It can be shown that the predicted load percentage is consistent with the experimental result using the chip thickness model.

Table 5.3. Validation of chip thickness model.

DOC (μm)	**Feed (mm/min)**	**Measured mechanical engagement (%)**	**Predicted mechanical engagement (%)**	**Error (%)**
200	4	38±4	35	-3
200	6	62±5	58	-4
200	8	100	100	0
100	6	30±7	28	-2
100	8	36±4	32	-4
100	10	40±8	38	-2
100	12	50±3	48	-2
100	14	69±7	63	-6
100	16	100	90	-10

5.5 Results and discussion

The major improvement for the EDAC cutting force model, comparing with the traditional cutting force model, comes from the following aspects:

- The linear intrinsic equation in the ECT scenario is replaced with a viscous fluid model. Therefore temperature dependency can be analytically calculated and involved in the cutting force simulation.
- A new chip thickness model is built to better deal with thermal removal. The new chip thickness model correctly predicts the no-load interval in groove cutting and is validated by experiment.

Figure 5.18 shows an example of cutting force simulation. The process parameters are as following:

Electrode voltage	40 V
Depth of immersion	2 mm
NaOH concentration	30 wt. %
Spindle speed	160 rpm
Feed rate	8 mm/s
Depth of cut	200 μm
Tool diameter	500 μm

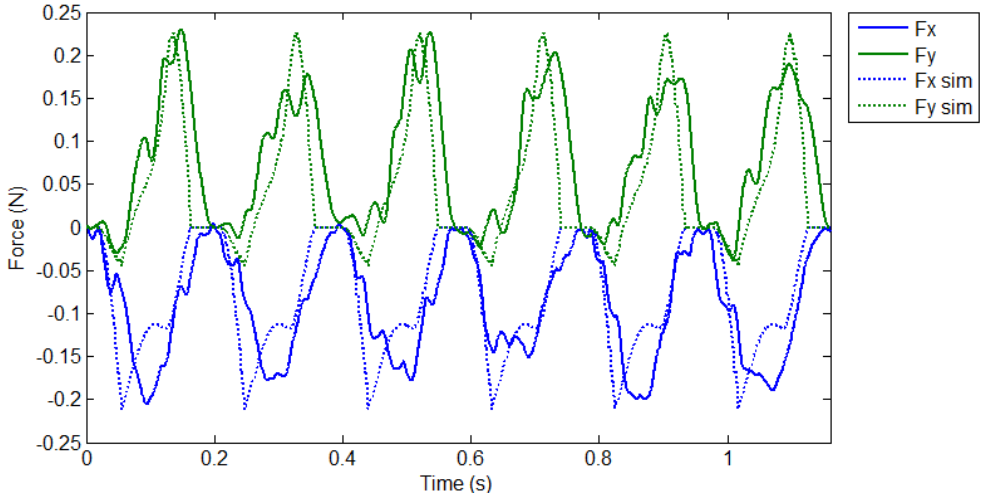

Figure 5.18. Cutting force simulation vs. experiment.

Figure 5.18 indicates that the cutting force model catches some of the features from the experiment:

- Phase difference. There is a clear phase difference between F_x and F_y signals, and the model predicts that phase well.
- Magnitude. The peak magnitude of the predicted force signals is consistent with the experiments in terms of both value and ratio. The experiment indicates that the magnitude of F_y is slightly higher than F_x, and the model captures this ratio in the simulation. Overall the model seems to slightly overestimate the force, but the overestimation is in a reasonable range.
- Waveform shape. Although the real signal is noisy, there is a clear pattern that the rising edge has a larger slope than the declining edge for F_x, while the rising edge has a smaller slope than the declining edge for F_y. The simulation demonstrates this pattern as well.

As a benchmark, the viscous fluid equation and the chip thickness model are replaced with traditional counterparts. Some necessary adaptions are made to better address issues including overcutting. Figure 5.19 shows the force simulation result within one full revolution of the tool. It can be seen that the traditional model is worse in terms of both magnitude and waveform shape.

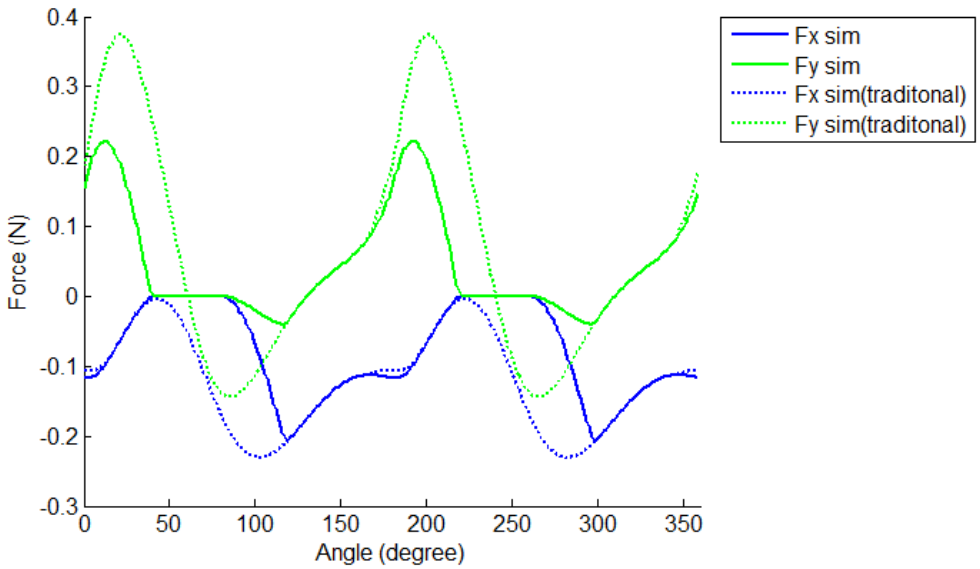

Figure 5.19. Force simulation with traditional model.

5.6 Conclusions

In this chapter, a material removal model in the EDAC is introduced. The thermal-mechanical properties of amorphous materials are analyzed, and a material heat transfer model is proposed to determine the temperature profile and therefore account for the highly thermal dependent material behavior. The electrochemical discharging, as the heat source in the process, is modeled analytically and is followed up with finite element simulations to determine the heat distribution on the tool electrode. Once the heat input is determined, the heat transfer problem can be solved using numerical simulation. The temperature profile can therefore divide the material into three

zones: thermally removed, softened, or solid. A cutting force model is created to estimate the overall cutting force that addresses the thermal removal and the thermal dependent mechanical behavior. The specific findings and conclusions are:

- Amorphous materials can be significantly softened at much lower temperature than the melting point. Mechanical cutting can be effective in removing the softened material.
- Electrochemical discharging energy is proportional to the square of the electric field intensity. Therefore discharging is very intense along the sharp cutting edges. It is a proper practice to emulate the tool with line heat source in heat transfer problems due to the fact that the majority of the energy is released at the edges.
- Discharging results in heated material with three status: removed, softened, or solid. Softened region can be much larger than the removed region, indicating the high potential of the hybrid process in terms of material removal capability.
- Cutting force is an essential parameter in finding out the limit of maximum material removal with the EDAC. The traditional cutting models cannot fully address the problems in the hybrid process. The proposed cutting force model can effectively predict the cutting force as a function of time, and performs significantly better than the adapted traditional methods.

Chapter 6

Conclusions and Recommendations for Future Study

6.1 Conclusions

The electrochemical discharge assisted cutting is a novel machining process targeting at three dimensional machining of hard-to-machine materials. This research consists of the development and analysis of the EDAC, as well as modeling of the electrochemical discharge phenomenon. The major contributions of this research are in the following aspects:

- A novel machining process is created to effectively cut glass. The feasibility of the EDAC is demonstrated by cutting soda-lime glass sample. The drilling process is introduced first. By incorporating mechanical micro-drilling with electrochemical discharge machining, the drilling process is not only improved in terms of the material removal rate, but in consistency of feed rate and surface quality. The assistance of vibration can further enhance the effectiveness of drilling. The correlations and effects of process parameters are empirically determined. It is concluded that there is no single combination of parameters that has optimal performance in all conditions. The tradeoff for higher material removal rate is the large overcut, rough surface finish, cracks, and

subsurface damages. The process parameters should be chosen depending on the specific needs of applications.

- The EDAC milling process is also investigated. The hybrid process can increase the material removal rate dramatically comparing with the traditional ECDM or cutting processes. Tungsten carbide flat end mill bit is a good option for both electrochemical discharge and mechanical cutting. Using the side of the tool instead of the bottom enables more effective mechanical cutting. It can be found from the groove cutting experiments that overcut and surface quality are the major concerns for accuracy in the milling process. Similar to drilling, higher electrode voltage increases material removal rate, but increases overcut and surface roughness as well. The overcut is empirically determined so that the impacts can be compensated in the process of tool path planning.
- Models are created to characterize the electrochemical discharge phenomenon. The electrochemical discharge phenomenon is the fundaments of the EDAC and is extensively studied in this research. The models developed are beneficial not only to the EDAC, but also to many other non-traditional machining processes facilitating this phenomenon. The physics-based models of bubbles and the gas film are established to determine bubble and film behavior, as well as electrochemical properties. The energy level of sparks is also measured, revealing a stochastic phenomenon in energy distribution. Not only does the model reveal the underlying physics behind the electrochemical discharge phenomenon, but also provides an analytical basis to model the material removal in the EDAC process.
- As the outcome of all prerequisite models, a material removal model is created. The model consists of multiple parts that are inherently related. The mechanical properties of

amorphous materials are highly temperature dependent, and therefore a heat transfer model is created to determine the temperature profile inside the material. It is found that apart from a small proportion of material which is directly removed by heat, a larger proportion of material is softened, making mechanical cutting to be very effective. A cutting force model is set up to estimate the contact force between the tool and the material, which is essential to determining the status of cutting processes and tracking brittle damages of the workpiece.

6.2 Recommendations for future study

The experimental investigations in this study cover both drilling and milling processes. The drilling process is inherently simpler than the milling process. After taking many approaches for improvement, the drilling process reaches a state of being capable of drilling many types of holes with reasonable accuracy and speed. The majority of the problems that remain unsolved comes from deep hole drilling. Electrochemical discharging can effectively remove materials at the early stage of drilling. However, it becomes ineffective in deeper hole drilling because replenishing electrolyte inside the drilled hole can be challenging. The incorporation of mechanical vibration can mechanically push out the debris and replenish the electrolyte, but the brittle damage to the surface is undesirable. An alternative solution is to design flow channels on the surface of the cylindrical electrode. The channels can reduce blockage of the tool and actively regulate the flow field near the tool electrode.

On the other hand, the milling process still leaves a plenty of room for further exploration. There are many aspects remains unclear, including

- Trapezoidal cross section and the crown feature of the milled groove. The potential reason for this is the electrolyte flow. The sodium hydroxide electrolyte can potentially etch the glass workpiece. The chemical etching process at room temperature is very slow. In the machining process however, heated electrolyte leaves the machining area through high heat impact and forced convection. Heat can significantly speed up the chemical etching process and thus creates a trapezoidal cross section. If the electrolyte flow can be characterized empirically or theoretically, the trapezoidal cross section will become predictable and controllable.
- The cutting tool used in the presented EDAC milling process is a standard flat-end mill bit. The tool is designed and optimized for conventional micro-milling, and therefore is not optimal for the hybrid electrochemical process. One major difference between conventional milling and the hybrid process is debris removal. In the mechanical milling processes, chips are usually continuous and need to be removed through the grooves on the electrode. In the EDAC process however, the majority of the debris are in form of small discrete chips and are pushed out by the vaporization of the electrolyte. If the grooves on the cutting tool can be redesigned to address the different debris removal mechanisms, the performance of the process can be further improved.
- In order to achieve freeform 3-D fabrication, ball end milling is an essential part which is not covered in this study. Ball end milling is very different from flat end milling in many aspects, the most important of which is the distribution of electrochemical discharging. A large proportion of the energy concentrates on the tips of flat end mills, while ball end mills do not have tips. This yields to a more consistent and uniform energy distribution and can presumably reduce thermal damages.

On the other hand, the electrochemical discharge machining process can be further improved and optimized if more of the underlying physic is revealed. In this study, models are created to characterize the gas film formation and the discharging process. But there is still a research gap between the models and the application. The specific issues are:

- One common approach to improve surface quality is to reduce the electrode voltage. Researchers have found that lower electrode voltage can significantly reduce the thermal cracks and improve surface quality. However, the range of applicable electrode voltage is quite small: typically 28 V to 40 V in most studies. Too much thermal energy is released if the electrode voltage is set beyond 40 V, resulting in severe cracks and breakage of the glass workpieces. On the other hand, if the voltage is lower than 28 V, the electric field becomes not strong enough to break down the gas film. If there is a method to have the machining process operates at an electrode voltage that is much lower than the current limit, the surface quality can be significantly improved.
- One potential solution to reduce the critical electrode voltage is to reduce the thickness of the gas film. Electric field intensity is reverse proportional to the thickness of the gas film under constant voltage. Although a gas film formation model that can predict the film thickness is presented in this study, it is hard to control the behavior of the gas film using the model. Reducing the thickness of the gas film while keeping it stable is an essential step to improve the machining process from the fundamental aspects.

REFERENCES

Abou Ziki, J. D., Fatanat Didar, T., & Wüthrich, R. (2012). Micro-texturing channel surfaces on glass with spark assisted chemical engraving. *International Journal of Machine Tools and Manufacture*, *57*, 66-72.

Abramzon, A. A., & Gaukhberg, R. D. (1993). Surface tension of salt solutions. *Russian Journal of Applied Chemistry*, 66, 1473-1480

Adornato, L., Cardenas-Valencia, A., Kaltenbacher, E., Byrne, R. H., Daly, K., Larkin, K., ... & Garçon, V. C. (2009). In situ nutrient sensors for ocean observing systems. In *Proceedings of the Oceanobs' 09: Sustained Ocean observations and Information for Society Conference* (Vol. 2).

Arif, M., Rahman, M., San, W. Y., & Doshi, N. (2011). An experimental approach to study the capability of end-milling for microcutting of glass. *The International Journal of Advanced Manufacturing Technology*, *53*(9), 1063-1073.

Basak, I., & Ghosh, A. (1996). Mechanism of spark generation during electrochemical discharge machining: a theoretical model and experimental verification. *Journal of materials processing technology*, *62*(1), 46-53.

Basak, I., & Ghosh, A. (1997). Mechanism of material removal in electrochemical discharge machining: a theoretical model and experimental verification. *Journal of materials processing technology*, *71*(3), 350-359.

Bhondwe, K. L., Yadava, V., & Kathiresan, G. (2006). Finite element prediction of material removal rate due to electro-chemical spark machining. *International Journal of Machine Tools and Manufacture*, *46*(14), 1699-1706.

Brown, Theodore, Eugene Lemay Jr. and Bruce Bursten. *Chemistry: The Central Science*. Upper Saddle River, NJ. Prentice Hall 2000: Page 884.

Chandrasekharan, V., Kapoor, S. G., & DeVor, R. E. (1995). A mechanistic approach to predicting the cutting forces in drilling: with application to fiber-reinforced composite materials. *Urbana*, *51*, 61801.

Chang, Y. P. (1957). A theoretical analysis of heat transfer in natural convection and in boiling. *Transactions of ASME*, *79*(7), 1501.

Cheng, C. P., Wu, K. L., Mai, C. C., Hsu, Y. S., & Yan, B. H. 2010. Magnetic field-assisted electrochemical discharge machining, *Journal of Micromechanics and Microengineering*, 20(7), pp. 075019.

Cheng, C. P., Wu, K. L., Mai, C. C., Yang, C. K., Hsu, Y. S., & Yan, B. H. 2010. Study of gas film quality in electrochemical discharge machining, *International Journal of Machine Tools and Manufacture*, 50(8), pp. 689-697.

Chiou, Y. C., Lee, R. T., Chen, T. J., & Chiou, J. M. (2012). Fabrication of high aspect ratio micro-rod using a novel electrochemical micro-machining method.*Precision Engineering*, *36*(2), 193-202.

Cole, R., & Shulman, H. L. (1966). Bubble departure diameters at subatmospheric pressures. In *Chemical Engineers Progress Symposium Series*(Vol. 62, No. 64, pp. 6-16).

Dahan, E., Bize, V., Lehnert, T., Horisberger, J. D., & Gijs, M. A. M. (2008). Rapid fluidic exchange microsystem for recording of fast ion channel kinetics in Xenopus oocytes. *Lab on a Chip*, *8*(11), 1809-1818.

Ellis, Williams. *Glass*. New York, NY Avon Books Inc. 1998: Page 5.

Fascio, V., Wüthrich, R., & Bleuler, H. 2004. Spark assisted chemical engraving in the light of electrochemistry, *Electrochimica Acta*, 49(22), pp. 3997-4003.

Foy, K., Wei, Z., Matsumura, T., & Huang, Y. (2009). Effect of tilt angle on cutting regime transition in glass micromilling. *International Journal of Machine Tools and Manufacture*, *49*(3), 315-324.

Fritz, W. (1935), Maximum volume of vapor bubbles, *Physik Zeitschr*, 36(11), 379-384.

Gautam, N., & Jain, V. K. (1998). Experimental investigations into ECSD process using various tool kinematics. *International Journal of Machine Tools and Manufacture*, *38*(1), 15-27.

Haeberle, S., & Zengerle, R. (2007). Microfluidic platforms for lab-on-a-chip applications. *Lab on a Chip*, *7*(9), 1094-1110.

Han, M. S., Min, B. K., & Lee, S. J. (2008). Modeling gas film formation in electrochemical discharge machining processes using a side-insulated electrode. *Journal of Micromechanics and Microengineering*, *18*(4), 045019.

Han, M. S., Min, B. K., & Lee, S. J. (2011). Micro-electrochemical discharge cutting of glass using a surface-textured tool. *CIRP Journal of Manufacturing Science and Technology*, *4*(4), 362-369.

He, X. L., Wang, Y. K., Zeng, Z. Q., Wang, Z. L., & Zhao, W. S. (2012). Electrochemical Machining of Micro Slots Using Shaped Electrode. *Advanced Materials Research*, *497*, 315-319.

Huang, S. F., Zhu, D., Zeng, Y. B., Wang, W., & Liu, Y. (2011). Micro-Hole Machined by Electrochemical Discharge Machining (ECDM) with High Speed Rotating Cathode. *Advanced Materials Research*, 295, pp. 1794-1799.

Jain, V. K., & Adhikary, S. (2008). On the mechanism of material removal in electrochemical spark machining of quartz under different polarity conditions.*Journal of materials processing technology*, *200*(1), 460-470.

Jain, V. K., & Chak, S. K. (2000). Electrochemical spark trepanning of alumina and quartz. *Machining science and technology*, 4(2), pp. 277-290.

Jain, V. K., Choudhury, S. K., & Ramesh, K. M. (2002). On the machining of alumina and glass. *International Journal of Machine Tools and Manufacture*, *42*(11), 1269-1276.

Jain, V. K., Dixit, P. M., & Pandey, P. M. (1999). On the analysis of the electrochemical spark machining process. *International Journal of Machine Tools and Manufacture*, *39*(1), 165-186.

Jalali, M., Maillard, P., & Wüthrich, R. (2009). Toward a better understanding of glass gravity-feed micro-hole drilling with electrochemical discharges. *Journal of Micromechanics and Microengineering*, *19*(4), 045001.

Jiang, B., Lan, S., Ni, J., & Zhang, Z. (2014). Experimental investigation of spark generation in electrochemical discharge machining of non-conducting materials. *Journal of Materials Processing Technology*,214(4), pp. 892-898.

Jui, S. K., Kamaraj, A. B., & Sundaram, M. M. (2013). High aspect ratio micromachining of glass by electrochemical discharge machining (ECDM). *Journal of Manufacturing Processes*, *15*(4), 460-466.

Kline, W. A., DeVor, R. E., & Lindberg, J. R. (1982). The prediction of cutting forces in end milling with application to cornering cuts. *International Journal of Machine Tool Design and Research*, *22*(1), 7-22.

Koenigsberger, F., & Sabberwal, A. J. P. (1961). An investigation into the cutting force pulsations during milling operations. *International Journal of Machine Tool Design and Research*, *1*(1-2), 15-33

Kunieda, M., Lauwers, B., Rajurkar, K. P., & Schumacher, B. M. (2005). Advancing EDM through fundamental insight into the process. *CIRP Annals-Manufacturing Technology*, *54*(2), 64-87.

Lide, D. R. (Ed.). (2004). *CRC handbook of chemistry and physics*. CRC press.

Mochimaru, Y., Ota, M., & Yamaguchi, K. (2012). Micro hole processing using electro-chemical discharge machining. *Journal of Advanced Mechanical Design, Systems, and Manufacturing*, *6*(6), 949-957.

Nakasuji, T., Kodera, S., Hara, S., Matsunaga, H., Ikawa, N., & Shimada, S. (1990). Diamond turning of brittle materials for optical components. *CIRP Annals-Manufacturing Technology*, *39*(1), 89-92.

Nann, T., & Heinze, J. (1999). Simulation in electrochemistry using the finite element method: Part 1: The algorithm. *Electrochemistry Communications*, *1*(7), 289-294.

Omar, O. E. E. K., El-Wardany, T., Ng, E., & Elbestawi, M. A. (2007). An improved cutting force and surface topography prediction model in end milling. *International Journal of Machine Tools and Manufacture*, *47*(7), 1263-1275.

Raizer, Y. P., & Allen, J. E. (1997). *Gas discharge physics*. Berlin: Springer.

Schneegaß, I., Bräutigam, R., & Köhler, J. M. (2001). Miniaturized flow-through PCR with different template types in a silicon chip thermocycler. *Lab on a Chip*, *1*(1), 42-49.

Takeuchi, Y., Sawada, K., & Sata, T. (1996). Ultraprecision 3D micromachining of glass. *CIRP Annals-Manufacturing Technology*, *45*(1), 401-404.

Wei, C., Hu, D., Xu, K., & Ni, J. (2011). Electrochemical discharge dressing of metal bond micro-grinding tools. *International Journal of Machine Tools and Manufacture*, *51*(2), 165-168.

Wei, C., Ni, J., & Hu, D. (2010). Electrochemical discharge machining using micro-drilling tools. *Transactions of NAMRI/SME*, *38*, 105-111.

Wei, C., Xu, K., Ni, J., Brzezinski, A. J., & Hu, D. (2011). A finite element based model for electrochemical discharge machining in discharge regime. *The International Journal of Advanced Manufacturing Technology*, *54*(9-12), 987-995.

West, J., & Jadhav, A. (2007). ECDM methods for fluidic interfacing through thin glass substrates and the formation of spherical microcavities. *Journal of Micromechanics and Microengineering*, *17*(2), 403.

Wüthrich, R., & Fascio, V. (2005). Machining of non-conducting materials using electrochemical discharge phenomenon—an overview. *International Journal of Machine Tools and manufacture*, *45*(9), 1095-1108.

Wüthrich, R., Despont, B., Maillard, P., & Bleuler, H. (2006). Improving the material removal rate in spark-assisted chemical engraving (SACE) gravity-feed micro-hole drilling by tool vibration. *Journal of Micromechanics and Microengineering*, *16*(11), N28.

Wüthrich, R., & Hof, L. A. (2006). The gas film in spark assisted chemical engraving (SACE)—a key element for micro-machining applications. *International Journal of Machine Tools and Manufacture*, *46*(7), 828-835.

Wüthrich, R., Spaelter, U., & Bleuler, H. 2006. "The current signal in spark-assisted chemical engraving (SACE): what does it tell us," *Journal of Micromechanics and Microengineering*, 16(4), pp. 779.

Wüthrich, R., & Ziki, J. D. A. (2009). *Micromachining Using Electrochemical Discharge Phenomenon: Fundamentals and Application of Spark Assisted Chemical Engraving*. Elsevier.

Yang, C. K., Cheng, C. P., Mai, C. C., Cheng Wang, A., Hung, J. C., & Yan, B. H. 2010. Effect of surface roughness of tool electrode materials in ECDM performance, *International Journal of Machine Tools and Manufacture*, 50(12), pp. 1088-1096.

Yang, C. K., Wu, K. L., Hung, J. C., Lee, S. M., Lin, J. C., & Yan, B. H. (2011). Enhancement of ECDM efficiency and accuracy by spherical tool electrode.*International Journal of Machine Tools and Manufacture*, *51*(6), 528-535.

Zheng, Z. P., Cheng, W. H., Huang, F. Y., & Yan, B. H. (2007). 3D microstructuring of Pyrex glass using the electrochemical discharge machining process. *Journal of micromechanics and microengineering*, *17*(5), 960

Zuber, N. (1959). *Hydrodynamic aspects of boiling heat transfer (thesis)* (No. AECU-4439). University of California, Los Angeles; and Ramo-Wooldridge Corporation, Los Angeles